

Determination of three-dimensional wind-vector fields using a bistatic Doppler radar network

Dipl.–Met. Katja Friedrich

DLR-Oberpfaffenhofen
Institut für Physik der Atmosphäre
D-82234 Weßling

Dissertation
der Fakultät für Physik
der Ludwig-Maximilians-Universität München

Oberpfaffenhofen 2002

Gutachter der Dissertation:

Erster Gutachter Prof. Dr. U. Schumann

Zweiter Gutachter Prof. Dr. R. K. Smith

Tag der mündlichen Prüfung: 22.Juli 2002

Bestimmung 3–dimensionaler Windvektorfelder mit einem bistatischen Dopplerradar Netzwerk

Kurzzusammenfassung

Diese Arbeit zeigt, dass mit Hilfe eines bistatischen Dopplerradars räumlich und zeitlich hochaufgelöste horizontale Windvektorfelder in stratiformen und konvektiven Niederschlag sowie während clear–air Situationen gemessen werden können. Die Vertikalgeschwindigkeit wird über eine Variationsanalyse bestimmt.

Eine ausführliche Diskussion ist der optimalen Positionierung der bistatischen Empfänger bezüglich der räumlichen Auflösung und der Genauigkeit der Windfeldmessung, technologischen Veränderungen innerhalb des bistatischen Netzwerkes sowie der Bewertung der Datenqualität gewidmet. Ein Qualitätskontrollschema wurde entwickelt, das nicht nur die Genauigkeit der Windfeldmessung, sondern auch die Signalstärke und die Wahrscheinlichkeit von internen (z.B. Nebenkeulenkontamination, Störungen bei Empfängersynchronisation) oder externen (z.B. Vögel) Störungen berücksichtigt. Die horizontalen Windvektorfelder gemessen mit dem bistatischen Dopplerradar wurden mit Hilfe von in–situ Flugzeugmessungen und mit Messungen von einem unabhängigen Dopplerradar evaluiert. Die Arbeit umfasst eine theoretische Studie über zukünftige Anwendungsgebiete bistatischer Radarsysteme, z.B. im Flughafennahbereich, für Assimilation in numerische Wettervorhersagemodelle und für Windmessungen innerhalb des Radarverbundes des Deutschen Wetterdienstes.

Determination of three–dimensional wind–vector fields using a bistatic Doppler radar network

Short Abstract

This thesis shows that a bistatic Doppler radar is capable of measuring temporal and spatial high–resolution horizontal wind–vector fields within stratiform and convective precipitation and clear–air. The vertical velocity is estimated using a variational analysis method.

The setup of bistatic receivers arranged optimally in terms of resolution and accuracy of the horizontal wind, technological advancements of the bistatic system, and determining the data quality are discussed. A quality-control scheme is developed, which considers not only the accuracy of the horizontal wind-field determination, but also signal quality and the probability of contamination due to external (e.g. birds) or internal (e.g. sidelobe, receiver synchronization) effects. The horizontal wind–vector fields measured by a bistatic Doppler radar are evaluated using in–situ flight measurements and measurements from an independent monostatic Doppler radar. This thesis concludes with a theoretical study on how bistatic Doppler radar measurements can be utilized in future, e.g. for warning of severe weather, now–casting in the vicinity of airports, or for assimilating wind–vector fields into numerical weather prediction models.

Contents

Zusammenfassung	vi
Abstract.....	vii
1 Introduction	1
1.1 Motivation	1
1.2 State of the art	2
1.3 Aims and strategy	5
2 Monostatic versus bistatic Doppler radar	7
2.1 Geometry and radar properties	7
2.2 Velocity components and Nyquist velocity	10
2.3 Radar equation	12
2.3.1 General derivations	12
2.3.2 Detection of spherical targets	13
2.4 Normalized power	19
2.4.1 Minimum detectable equivalent reflectivity factor	21
2.5 Sidelobe contamination	21
2.6 Determination of the horizontal wind-field	25
2.7 Accuracy of the wind-field determination	28
2.8 Optimal arrangement for the bistatic receiver	31
3 The bistatic Doppler radar network	35
3.1 Bistatic network design	35
3.2 Bistatic antennas	36
3.3 Real-time wind synthesis at the central hub computer	39
4 Wind synthesis and quality control	42
4.1 Data-processing	43
4.1.1 Dealiasing of Doppler velocity	43
4.1.2 Interpolation onto a Cartesian grid and to a reference time	46
4.2 Synthesis of the horizontal wind-vector field	47
4.3 Quality-control scheme for horizontal wind-vector fields	51
4.3.1 Utilizing geometrical accuracy	52
4.3.2 Utilizing signal quality based on the reflectivity gradient	53
4.3.3 Utilizing signal quality based on fractional uncertainty	55
4.4 Utilizing data consistency	56
4.4.1 Utilizing data consistency based on a persistence check	57
4.4.2 Utilizing data consistency based on an internal check	58
4.4.3 Utilizing data consistency based on a sidelobe contamination check ..	60

5	A variational analysis method to determine the vertical velocity	63
5.1	State of the art	63
5.2	Methodology	64
5.2.1	The minimization procedure	65
5.2.2	Vertical integration of the equation of continuity	66
5.3	Testing vertical integration with simulated radar data	67
5.3.1	Experimental design	67
5.3.2	Results of the retrieval	70
5.3.3	Assessment and discussion	76
6	Retrieval of wind-fields	78
6.1	Stratiform precipitation in a frontal system: 2 February 2000	78
6.1.1	Meteorological situation and data analysis	78
6.1.2	Assessment and discussion	78
6.2	Stratiform precipitation in a frontal system: 10 April 2001	82
6.2.1	Meteorological situation and data analysis	82
6.2.2	Assessment and discussion	83
6.3	Wind-vectors within a convective system: 3 May 2000	83
6.3.1	Meteorological situation and data analysis	83
6.3.2	Assessment and discussion	87
6.4	Wind-fields within a clear-air situation: 18 August 1998	90
6.5	Assessment and discussion	92
7	Evaluation of horizontal wind-fields	94
7.1	Intercomparison to monostatic Doppler radar measurements	94
7.2	Intercomparison to in-situ flight measurements	96
8	Future applications	100
8.1	Wind-vector fields throughout Germany	100
8.2	Wind-vector fields in the vicinity of airports	102
8.3	Assimilation of wind-vector fields	103
9	Summary and Conclusion	110
A	Technical specifications	113
A.1	Transmitting radar, POLDIRAD	113
A.1.1	Receiver at the radar	113
A.2	Bistatic receivers at remote sites	114
B	Signal Processing	115
	Abbreviations	118
	References	118
	Acknowledgement	125
	Curriculum vitae	129

Zusammenfassung

Die Kenntnis des 3-dimensionalen Windvektorfeldes hat für die Forschung und für die operationelle Wettervorhersage eine essentielle Bedeutung, z.B. für die Untersuchung von Transportprozessen in Gewittern, für Wetterüberwachung und -vorhersage.

Diese Arbeit zeigt, dass mit Hilfe eines bistatischen Dopplerradars räumlich und zeitlich hochaufgelöste horizontale Windvektorfelder in stratiformen und konvektiven Niederschlag sowie während clear-air Situationen gemessen werden können. Das bistatische Dopplerradar-Netzwerk am DLR ist das erste weltweit, das mit einem C-band Dopplerradar und mit einem Magnetronsender betrieben wird. Die Vertikalgeschwindigkeit wird über eine Variationsanalyse bestimmt. Der Einfluss von Datendichteschwankungen und der Integrationstechnik auf die Qualität des abgeleiteten Vertikalwindes wurde anhand von simulierten Radardaten untersucht.

Eine ausführliche Diskussion ist der optimalen Positionierung der bistatischen Empfänger bezüglich der räumlichen Auflösung und der Genauigkeit der Windfeldmessung, technologischen Veränderungen innerhalb des bistatischen Netzwerkes sowie der Bewertung der Datenqualität gewidmet.

Windfeldmessungen mit einer räumlichen Auflösung von 150 m – 700 m und einer Genauigkeit von 2 m s^{-1} – 3 m s^{-1} können innerhalb eines Streuwinkelsbereichs von 50° bis 140° durchgeführt werden. Die Fähigkeit des Empfängers, schwache Signale zu detektieren, erhöht sich, wenn die gesendete elektromagnetische Welle sowie die Empfangsantenne am Boden vertikal polarisiert sind. Ab einer Höhe von 9 km sollte eine 45° bzw. 135° polarisierte Welle ausgesendet werden.

In Übereinstimmung mit der optimalen Positionierung von Empfänger zu Sender wurde das bistatische multiple Dopplerradar-Netzwerk, bestehend aus drei bistatischen Empfängern, in Oberpfaffenhofen installiert. Neben den konventionellen Antennen für die Messungen innerhalb der Grenzschicht wurden zusätzlich zwei Prototypantennen für Gewittermessungen entwickelt.

Ein Qualitätskontrollschema wurde entwickelt, das nicht nur die Genauigkeit der Windfeldmessung, sondern auch die Signalstärke und die Wahrscheinlichkeit von internen (z.B. Nebenkeulenkontamination, Störungen bei Empfängersynchronisation) oder externen (z.B. Vögel) Störungen berücksichtigt. In diesem Schema werden die verrauschten Messungen verworfen und die Qualität der übrigen anhand einzelner Qualitätsindices, die zwischen null und eins variieren, analysiert. Diese Qualitätsfelder werden gemittelt und stehen neben den Windfeldmessungen dem Nutzer zur Verfügung.

Die horizontalen Windvektorfelder, gemessen mit dem bistatischen Dopplerradar, wurden mit Hilfe von in-situ Flugzeugmessungen und mit Messungen von einem unabhängigen Dopplerradar evaluiert. Die Differenzen schwanken zwischen 1 m s^{-1} bis 2 m s^{-1} .

Die Arbeit umfasst außerdem eine theoretische Studie über zukünftige Anwendungsgebiete bistatischer Radarsysteme, z.B im Flughafennahbereich, für Assimilation in numerische Wettervorhersagemodelle und für Windmessungen innerhalb des Radarverbundes des Deutschen Wetterdienstes.

Abstract

A knowledge of wind–vector components throughout the atmosphere is extremely desirable for both meteorological research and operational meteorology, e.g. diagnostic research study, hazard warning, regional weather surveillance, nowcasting of meteorological phenomena, and assimilation into numerical weather prediction models.

This thesis shows that a bistatic Doppler radar is capable of measuring temporally and spatially high–resolution horizontal wind–vector fields within stratiform and convective precipitation and in clear–air. The bistatic Doppler radar network at the DLR is the first worldwide operating with a monostatic C–band Doppler radar and with a magnetron transmitter. The vertical velocity is estimated using a variational analysis method. The impact of the integration technique and the influence of irregular data density on the quality of vertical–velocity retrieval is investigated also.

The setup of bistatic receivers arranged optimally in terms of resolution and accuracy of the horizontal wind, technological advancements of the bistatic system, and the determination of the data quality are discussed.

Wind–field measurements can be achieved with a spatial resolution ranging from 150 m to 700 m and a standard deviation margin varying between 2 m s^{-1} and 3 m s^{-1} within a scattering–angle limit of 50° to 140° . Investigations on how the transmitted wave and the receiver have to be polarized indicate that vertically–polarized transmitted wave and vertically–polarized receiver are optimal at lower altitudes. At higher altitudes (above a height of 9 km), a transmitted wave with slanted $45^\circ/135^\circ$ polarization and a receiver polarized vertically give a higher sensitivity.

In accordance with bistatic receivers arranged optimally, the bistatic multiple–Doppler radar network consisting of three bistatic receivers was installed around Oberpfaffenhofen. Besides the conventional bistatic antennas for measurements within the boundary layer, two prototype antennas were developed in the context of this thesis.

A quality–control scheme is developed, which considers not only the accuracy of the horizontal wind–field determination, but also signal quality and the probability of contamination due to external (e.g. birds) or internal (e.g. sidelobe, receiver synchronization) effects. In this quality–control scheme, the algorithms either reject noisy data or the quality of the measurements is analyzed by means of quality–index fields with values ranging from zero to one. These fields can be merged into an average quality–control field which is available together with the wind–vector field to the user.

The horizontal wind–vector fields measured by a bistatic Doppler radar are evaluated using in–situ flight measurements and measurements from an independent monostatic Doppler radar. The differences range between $\pm 2 \text{ m s}^{-1}$.

This thesis concludes with a theoretical study on how bistatic Doppler radar measurements can be utilized in future, e.g. for warning of severe weather, now–casting in the vicinity of airports, or for assimilating wind–vector fields into numerical weather prediction models.

1 Introduction

1.1 Motivation

A knowledge of wind–vector components throughout the atmosphere is extremely desirable for both meteorological research and operational meteorology, e.g. diagnostic research study, hazard warning, regional weather surveillance, nowcasting of meteorological phenomena, and assimilation into numerical weather prediction models. Diagnosing and predicting storms is specially important in regional weather forecasts. Dynamic processes in the atmospheric boundary layer, e.g. transport processes in thunderstorms, can be identified, characterized and understood with a knowledge of the wind–vector. The observed wind–vector fields can be used for weather forecast or applied directly to severe weather warning systems, for example, in the vicinity of airports or around populated areas. Wind–vector fields are desirable for assimilation into numerical weather prediction models to adjust the model initial state more realistically to the meteorological situation at the time of the observation. Hence, the continuous observation of wind–vector fields in time and space is a great challenge.

A Doppler radar system is an instrument capable of sampling Doppler velocity and reflectivity over a horizontal range of up to 250 km, with a spatial resolution of a hundred meters and a temporal resolution within minutes. With a traditional monostatic Doppler radar system, only one wind component out of three can be measured. Various techniques for scientific and operational usage can be applied to retrieve wind–vector fields from Doppler velocity and reflectivity measurements. If two or more Doppler radar systems are monitoring the same region, the Doppler velocities can be combined to form a wind–vector field. The major limitation when combining monostatic radar systems is the expense incurred for installation, transport, and operational usage. Furthermore, Doppler velocities are not measured simultaneously by a multiple–Doppler radar network. Rather, each individual radar system has its own scan algorithm, scan time, and scans in a spherical coordinate system centered round the radar. All Doppler velocities have to be merged into a reference time and onto a common coordinate system before a wind synthesis can be applied. The interpolation of each measurement in time and space can cause difficulties, especially in the case where weather systems evolve rapidly.

High costs can be avoided and the interpolation discrepancies of each Doppler velocity measurements in time and space can be made negligible when employing a bistatic multiple-Doppler radar system. The latter consists of a traditional transmitting/receiving Doppler radar system and one or more passive, non–transmitting receivers with broad-beam antennas located at remote sites. In a bistatic Doppler radar system, transmitter and receiver are spatially separated, whereas in a monostatic radar system transmitter and receiver are collocated. In a bistatic multiple–Doppler network, several bistatic receivers are grouped around one monostatic radar system. The advantage when compared to monostatic multiple-Doppler radar networks is the easy implementation of bistatic receivers to an already existing transmitting Doppler

radar system. A bistatic receiver costs less than 5% of a typical weather radar system. The reason that enables Doppler velocity measurements to be carried out simultaneously is owing to the fact that these measurements are based on just a single source of illumination.

1.2 State of the art

The first radar systems were constructed in the United States, United Kingdom, France, Italy, Russia, Germany, and Japan in the late 1930s with separate transmitter and receiver for technical reasons, e.g. to avoid transmitter/receiver switching (a duplexer¹ had not yet been developed), and to be able to use continuous waves. The main application at that time was in aircraft- and ship-detection. At that time, radar systems attained a distance of up to 40 km. For reasons of economy and operational efficiency, monostatic radar systems had been dominated the scene ever since the invention of duplexer and pulsed transmission. However, because the demands on military radar systems had become increasingly severe in the Seventies, multistatic radar systems were rediscovered, which resulted also in new progress on radar technology (antennas, processing capabilities, computer control). Bistatic radar systems were applied primarily to military use. These systems usually employ a ground-based transmitter and a receiver carried by missile or aircraft for the purpose of processing the reflected signals. Because only the emission can be detected, the bistatic receiver remains undetected. Therefore, bistatic radar systems were used for aircraft-, missile- and ground-target detection and also to protect aircraft at the ground level. These systems, for instance, have an airborne or ground-based transmitter and inexpensive ground-based receivers. Non-military applications were, e.g., planetary explorations such as mapping the surfaces of the moon and Venus and inferring the thickness of Saturn's rings. Bistatic methods were also used to observe the long-wavelength directional ocean-wave spectra [for more historical detail, see Glaser (1986); Hanle (1986)].

Early meteorological experiments with bistatic radar systems² concentrated only on power data. To detect the melting layer and approximate values for the layer thickness, for example, Doviak & Weil (1972) gave methods for interpreting data measured by a bistatic system. Doviak (1972) also showed how one could detect targets within non-precipitating situations with a bistatic radar system.

Shupyatsky (1974) was able to trace large particles in a cumulonimbus with the help of computations indicating that depolarization measurements at various scattering angles do indeed provide information about the presence of large particles and particle-distribution parameters. He used reflectivity measured by a bistatic receiver in order to evaluate scattering models for different frequencies. The use of polarimetric parameters in scattering models was also investigated by Crane (1974); Awaka &

¹ *A device in the waveguide which protects the sensitive receiver from the full power of the transmitter [cited from the glossary by Rinehart (1999)].*

²At the beginning, two monostatic radar facilities were used for bistatic measurements.

Oguchi (1982); Dibbern (1987).

Only after frequency and time coherence measurements between transmitter and receiver had been achieved, however, measuring Doppler velocities bistatically with a conventional radar systems was made possible. Since Wurman et al. (1993); Wurman (1994a,b); Wurman et al. (1994) developed a bistatic receiver for meteorological applications in 1993, however it is now possible to measure both Doppler-velocity and power with bistatic Doppler radar systems. To determine wind-vectors Wurman et al. (1993); Wurman (1994a,b); Wurman et al. (1994) presented a detailed description of the design and the advantages of a bistatic Doppler radar system as compared to a monostatic one.

Investigations on measurement characteristics within a bistatic Doppler radar system and wind-vector field analysis had already been initiated, e.g., for supercell hailstorms and convective systems by Skolnik (1990); Satoh & Wurman (1999); de Elia & Zawadzki (2000); de Elia (2000); Friedrich et al. (2000); Takaya & Nakazato (2002). Furthermore, Doppler velocities, measured by a bistatic Doppler radar, were used as input data for a constraining model using a variational analysis method in order to derive thermodynamical parameters in addition to the wind components³, u, v, w , (Protat & Zawadzki, 2000; Montmerle et al., 2001). Montmerle et al. (2001) developed an analysis scheme to initialize a cloud-resolving model from kinematic and thermodynamic fields. These fields were retrieved from Doppler velocities, measured by a bistatic multiple-Doppler radar system, using a constraining model.

Ever since the bistatic receivers have been constructed, they have been developing as an alternative to the monostatic multiple-Doppler radar system. They can be applied in addition to existing monostatic radar systems.

As part of a collaboration between the University of Oklahoma and the National Center for Atmospheric Research (NCAR) in the United States, and McGill University in Montreal, Canada, two bistatic receivers have been operating together using the McGill S-band Doppler radar around Montreal since 1996. The NCAR has used its bistatic network for several research experiments, e.g. in Colorado, Florida, Kansas (CASES97), and Washington (IMPROVE 2001). In 1998, one bistatic receiver was installed at the Deutsches Zentrum für Luft- und Raumfahrt (DLR) in Oberpfaffenhofen (OP), close to Munich in southern Germany. It was the first bistatic radar system operating at C-band with a magnetron transmitter⁴. Since then, the network has been augmented by two receiver systems and four bistatic antennas. Recently, at the Communication Research Laboratory (CRL) in Okinawa and at Hokkaido University, the Japanese have installed a bistatic Doppler radar network.

The bistatic Doppler radar network in Oberpfaffenhofen consists now of the mono-

³The wind vector at each point in the three-dimensional space consists of the west-wind component u , south-wind component v , and the updraft w . The horizontal wind-vector consists of the west- and south-wind components u and v .

⁴A self-exciting oscillator tube used to produce the transmitted pulse. In comparison to a klystron, where the phase of the transmitted pulse is exceptionally stable over long periods of transmission, in a magnetron the phase is random and has to be measured for each transmission (Rinehart, 1999).

static polarimetric Doppler radar system, POLDIRAD (Schroth et al., 1988), and three bistatic receivers at remote sites each containing both at least one antenna and a signal processor. In Fig. 1, the location of the three bistatic receivers and the respective look angles of the bistatic antennas are illustrated. The investigation area, indicated schematically, is restricted by the received power pattern of the bistatic antenna, which has a horizontal angular aperture covering about -30° to 30° (henceforth horizontal antenna aperture). The horizontal antenna aperture together with range arcs are exhibited in Fig. 1 for each bistatic antenna.

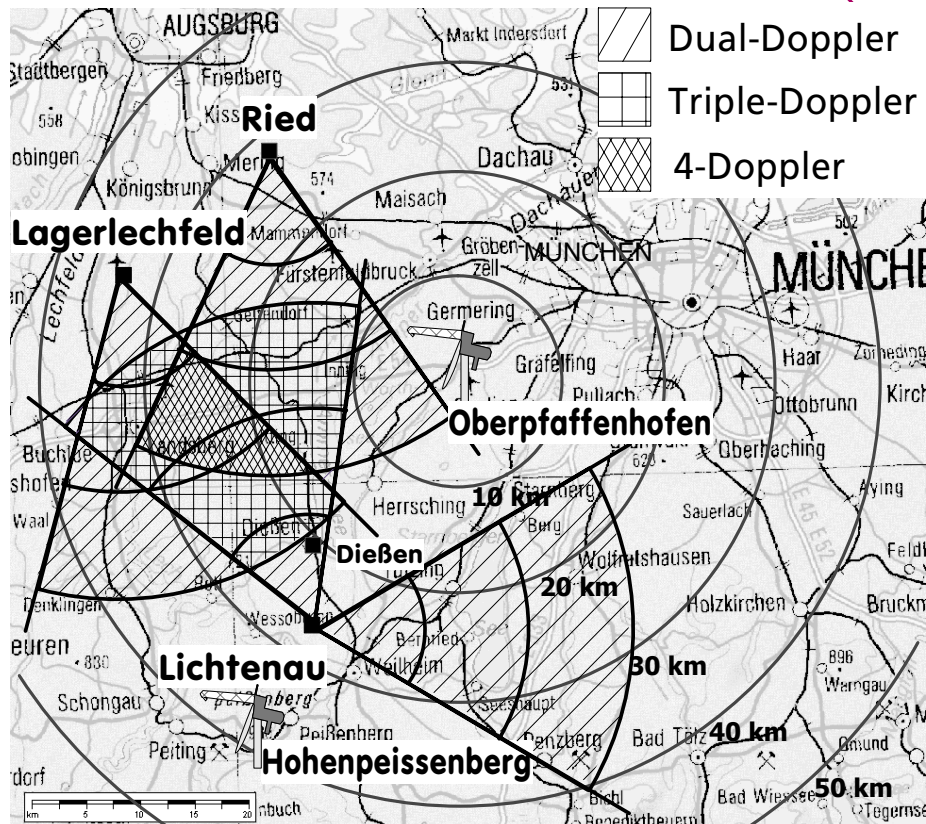


Figure 1: Map of the bistatic multiple-Doppler radar network at the DLR in OP consisting of POLDIRAD and three bistatic receivers located at Lichtenau, Lagerlechfeld, and Ried. The investigation area is restricted by the horizontal antenna aperture of the bistatic antennas. The equation system to calculate the horizontal wind-field is exactly determined in the dual-Doppler areas (hatched) and overdetermined in the triple- or quadruple-Doppler areas (cross-hatched). An additional monostatic Doppler radar system, operated by the German Weather service (DWD) is located at Hohenpeißenberg. A meteorological surface observation station is placed in Dießen.

Both receiver systems at Lagerlechfeld and Lichtenau are equipped with two antennas each, which have a vertical angular aperture covering 1° to 9° and 1° to 23° , respectively. At Ried, one antenna having a vertical aperture of 8° has been installed (more details in Sec. 3.2). At the moment, the bistatic radar network at OP covers

an area of about $50 \text{ km} \times 50 \text{ km}$. Within this area, horizontal wind-fields are determined exactly in the dual-Doppler area (in Fig. 1 hatched) and overdetermined in triple-/quadruple-Doppler areas (in Fig. 1 cross-hatched).

Due to a limited vertical antenna aperture of 8° oriented close to the ground, the measured wind components are dominated by the horizontal components u, v . As a result, these measurements are used only to determine the horizontal wind-vector field directly. The vertical component, w , is retrieved by means of a variational analysis method. Over the years, a great effort has been made to retrieve the three components of the wind-vector from Doppler velocity and reflectivity measurements using variational analysis methods (Miller & Strauch, 1974; Bohne & Srivastava, 1976; Ray et al., 1978, 1980; Ray & Sangren, 1983). Alternatively, variational analysis methods have been expanded to use dual-/multiple-Doppler radar data to retrieve the three components of the wind-vector (Gao et al., 1999; Protat & Zawadzki, 1999; Shapiro & Mewes, 1999). The variational analysis methods are being continually improved for monostatic (Shapiro & Mewes, 1999) as well as for multiple-Doppler analysis (Chong et al., 1983; Chong & Testud, 1983; Gao et al., 1999; Protat & Zawadzki, 2000). Protat & Zawadzki (1999) expended a constraining model based on a variational analysis method, developed by Laroche & Zawadzki (1994), for using Doppler velocity data measured by bistatic -Doppler radar, to retrieve u, v, w . They refined the constraining model by, e.g. using the results of both vertical up- and downward integration of the continuity equation or interpolating data linearly to a single reference time. The retrieval of the wind-vector field was presented using data, which were collected during a shallow supercell hailstorm, by the McGill bistatic Doppler radar network. The network includes a monostatic S-band Doppler radar located 30 km west of Montreal.

1.3 Aims and strategy

The main aim of this thesis is to determine temporally and spatially high-resolution, quality-controlled horizontal wind-vector fields by using the bistatic multiple-Doppler radar network at OP. This is the first network operating with a monostatic C-band Doppler radar and with a magnetron transmitter. Another aim is to determine also the vertical velocity which has been done by means of the constraining model using variational methods. The requirement on a bistatic radar system is to achieve measurements within the same weather situations as those obtained by a monostatic radar, e.g. within stratiform and convective precipitation and within non-precipitating situations (clear-air situation⁵).

To achieve these aims, an optimal arrangement of the transmitter and several receivers are obtained to measure within the boundary layer as well as during thunderstorms. Furthermore, fast, flexible, and individual data acquisition and processing al-

⁵Within non-precipitating air, the radar echo can be scattered from insects, dust, chaff, and other particulates in the atmosphere. Small-scale fluctuations of the refractive index of the atmosphere can also return some of the incident power (Rinehart, 1999).

gorithms are developed, which will be applicable for each individual multiple-Doppler radar network.

To attain quality-controlled wind-vector fields, algorithms are developed and tested to quantify the confidence of the measurement determined by the bistatic Doppler radar network. The final aim is to process the high-resolution wind-vector fields, so that they are available operationally to further application. This data processing must include an automatic quality control, dealiasing, and retrieval of the wind-vector fields.

In Sec. 2, the optimal arrangement in terms of spatial resolution and accuracy in wind-field determination is derived for a bistatic radar system. Knowing the spatial distribution of the radar properties (such as range resolution, velocity projection, Nyquist velocity, and scattering characteristics of Rayleigh particles) which are discussed in Sec. 2, an optimal receiver arrangement can be found. Furthermore, this section deals with determining the horizontal wind-vector field and calculating its accuracy for several monostatic and/or bistatic receivers.

Section 3 introduces the bistatic multiple-Doppler radar network at OP. Technical specifications and technical improvements of the bistatic radar system as well as data acquisition are explained. Section 4 discusses data-processing algorithms, including dealiasing of the Doppler velocity, interpolating radar data onto a Cartesian grid and to reference time, and analyzing data quality. The quality-controlled Doppler-velocity data can be used to compose a horizontal wind-vector field or, alternatively, to retrieve also the vertical-wind component using a constraining model. This model is presented in Sec. 5. This section also investigates the impact of the integration technique and the influence of irregular data density on the quality of vertical-velocity retrieval. Sec. 6 demonstrates how to process Doppler velocities and how to determine a quality-controlled high-resolution wind-vector field. The methodology is applied to bistatic Doppler radar measurements obtained during stratiform precipitation in a frontal system, during precipitation within a convection system, and during a clear-air situation. In Sec. 7, an attempt is made to test the confidence of wind-vector fields determined by a bistatic Doppler radar. The horizontal wind-field is evaluated using in-situ flight measurements and measurements from an independent monostatic Doppler radar system. The evaluation is performed during stratiform precipitation events. This thesis concludes with a theoretical study on how bistatic Doppler radar measurements can be utilized in future, e.g. for warning of severe weather and now-casting in the vicinity of airports or for assimilating wind-vector fields into numerical weather prediction models. A recommendation on how to install bistatic receivers in addition to the already existing operationally working monostatic radar systems operated by the German Weather Service (DWD) is presented in Sec. 8.

2 Monostatic versus bistatic Doppler radar

2.1 Geometry and radar properties

The principle of a bistatic Doppler radar network is explained in Fig. 2.1: The monostatic Doppler radar system transmits an electro-magnetic wave (thick line) which is scattered by a target in all directions. Reflectivity and Doppler velocity are measured by bistatic receivers each located at a remote site and by the monostatic Doppler radar system (thin lines). The Doppler velocities, measured simultaneously by each receiver (gray arrows), represent the components of the wind vector. These wind components can then be combined to a wind-vector.

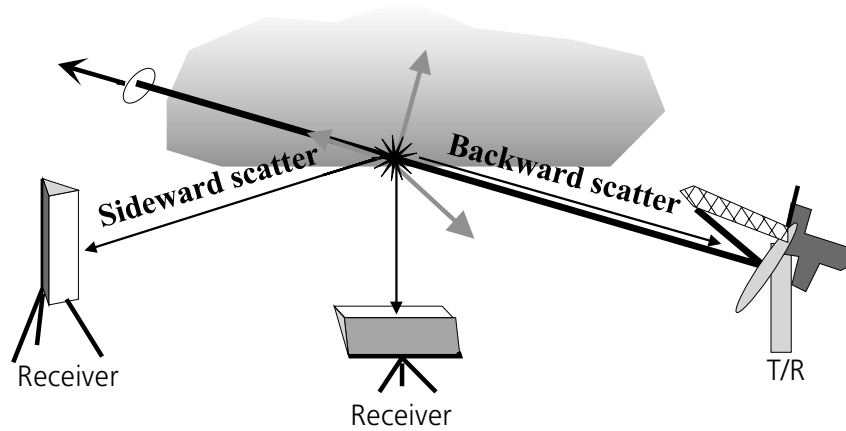


Figure 2.1: Principle of a bistatic multiple-Doppler radar system consisting of one monostatic Doppler radar system and two bistatic receivers located at remote sites.

In the monostatic case, the target location is defined by the propagation of the electro-magnetic wave to the target and returning to the radar at a given time after the pulse has been emitted. The total distance traveled by the pulse (traveling with the speed of light) is denoted by $2r'_t$.

The geometrical properties of a bistatic radar network are given in Fig. 2.2. In the bistatic case, where transmitter and receiver are not collocated, the signal travels two different paths. The propagation time measured by the bistatic receiver represents the distance from the transmitter to the target and from the target to the receiver, given by $r'_t + r'_b$. The scattering plane is defined by the bistatic triangle (Skolnik (1990) p. 25.13), which connects transmitter, target, and receiver. Because the scattering process is formulated according to the backscatter alignment convention following van Zyl & Ulaby (1990), the scattering plane is characterized by the scattering angle, γ , enclosed by r'_b and r'_t . The baseline between transmitter and receiver is denoted by b . The angle between the distance transmitter-target and transmitter-bistatic receiver is given by α , while the angle between the distance bistatic receiver-target and receiver-transmitter is given by β . The scattering plane, projected onto the horizontal plane, is defined by the respective angles extended by the index h and the

respective distances, r_t, r_b . With respect to the earth's surface, the direction of the transmitted beam is given by the azimuth angle, ϕ_t (pointing to North $\phi_t = 0^\circ$ and it increases clockwise), and by the elevation angle, θ_t (with $\theta_t = 0^\circ$ at ground level and it increases upward). The azimuth and elevation angle of the bistatic antenna are denoted by ϕ_b and θ_b , respectively, with the same convention as that for the monostatic radar. Note that the non-rotating bistatic antennas have a wide antenna aperture. Therefore, the position of the target related to bistatic receiver is derived from the propagation time and ϕ_t, θ_t .

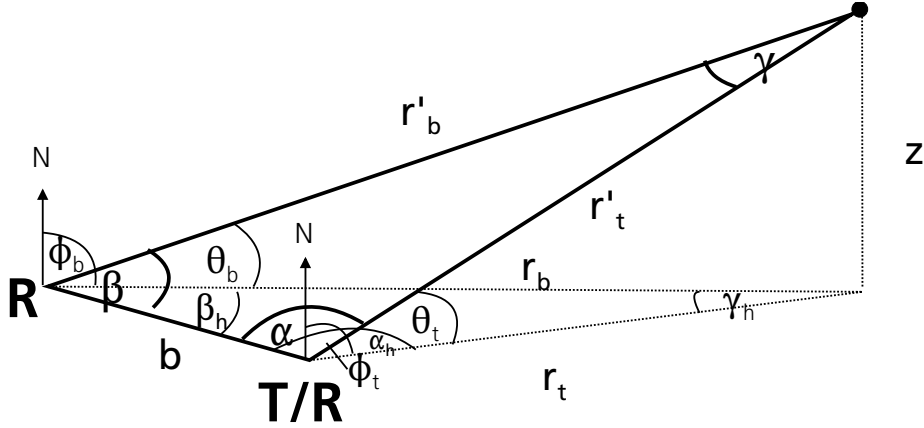


Figure 2.2: Definition of geometrical parameters in a bistatic radar system. Hereafter, the monostatic transmitting and receiving radar is denoted by T/R and the bistatic receiver by R. The scattering angle γ spans the incident ray, traveling along r'_t , and the scattered ray, traveling along r'_b . The position and size of the scattering plane is defined by the angles α, β, γ , and the distances r'_t, r'_b, b , respectively. When projecting the scattering plane onto the horizontal plane, the angles are named as $\alpha_h, \beta_h, \gamma_h$, and the distances as r_t, r_b, b , respectively.

Certain radar parameters such as range-resolution, Doppler velocity measurement, Nyquist velocity, and scattered power depend on the scattering angle γ . An overview of the radar parameters of a bistatic Doppler radar system as well as the major differences between monostatic and bistatic radar characteristics are pointed out in Tab. 2.1. Each characteristic is explained in greater detail further in this chapter. Technical specifications for the DLR transmitter and receiver system can be found in Sec. 3.

The scattering angle γ spans the incident wave and the scattered wave. Figure 2.3 exhibits the spatial distribution of $\gamma/2$ within a bistatic dual-Doppler radar system. When $\gamma \geq 160^\circ$, that part of the electro-magnetic wave scattered in a forward direction, is measured by the bistatic receiver (Fig. 2.3, cross-hatched area). The sideward scattered region is the angular region between $20^\circ < \gamma < 160^\circ$ (Fig. 2.3, plain area). While $\gamma < 20^\circ$, the directions of transmission and reception, however, are almost identical (hatched area in Fig. 2.3).

Range determination with radar is achieved by measuring the time delay between

Table 2.1: An overview of the radar parameters of a monostatic and a bistatic Doppler radar system. Each characteristic is explained in more detail in the following text.

	MONOSTATIC RADAR	BISTATIC RADAR
Scattering angle	$\gamma = 0^\circ$	$0^\circ \leq \gamma \leq 180^\circ$
Surface of constant delay	Sphere	Ellipsoid
Sample volume length	$a_t = \frac{cT}{2}$	$a_b = \frac{cT}{2 \cos^2(\gamma/2)}$
Velocity component	$v_t \perp$ Sphere	$v_e \perp$ Ellipsoid
Nyquist interval	$v_{nt} = \pm \frac{\lambda}{4T_S}$	$v_{ne} = \pm \frac{\lambda}{8T_S \cos(\gamma/2)}$
Received power	$P_r \sim \frac{\sigma_b(\mathbf{s}, \mathbf{i})}{r_t^2}$	$P_r \sim \frac{\sigma_b(\mathbf{s}, \mathbf{i})}{r_b^2 \cos^2(\gamma/2)}$
Scattering cross-section (Rayleigh scattering)	$\sigma_{b\perp}(\mathbf{s}, \mathbf{i}) = \sigma \sin^2(\varphi_t)$ $\sigma_{b\parallel}(\mathbf{s}, \mathbf{i}) = \sigma \cos^2(\varphi_t)$	$\sigma_{b\perp}(\mathbf{s}, \mathbf{i}) = \sigma \sin^2(\chi)$ $\sigma_{b\parallel}(\mathbf{s}, \mathbf{i}) = \sigma \cos^2(\chi) \cos^2(\delta)$

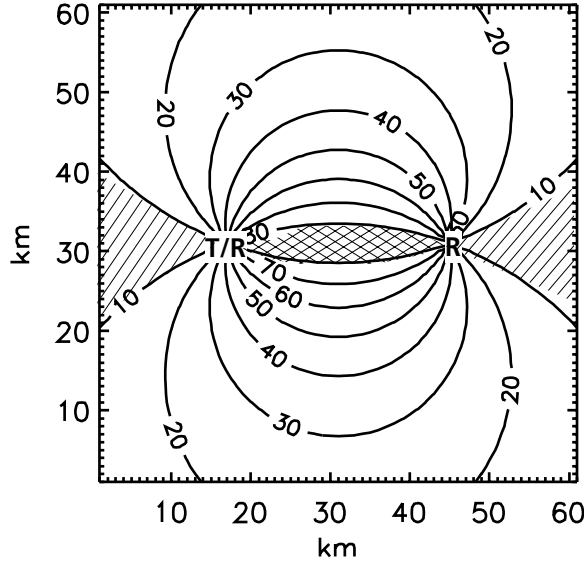


Figure 2.3: Spatial distribution of $\gamma/2$ within a bistatic dual-Doppler radar system. The two-dimensional cross-section is obtained along the scattering plane. In the cross-hatched area, the forward scattered part of the electro-magnetic wave is measured by the bistatic receiver. The backward or sideward scattered parts are measured by the bistatic receiver if the targets are located in the hatched or plain area, respectively.

transmitted and received radar pulse. Within the bistatic radar system, surfaces of constant delay are ellipsoids, with transmitter and receiver at the foci. The geometry of the transmission and reception process in a monostatic radar is a special case of the bistatic geometry. In the monostatic case, $\gamma = 0$, transmitter and receiver are collocated and the surfaces of constant delay are spheres centered in the monostatic radar system.

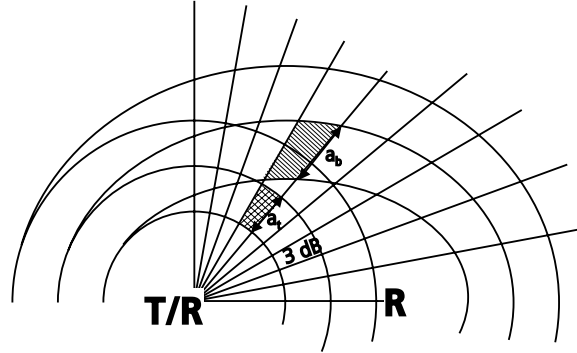


Figure 2.4: A two-dimensional cross-section the surfaces of constant delay and the sample volumes obtained along the scattering plane. In the monostatic case, surfaces of constant delay are spheres and the shape of the sample volume is illustrated in the cross-hatched area, with a length a_t . Within the bistatic radar system, surfaces of constant delay are ellipsoids and the shape of the sample volume is hatched, with a length of a_b . The 3 dB beam-width is indicated. The lines of constant delay are separated by a distance of $(c\tau)/2$.

Each pulse generated by a transmitter is emitted within the duration time, τ . This corresponds to a pulse-length $c\tau$, with c being the speed of light. The size and shape of the sample volume is defined by the length of the transmitted pulse and the two-way transmission beam-width⁶ as seen in Fig. 2.4. Whereas the length of sample volume in monostatic radar, a_t , is constant for a given pulse-length, the length of bistatic sample volume, a_b , depends in addition on γ [Tab. 2.1, de Elia & Zawadzki (2000)]. A cross-section of the size and shape of a monostatic (defined by spheres) as opposed to a bistatic sample volume (defined by ellipsoids) is illustrated in Fig. 2.4. The spatial distribution of the length of the bistatic resolution volume as a multiple of a_t is shown in Fig. 2.5. The resolution achieved with the bistatic receiver is always poorer than that achieved by monostatic measurements, ranging between $1.1a_t \leq a_b \leq 6a_t$ (plain area), or equal (hatched area). Close to the baseline (cross-hatched area), the length of the sample volume increases from $12a_t$ up to the baseline length ($a_b = b$).

2.2 Velocity components and Nyquist velocity

Measuring velocity with radar means measuring the displacement of particles within a certain time interval. Only displacements which change the distance transmitter–target–receiver can be considered. Therefore, in the case of monostatic radar, only those motions perpendicular to the spheres of constant delay can be observed (Doviak & Zrnic (1984), pp. 35). For bistatic radar systems, however, these motions have to be perpendicular to the ellipsoids of constant delay [Fig. 2.6; for more details, see Protat & Zawadzki (1999)]. Movements along the sphere or ellipsoid cannot be detected.

⁶Due to the extension of the transmitted beam, the sample volume enlarges when the distance r'_t increases.

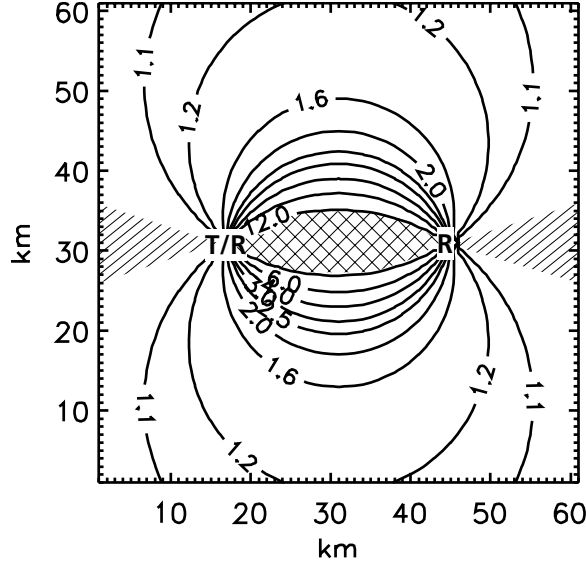


Figure 2.5: Spatial distribution of the bistatic sample volume lengths as a multiple of the monostatic one within a bistatic radar system. The two-dimensional cross-section is obtained along the scattering plane. The resolutions achieved by both bistatic and monostatic radar are nearly equal in the hatched area, while in the cross-hatched area the length of the resolution obtained by a bistatic receiver increases by a factor of 12 up to $a_b = b$. In the plain area, the length of the sample volume is always larger than that achieved using the monostatic radar.

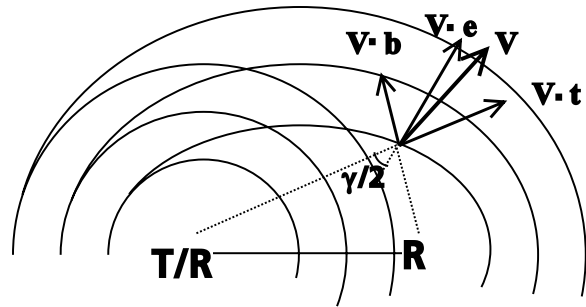


Figure 2.6: The decomposition of the wind velocity \mathbf{V} in a bistatic Doppler radar system, with the unit vectors \mathbf{t} , \mathbf{e} , and \mathbf{b} pointing in the radial direction away from the monostatic receiver, perpendicular to the ellipsoid, and in the radial direction away from the bistatic receiver, respectively. The two-dimensional cross-section is obtained along the scattering plane.

In a Cartesian-coordinate system x, y, z (east-, north-, upward), u, v , and w are the orthogonal components of the wind-vector \mathbf{V} , oriented along x, y , and z .

A bistatic receiver measures the phase shift between two successive pulses, which is caused by the difference in path length. The measured difference in path-length within a certain time interval consists of a displacement in the radial direction designated by the unit vector \mathbf{t} , and in the receiver direction denoted by the unit vector

b. Then this 'apparent' velocity, v_a , has to be projected onto the direction \mathbf{e} , which is the unit vector of the direction perpendicular to the ellipsoid of constant delay (Protat & Zawadzki, 1999), leading to

$$v_e = \mathbf{V} \cdot \mathbf{e} = \frac{v_a}{\cos(\gamma/2)}, \text{ where } v_a = \frac{1}{2} \mathbf{V} \cdot (\mathbf{b} + \mathbf{t}). \quad (2.1)$$

The Doppler velocity, v_e , measured by the bistatic receiver is perpendicular to the ellipsoid of constant delay and can be written as

$$v_e = u \frac{\sin(\phi_b) \cos(\theta_b) + \sin(\phi_t) \cos(\theta_t)}{2 \cos(\gamma/2)} + v \frac{\cos(\phi_b) \cos(\theta_b) + \cos(\phi_t) \cos(\theta_t)}{2 \cos(\gamma/2)} + (w - w_T) \frac{\sin(\theta_b) + \sin(\theta_t)}{2 \cos(\gamma/2)}. \quad (2.2)$$

The terminal fall velocity of scattering particles is represented by w_T .

For monostatic radar systems ($\gamma = 0$, $\phi_b = \phi_t$, $\theta_b = \theta_t$), Eq. (2.2) can be simplified and the radial velocity v_t can be written as

$$v_t = \mathbf{V} \cdot \mathbf{t} = u \sin(\phi_t) \cos(\theta_t) + v \cos(\phi_t) \cos(\theta_t) + (w - w_T) \sin(\theta_t). \quad (2.3)$$

For pulsed Doppler radar systems, velocity measurements are unambiguous only insofar as they lie within the Nyquist velocity interval. In the case where the wind velocities exceed the Nyquist velocity, measurements become folded into the Nyquist interval and then have to be unfolded to enable further analysis. The Nyquist velocity interval (cf. Tab. 2.1) depends on the wavelength λ and the sample time T_s (Doviak & Zrnic, 1984). The Nyquist interval for monostatic radar, v_{nt} , is constant, whereas the Nyquist interval for bistatic reception, v_{ne} , depends on γ . As a result, since $v_{ne} \geq v_{nt}$, the bistatic Doppler velocity is folded less frequently (this topic is enlarged upon Sec. 4.1.1).

2.3 Radar equation

2.3.1 General derivations

The radar equation describes how power measured by a receiver is related to the transmitted signal and to the scattering properties at a target. As a consequence, the process of transmission, reradiation of the target's energy, and reception are expressed in this equation. Following the detailed description by Doviak & Zrnic (1984), the echo power from an electro-magnetic wave scattered by a target and then measured by a receiver is

$$P_r = S_i \frac{\sigma_b(\mathbf{s}, \mathbf{i})}{4\pi r'^2_b} A_e = S_r A_e \quad (2.4)$$

where S_i is the incident radiation power density and S_r is the power density reradiated isotropically by a target and measured by a receiver. Losses of power in the system and because of attenuation along the propagation path will be neglected. The power intercepted by an apparent area of the target is $S_i \sigma_b(\mathbf{s}, \mathbf{i})$. Because the physical size of a target is in general different from the target size apparent to the radar, a new parameter called the bistatic scattering cross-section of the target⁷, $\sigma_b(\mathbf{s}, \mathbf{i})$, needs to be defined. The bistatic scattering cross-section depends not only on the properties of the particles, but also on the polarization of the incident electro-magnetic wave and the direction in which the scattered wave is received. The unit vectors of the incident and scattered direction of the wave are denoted as \mathbf{i} and \mathbf{s} , respectively. A_e is the effective aperture area of the antenna. According to Doviak & Zrnic (1984) [pp. 26] S_i and A_e are

$$S_i = \frac{P_t G_t}{4\pi r'^2_r} \quad \text{and} \quad (2.5)$$

$$A_e = \frac{G_b \lambda^2}{4\pi} . \quad (2.6)$$

Here, P_t is the transmitted power, G_t is the antenna gain of the transmitting radar, r'_r is the distance between transmitter and target, λ is the wavelength, and G_b the antenna gain of the receiving antenna. Substituting Eqs. (2.5) and (2.6) into Eq. (2.4), the radar equation for a discrete target is

$$P_r = \frac{P_t G_t G_b \lambda^2 \sigma_b(\mathbf{s}, \mathbf{i})}{(4\pi)^3 r'^2_t r'^2_b} . \quad (2.7)$$

If the transmitting antenna is used for echo reception (monostatic case), G_b transfers to G_t and r'_b is r'_t . The bistatic scattering cross-section, σ_b , of targets within the radar sample volume can be obtained by knowing the transmitted and received power, the antenna specifications, and the propagation distance ($r'_t + r'_b$).

2.3.2 Detection of spherical targets

A single radar sample volume can contain targets of different shapes, sizes (e.g. prolate or oblate spheroid), and dielectric constants. Many forms are so complex that no analytical solutions can be found to describe the scattering process. Therefore, the focus is solely on the scattering of those spherical particles whose radii are smaller than

⁷For monostatic radars measuring only information from the backscattering process, $\sigma_b(\mathbf{s}, \mathbf{i})$ is called backscattering cross-section.

0.07 of the radar wavelength⁸ (Rayleigh approximation). Furthermore, only electric-field vectors polarized linearly having a horizontal, vertical, 45°, or 135° orientation will be considered.

The spherical particle behaves like a Hertz dipole oscillating synchronously and in the same direction as electric field vector after being induced by the polarized electromagnetic wave. For Rayleigh scattering, the scattered radiation will be polarized in the same way as the dipole, i.e. if the transmitted wave is vertically-polarized then the scattered wave is also vertically-polarized. The scattered intensity of a vertically-polarized transmitted electro-magnetic wave can then be described by a radiation pattern as shown in Fig. 2.7.

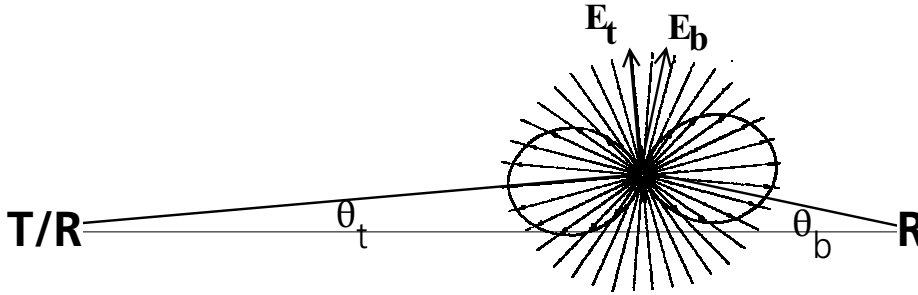


Figure 2.7: A vertical cross-section along the baseline of the radiation diagram of a Hertz oscillator (Rayleigh scattering) for vertically-polarized transmission. The radiation diagram is rotationally symmetric along the axis of the dipole. \mathbf{E}_t indicates the electric field vector of the transmitted wave, while \mathbf{E}_b is the electric field vector of the emitted wave. The elevation angles of the monostatic transmitter and bistatic receiver are θ_t , θ_b , respectively.

The geometrical view of the scattering process in a Cartesian-coordinate system⁹ xyz at ground level is illustrated in Fig. 2.8: The linearly polarized incident wave propagating along the positive y -axis has its electric field vector \mathbf{E} (induced dipole) oriented in the xz plane. The polarization of the incident wave with respect to the xy -plane is expressed by the angle χ . The scattering plane is the xy plane for scattering at ground level (Fig. 2.8). If the target hit by the electro-magnetic wave is located above ground level ($\theta_t > 0$, $\omega \neq 0$), the scattering plane is no longer at the xy plane. In fact, it has to be rotated from the xy plane to the plane which faces towards the bistatic receiver. The rotation axis is y . In both cases, the scattering plane spans both the continuing incident ray and the ray scattered towards the receiver. The direction of scatter is then defined by the forward scattering angle¹⁰, δ , as

$$\delta = \pi - \gamma = \pi - \cos^{-1} \left(\frac{b^2 - r_t'^2 - r_b'^2}{-2 r_t' r_b'} \right) . \quad (2.8)$$

⁸Battan (1973), p. 40

⁹This coordinate system is independent from the one introduced in Sec. 2.2.

¹⁰Note that the scattering matrix is formulated in the forward scatter alignment convention formulated by van Zyl & Ulaby (1990).

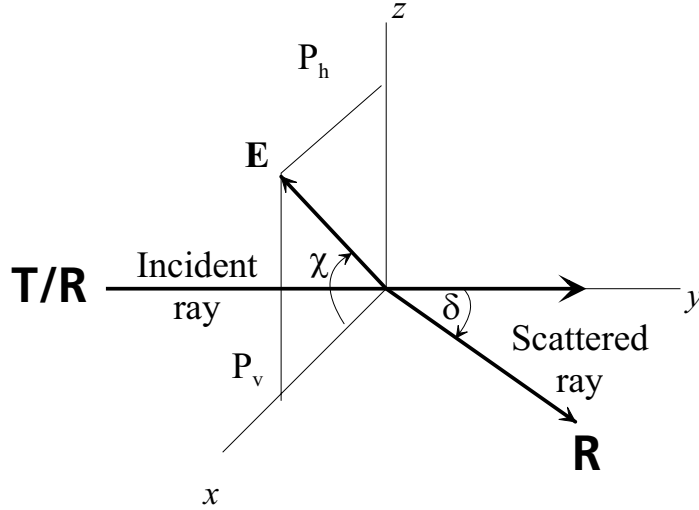


Figure 2.8: Geometry for Rayleigh scattering of electro-magnetic waves at ground level, $\omega = 0$, (Kerker, 1969). The horizontal and vertical components related to \mathbf{E} of induced dipole are P_h and P_v . A detailed explanation is given in the text.

The distance between transmitter–target, target–receiver, and receiver–transmitter are indicated by r'_t, r'_b, b , respectively.

For a periodic field such as the electro-magnetic waves, a flux of energy crossing a unit area per unit time is given by the Poynting vector $\mathbf{S} = \mathbf{E} \times \mathbf{H}$ (Kerker, 1969). Since the magnetic and electric field vectors, \mathbf{H} and \mathbf{E} , and the direction of propagation are orthogonal to each other, the Poynting vector is along the propagation direction and represents the intensity of the wave, I (Kerker, 1969). In studies of electro-magnetic wave propagation in radar meteorology, the power flux is studied usually in terms of the electric-field intensity, \mathbf{E} (Battan, 1973). By taking the appropriate time average of the Poynting vector, the flow of energy (intensity) crossing a unit area along the direction of propagation is denoted as

$$I = \frac{|\mathbf{E}|^2}{2Z_0} . \quad (2.9)$$

The quantity Z_0 is called the intrinsic impedance of the medium for plane waves (Kerker, 1969) and $|\mathbf{E}|$ is the amplitude of the electric field.

The electro-magnetic wave, intercepted by the target, is reradiated according to the size and shape of the particle as well as according to the polarization of the transmitted wave.

For an incident linearly polarized electro-magnetic wave of unit intensity, the wave scattered at a spherical target consist of two linearly polarized components (described for the two-dimensional case by Kerker (1969), pp. 35) and can be written as

$$I_{\perp}(\chi) = \frac{\pi^4 D^6}{4 r_b'^2 \lambda^4} \left(\frac{m^2 - 1}{m^2 + 2} \right)^2 \sin^2(\chi) \quad (2.10)$$

$$I_{\parallel}(\chi) = \frac{\pi^4 D^6}{4 r_b'^2 \lambda^4} \left(\frac{m^2 - 1}{m^2 + 2} \right)^2 \cos^2(\chi) \cos^2(\delta) \quad . \quad (2.11)$$

Herein, λ is the wavelength, D the diameter of the sphere, r_b' the distance between target and receiver, and m the relative refractive index. The intensities I_{\perp} and I_{\parallel} refer to the scattering plane and not to the coordinate system of a fixed bistatic antenna on the earth's surface. At low elevation angles, the resulting differences are negligible.

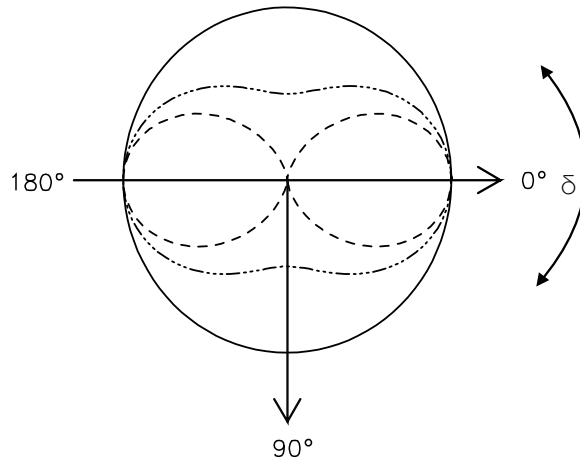


Figure 2.9: Radiation diagram for Rayleigh scattering in the scattering plane. The radius vector to each curve is proportional to the intensity scattered at the corresponding forward scattering angle, δ . The solid line signifies the radiation pattern for polarization transmitted vertically, the dashed line stands for transmitted horizontal polarization, and the dotted-dashed line represents linear $45^\circ/135^\circ$ transmitted polarization. The incident wave propagates from the left to the right. The particle is depicted in the center.

For bistatic three-dimensional scattering, the polarization angle χ as defined by the polarization of the electro-magnetic wave φ_t ($\varphi_t = 0$ for horizontal; $\varphi_t = \pi/2$ for vertical polarization) and the angle of rotation ω between the scattering plane and the plane facing towards the receiver, are denoted as

$$\chi = \varphi_t + \omega \quad (2.12)$$

$$\omega = \pi/2 - \arccos \left(\frac{\tan(\theta_t) \cos(\alpha_h)}{\sqrt{1 + \cos^2(\alpha_h) [\tan^2(\theta_t) - 1]}} \right) \quad . \quad (2.13)$$

The elevation angle of the transmitting antenna is θ_t and α_h represents the angle between the distance transmitter-target and transmitter-receiver projected onto the horizontal plane (cf. Fig. 2.2).

For Rayleigh–approximation, the scattering cross–section of a sphere can be expressed (Rinehart (1999), p. 70) by

$$\sigma = \frac{\pi^5 D^6}{\lambda^4} \left(\frac{m^2 - 1}{m^2 + 2} \right) . \quad (2.14)$$

Substituting Eq. (2.14) into Eqs. (2.10) and (2.11), the received intensity can be derived into a part perpendicular to the scattering plane ($\sigma_{b\perp}$) and a part parallel to the scattering plane ($\sigma_{b\parallel}$). Close to the ground Eq. (2.10) and Eq. (2.11) can be approximated as

$$I_{\perp}(\chi) = \frac{\sigma \sin^2(\chi)}{4\pi r_b'^2} = \frac{\sigma_{b\perp}(\mathbf{s}, \mathbf{i})}{4\pi r_b'^2} \quad (2.15)$$

$$I_{\parallel}(\chi) = \frac{\sigma \cos^2(\chi) \cos^2(\delta)}{4\pi r_b'^2} = \frac{\sigma_{b\parallel}(\mathbf{s}, \mathbf{i})}{4\pi r_b'^2} . \quad (2.16)$$

When probing the atmosphere, many raindrops and cloud particles exist within the radar beam at the same time. To determine the bistatic scattering cross–section of targets within a radar sample, the scattering cross–section of an unit volume can be multiplied by the total sample volume, leading to the bistatic total cross–section

$$\sigma_t = V \sum_{vol} \sigma_b(\mathbf{s}, \mathbf{i}) . \quad (2.17)$$

For narrow–beam antennas, a Gaussian shape can be used to approximate the radiation pattern. Probert-Jones (1962) found the volume of a radar pulse to be (Rinehart & Tuttle (1981), p. 86)

$$V = \frac{\pi \Delta\Phi_t \Delta\Theta_t}{8 \ln(2)} r_t'^2 a_b . \quad (2.18)$$

The fractional term in Eq. (2.18) denotes the Gaussian shape of the radiation pattern and a factor $2 \ln(2)$ in the denominator accounts for the real beam shape. $\Delta\Phi_t$ and $\Delta\Theta_t$ represent the horizontal and vertical beam–width of the transmitting radar, and a_b signifies the length of the sample volume (for $\gamma = 0$, $a_b = a_t$).

Substituting Eqs. (2.17) and (2.18) into the radar equation for a point target enables Eq. (2.7) to give the radar equation of a beam–filling meteorological target as

$$P_r = \frac{P_t G_t G_b(\phi_b, \theta_b) \lambda^2 \Delta\Phi_t \Delta\Theta_t a_b \sum_{vol} \sigma_b(\mathbf{s}, \mathbf{i})}{512 \pi^2 \ln(2) r_b'^2} . \quad (2.19)$$

Because in the bistatic case, the received power depends on the polarization of the receiving antenna (due to the angle-dependency of the scattering process), the radar equation has to be used according to the polarization of the receiving antenna. For a vertically-polarized receiving antenna measuring close to the ground, Eq. (2.19) can be written as

$$P_r = \frac{P_t G_t G_b(\phi_b, \theta_b) \lambda^2 \Delta \Phi_t \Delta \Theta_t c \tau \sin^2(\chi) \sum_{vol} \sigma}{1024 \pi^2 \ln(2) r_b'^2 \cos^2(\gamma/2)} \quad , \quad (2.20)$$

while for a horizontally-polarized receiving antenna it would be

$$P_r = \frac{P_t G_t G_b(\phi_b, \theta_b) \lambda^2 \Delta \Phi_t \Delta \Theta_t c \tau \cos^2(\chi) \cos^2(\delta) \sum_{vol} \sigma}{1024 \pi^2 \ln(2) r_b'^2 \cos^2(\gamma/2)} \quad . \quad (2.21)$$

If transmitter and receiver are collocated (monostatic case), the receiving antenna polarized vertically, and $a_b = a_t = (c\tau)/2$, Eqs. (2.20) and (2.21) reduce to the radar equation for monostatic radar systems:

$$P_r = \frac{P_t G_t^2 \lambda^2 \Delta \Phi_t \Delta \Theta_t c \tau \sin^2(\varphi_t) \sum_{vol} \sigma}{1024 \pi^2 \ln(2) r_t'^2} \quad (2.22)$$

and for horizontally-polarized reception to

$$P_r = \frac{P_t G_t^2 \lambda^2 \Delta \Phi_t \Delta \Theta_t c \tau \cos^2(\varphi_t) \sum_{vol} \sigma}{1024 \pi^2 \ln(2) r_t'^2} \quad . \quad (2.23)$$

First, vertical polarized transmission ($\chi = \varphi_t = \pi/2$) at ground level where $\omega = 0$ is considered. For both monostatic and bistatic radar systems, no intensity is measured by the receiver equipped with a horizontally polarized antenna, as shown in Eqs. (2.20) and (2.21). Receiving with vertical polarization causes a maximum of intensity in all directions, independent of δ as illustrated in the radiation diagram in Fig. 2.9 (solid line).

Equation (2.20) and Eq. (2.21) show that, if the transmitted wave is polarized horizontally ($\chi = \varphi_t = 0$, $\omega = 0$), no voltage (and as a result no Doppler shift) will be received at the bistatic receiver equipped with a vertically polarized antenna, while the intensity received with horizontal polarization depends on δ as exhibited in Fig. 2.9 (dashed line). No intensity is scattered at the angle $\delta = 90^\circ$ (as indicated in Fig. 2.9).

Above ground level ($\omega \neq 0$), the intensity of \mathbf{E} scattered towards a bistatic receiver is always lower than the intensity scattered backwards to the monostatic receiver (de Elia & Zawadzki, 2000). This intensity reduction is negligible for transmitting and receiving both with vertical polarization at lower elevations.

Weather radars without polarization diversity are usually equipped to transmit a linear horizontally-polarized wave (Gekat, 1998), because the backscattering cross-section of raindrops is larger for a horizontal than for vertical polarized transmission, while the backscattering cross-section for hail is independent of the transmitted polarization. Since an electro-magnetic wave is transmitted with a certain polarization, and the bistatic antenna, usually a slotted wave guide, can receive only one polarization, the electro-magnetic wave should be transmitted using vertical polarization. For measurements with non-collocated transmitter and receiver, the receiving antenna should always be constructed to receive vertical polarization.

2.4 Normalized power

In radar meteorology, the measurements of Doppler shift are related to the particle velocity, while the measured power is used to obtain information about the scattering properties of the particles within the sample volume.

Reflectivity, η , is the general radar terminology for the scattering cross-section with $\eta = \sum_{vol} \sigma_b(\mathbf{s}, \mathbf{i})$ (Doviak & Zrnicek (1984), p. 58). The radar equation for a beam-filling meteorological target coupled with a vertically-polarized receiving antenna [Eq. (2.20)] is transposed to reflectivity as

$$\sum_{vol} \sigma_b(\mathbf{s}, \mathbf{i}) = c_1 \frac{P_r r_b'^2 \cos^2(\gamma/2)}{G_b(\phi_b, \theta_b) \sin^2(\chi)} \quad \text{with} \quad (2.24)$$

$$c_1 = \frac{1024\pi^2 \ln(2)}{P_t G_t \lambda^2 \Delta\Phi_t \Delta\Theta_t c\tau} \quad ,$$

where c_1 is the radar constant including the fixed parameters of the transmitting radar system and P_r is the power measured by the bistatic receiver. For most weather radar systems ($\lambda \geq 3$ cm), almost all raindrops can be considered small compared to the transmitted wavelength, thus the Rayleigh approximation holds (Rinehart, 1999). The scattering cross-section of spheres within the sample volume is given by

$$\sum_{vol} \sigma_b(\mathbf{s}, \mathbf{i}) = \frac{\pi^5 |K|^2 \sum_{vol} D^6}{\lambda^4} \quad , \quad (2.25)$$

where $|K|$ is the magnitude of the parameter related to the complex index of refraction, depending on the particle material, its temperature, and the transmitted wavelength (Battan, 1973). While temperature and wavelength dependency is not very great, dependency on the material is. For water $|K|^2$ is usually taken at a value of 0.93, and for ice $|K|^2 = 0.179$ (Battan, 1973).

The reflectivity factor, z , in mm^6m^{-3} is defined as $z = \sum_{vol} D^6$. Substituting z and Eq. (2.25) into Eq. (2.24) leads to

$$z = c_2 \frac{P_r r_b'^2 \cos^2(\gamma/2)}{G_b(\phi_b, \theta_b) \sin^2(\chi)} \quad \text{with} \quad (2.26)$$

$$c_2 = c_1 \frac{\lambda^4}{\pi^5 |K|^2} \quad ,$$

where c_2 is a constant.

The radar signal is transmitted towards the reflector (e.g. Cassegrain antenna with a parabolic reflector) and then reflected and directed away from the radar. The pulse shape and the shape of the reflector determine the shape of the antenna-beam pattern. The antenna gain¹¹, $G(\phi, \theta)$, can be formularized as being a product of the antenna gain along the beam axis, G_0 , and the normalized antenna-gain pattern function, $f^2(\phi, \theta)$, describing the one-way radiation pattern, as

$$G(\phi, \theta) = G_0 f^2(\phi, \theta) \quad . \quad (2.27)$$

In the monostatic case, $G(\phi, \theta)$ can be assumed to be constant because the signal is transmitted and received through the same antenna pattern.

In the bistatic case, the receiving antenna is fixed with a broad azimuthal aperture, while the narrow-beam transmitting antenna rotates. The antenna patterns are different. Because a pencil-beam with a beam-width of 3 dB is used for transmission, the dependency on the transmitted antenna pattern is less pronounced. The received power depends more on the antenna pattern of the bistatic antenna at ϕ_b and θ_b . Therefore, the exact knowledge of the received power pattern is required. Measurements of $f^2(\phi_b, \theta_b)$ at different elevations obtained at the DLR antenna range are presented in Sec. 3.2, Fig. 3.3, but the three-dimensional pattern is not available. Correction of the received power with an approximated antenna pattern will produce unrealistic features (de Elia, 2000). As a result, as long as the three-dimensional power pattern of the bistatic antenna is unknown, the product between reflectivity factor and receive antenna pattern is defined as the normalized power, z_b , and can be written as

$$z_b = z G_b(\phi_b, \theta_b) = c_2 \frac{P_r r_b'^2 \cos^2(\gamma/2)}{\sin^2(\chi)} \quad . \quad (2.28)$$

Because the reflectivity factor ranges from very low values in fog (perhaps $0.001 \text{ mm}^6 \text{ m}^{-3}$) to very large values in hailstorms (perhaps $1\,000\,000 \text{ mm}^6 \text{ m}^{-3}$), logarithmic values are used to replace linear values. The logarithmic normalized power in dBZ, Z_b , is called bistatic reflectivity factor and is given as

¹¹ *The gain of an antenna is the ratio of the power received at a specific point in space at the center of the beam axis with the radar reflector in place to the power that would be received at the same point from an isotropic antenna [cited from the glossary by (Rinehart, 1999)].*

$$Z_b = 10 \log \left(\frac{z_b}{1 \cdot \text{mm}^6 \text{m}^{-3}} \right) . \quad (2.29)$$

2.4.1 Minimum detectable equivalent reflectivity factor

The power measured by a vertically-polarized bistatic antenna depends on the technical specifications of the radar systems, the bistatic scattering cross-section of the target, and the locations of transmitter, target, and receiver [cf. Eq. (2.20) and Eq. (2.21)]. In this section, the impact of the transmitted polarization on the received bistatic reflectivity factor Z_b is investigated. The minimum detectable signal strength of the bistatic receiver is 10^{-14} W. By substituting $P_r = 10^{-14}$ W into Eq. (2.28), the minimum detectable reflectivity factor, $Z_{b_{\min}}$, can then be calculated using Eqs. (2.28) and (2.29) as well as the technical specifications of the DLR system (Appendix A).

Wurman et al. (1993) showed the spatial distribution of $Z_{b_{\min}}$ at different elevations using vertically- and horizontally-polarized transmission and vertically-polarized reception. The horizontal distribution of the power, measured by the bistatic receiver, was also investigated by de Elia (2000) for a uniform reflectivity field for linear horizontally and vertically polarized transmission and vertically-polarized reception. Wurman et al. (1993) and de Elia (2000) showed that vertically-transmitted and received polarization is optimal at lower elevations.

Here, it is investigated if a vertically-polarized antenna slanted linear polarization oriented at $45^\circ/135^\circ$, which can be transmitted by POLDIRAD, will reduce $Z_{b_{\min}}$ compared to vertical transmission.

As a result, at low elevations, the lowest values of $Z_{b_{\min}}$ will be achieved with a vertically-polarized transmitting and receiving antenna. At higher elevations, however, slanted linear polarization oriented at $45^\circ/135^\circ$ is favorable to achieve low values of $Z_{b_{\min}}$.

Figure 2.10 exhibited the horizontal distribution of $Z_{b_{\min}}$ measured by the bistatic receiver at an elevation of 9 km for vertically- and $45^\circ/135^\circ$ -polarized transmission.

For those regions where θ_b is high and for measurements close to the bistatic receiver, slanted linear polarization oriented at $45^\circ/135^\circ$ gives an improvement in sensitivity of about 5 dBZ – 10 dBZ, when compared to a transmitted wave vertically polarized. This advantage when using slanted linear polarization should always be taken into account when measuring at high elevations (e.g., with $\Delta\Phi_b = 20 - 25^\circ$ – antennas) in either light rain or clear-air conditions. Note that the antenna gain reduces as the antenna aperture increases. Therefore for the sensitivity of the receiver, the polarization of the transmitted electro-magnetic wave plays an important role.

2.5 Sidelobe contamination

Most antennas installed at weather radar systems are directional; which means, they focus the energy into a particular direction and not sending radiation equally in

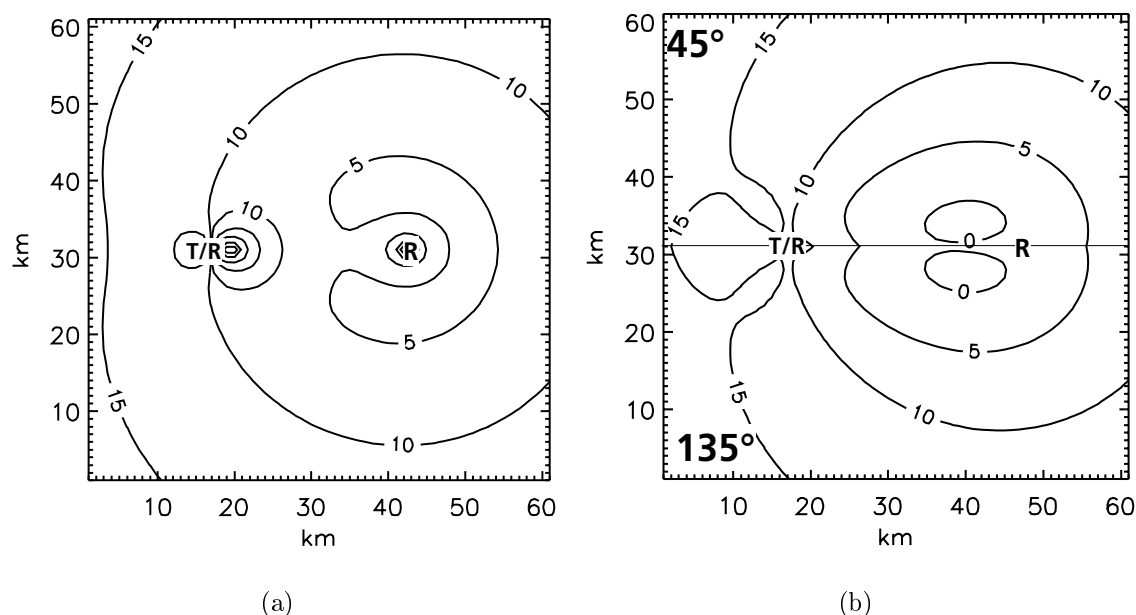


Figure 2.10: Horizontal cross-section at 9 km height of the $Z_{b_{\min}}$ -distribution in dBZ measured by the vertically-polarized bistatic receiver for (a) vertically-polarized transmission and (b) $45^\circ/135^\circ$ transmitted polarization.

all directions like antennas with an isotropic antenna power pattern. The directional transmission and reception lead to a higher antenna gain (Sec. 2.4) and make locating targets in space possible. As already addressed in Sec. 2.4, the radar signal is sent towards the reflector, then reflected and sent away from the radar. The shape of the reflector determines the shape of the antenna beam pattern (Rinehart, 1999). In an ideal transmitting antenna-pattern all energy would be focused into a single direction and none of it would go anywhere else. This is physically impossible. Real radar antennas will also transmit and receive energy off to the side of the mainlobe which are called sidelobes. The sidelobes exist in all directions away from the mainlobe and are different from one direction to another.

The offset fed paraboloid antenna installed at POLDIRAD has an antenna beam pattern as illustrated in Fig. 2.11. The main power is sent in the direction the antenna is pointing. A secondary maximum of power appears at an angle of about 1.7° in azimuthal and about 4.5° in vertical direction from the first power maximum, with a reduction of about 32 dB and 37 dB, respectively, compared to the main power. For a monostatic radar system, the scattered power is received with the same antenna power pattern, while in the bistatic case, the signal is received at a remote site by antennas with a wide angular aperture (i.a. $\Delta\Phi_b = 60^\circ$, $\Delta\Theta_b = 8^\circ$, or $\Delta\Theta_b = 22^\circ$). The wide angular aperture is necessary to sample along the transmitted beam and, therewith, cover a large spatial area. Because the pulse travels with the speed of light, the antenna cannot be rotated along the propagation path. The power pattern

of a vertically-polarized bistatic receiving antenna is given in Fig. 3.3.

For a monostatic radar system the effect of sidelobe contamination is illustrated in Fig. 2.12(a), using a narrow-beam transmitting and receiving antenna. Figure 2.12(b) exhibits sidelobe contamination in a bistatic radar system using a narrow-beam transmitting and a wide-beam receiving antenna. The power pattern of the transmitting antenna is indicated schematically by the main lobe and the first sidelobe.

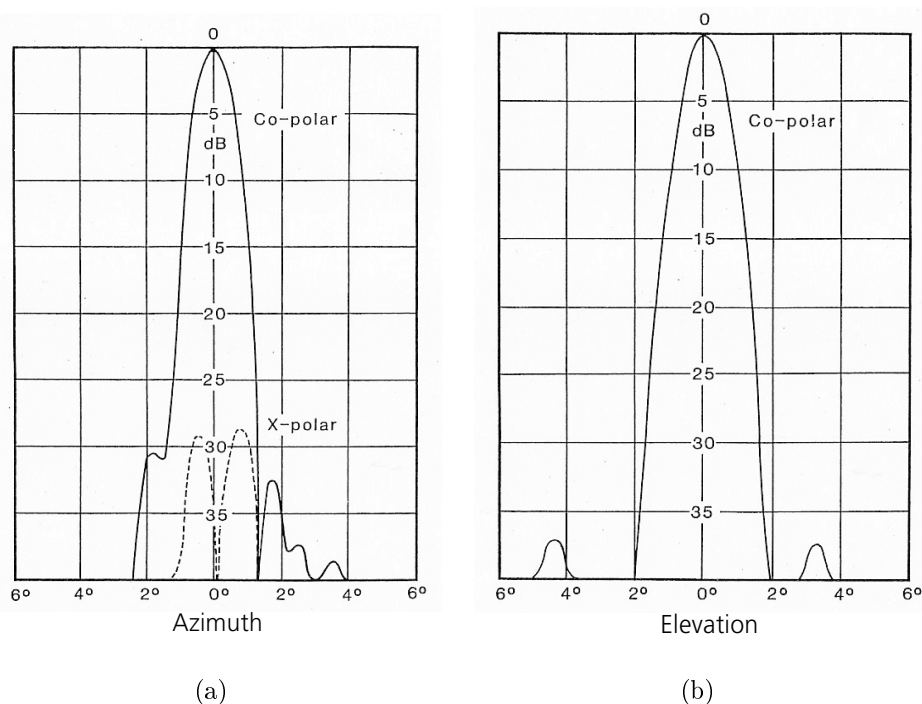


Figure 2.11: One-way power-pattern of the POLDIRAD antenna in dB for transmitted vertical polarization. (a) Receiving power-pattern sampled in an azimuthal direction with receiving vertical (Co-polar) and horizontal (X-polar) polarization. (b) Receiving power-pattern sampled in vertical direction with received vertical (Co-polar) polarization (Schroth et al., 1988).

All signals arriving at the receiver at the same time (propagation is indicated by dotted lines in Fig. 2.12) are located at the same surfaces of constant delay (sphere or ellipsoid), because they have the same propagation length which is $2r'_t$ for the monostatic and $r'_t + r'_b$ for the bistatic reception. These signals are assigned to the area, where the main beam points and to the corresponding sample time (signal processing is described in more detail in Appendix B). Therefore, if an area is hit by a sidelobe of the transmitted power pattern (illustrated as light gray area in Fig. 2.12), the receiver measures the power scattered by targets, which are illuminated by the main beam, plus the power scattered by targets, which are illuminated by sidelobe, because both signals have the same propagation time. All signals arriving at the receiver at a given time are assigned to an area where the main beam is pointing

(ϕ_t, θ_t) and to the corresponding surface of constant delay for that time (hatched area in Fig. 2.12). In radar systems using narrow-beam antennas, the contamination due to sidelobes is normally negligible, because the signal sent through the weak sidelobe is received by that same weak sidelobe. POLDIRAD receives a signal from a target, illuminated by the sidelobe, with the same power as a target, illuminated by the mainlobe, which reflectivity is 60 dB weaker. In contrast to the monostatic case, in bistatic systems sidelobe contamination cannot be ignored. In the bistatic case, the signal sent through the sidelobe can be received within the mainlobe of the bistatic antenna.

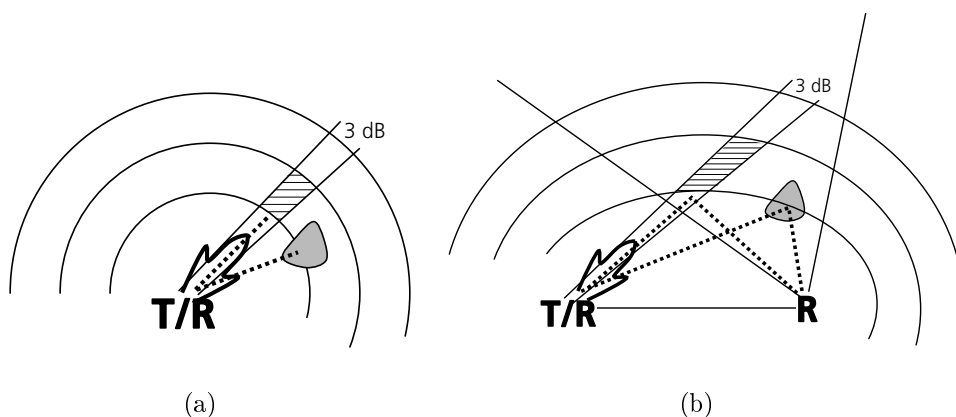


Figure 2.12: Schematic view of the effect of sidelobe contamination at a (a) monostatic radar (T/R) and (b) bistatic receiver (R). The degree of contamination depends on the power pattern of the transmitting and receiving antennas. All signals arriving at the receiver at a given time are assigned to an area where the main beam is pointing and to the corresponding surface of constant delay for that time (hatched area). The 3 dB beamwidth of the monostatic radar and the angular aperture of 60° of the bistatic antenna are indicated.

The degree of contamination in the data measured by the bistatic receiver depends strongly on the weather conditions, the beam pattern of the transmitting radar, and the power pattern of the receiving antenna. The problems involved in data contamination, which arose due to the transmission of sidelobes by the transmitting radar, were investigated by de Elia & Zawadzki (2000) using the bistatic radar system at McGill University, Montreal, Canada. They constructed a model to simulate reflectivity that was measured by the bistatic receiver. The simulated reflectivity fields were used as a tool to discriminate between non-contaminated data (simulated) and contaminated data (measured) which was demonstrated by reflectivity as well as Doppler velocity measurements during different weather situations. Heavy contamination was found in areas where a strong reflectivity gradient was present, e.g. around a core of a convective storm. In a stratiform case, contamination appeared in regions above the melting layer, indicated by the bright band. The degree of contamination was calculated. It was then used as a weight in the cost function of the constraining model (cf.

Sec. 5) so that Doppler velocities in regions where high contamination exists have a small impact on the retrieved wind–field.

The transmitted beam pattern of the McGill S-band radar has the first sidelobe as being about 22 dB below the mainlobe in 1.5° azimuthal direction [Fig. 4 in de Elia & Zawadzki (2000)], while POLDIRAD has a suppression in the sidelobes of about 32 dB, at an azimuth angle of about 1.7° (Fig. 2.11). Therefore, assuming an uniform receiving power pattern, the bistatic antenna receives a signal from a target illuminated by the sidelobe with the same power as a target illuminated by the mainlobe, if the reflectivity differences exceed 32 dB per about 1.7° in azimuthal direction. In general, sidelobe appearances can be suppressed in the first place if a transmitted power pattern is constructed with a very low sidelobe suppression.

With the help of the reflectivity measured by the monostatic receiver, the power field measured by the bistatic receiver could be corrected (cf. Sec. 4.4.3). No correction can be done for the Doppler velocity (de Elia & Zawadzki, 2000) because each receiver measures only one component of the wind–vector. As long as the true wind–vector is unknown, the Doppler velocity cannot be corrected or reconstructed.

2.6 Determination of the horizontal wind–field

Estimates of the wind–vector field by monostatic multiple–Doppler radar systems have been performed for more than 30 years, e.g. by Bohne & Srivastava (1976); Ray et al. (1978, 1980); Ray & Sangren (1983). The fundamental early works were summarized during a workshop about monostatic multiple–Doppler radar systems (Carbone et al., 1980).

To estimate the three components of the wind–vector, independent measurements by three Doppler radar systems are necessary. These can be either monostatic or bistatic radar systems. As shown by Wurman et al. (1993), the direct determination of the vertical wind–component, w , is very inaccurate at low elevations, because the part of the vertical component of the wind velocity is small in the measured Doppler velocity for $1^\circ \leq \theta_b \leq 8^\circ$, corresponding to $0.02w \leq \sin(\theta_b)w \leq 0.14w$ [cf. Eq. (2.2)]. It seems more appropriate to integrate the vertical velocity from the horizontal wind–field. Recent studies using variational analysis [e.g. Protat & Zawadzki (1999); Montmerle et al. (2001); Nissen et al. (2001)] show reliable results.

Therefore, the direct determination of the wind–field is limited to the horizontal wind–vector field. The vertical component will be retrieved in Sec. 5 using a constraining model based on a variational analysis method (Protat & Zawadzki, 1999).

The measured Doppler velocities v_e and v_t can be separated into the horizontal wind–components u, v , as demonstrated in Eqs. (2.2) and (2.3), disregarding w .

Here, a general version of the horizontal wind–vector field determination is presented for all kinds of multiple–Doppler velocity–processing, i.e. dual–Doppler, triple–Doppler and so on. For horizontal wind–field determination, one transmitting source and at least two receivers are necessary. With two measured Doppler velocities, the equation system to calculate the horizontal wind–vector field is exactly determined (Eq. (2.2) and Eq. (2.3), disregarding w).

A bistatic Doppler radar system consists usually of one monostatic transmitting and receiving radar system and several bistatic receivers. In a bistatic network consisting of n receivers ($n \geq 2$), n Doppler velocities, v_{m_n} , are measured. This leads to an overdetermined equation system that can be written as

$$\begin{pmatrix} \frac{\sin(\phi_{b_1}) \cos(\theta_{b_1}) + \sin(\phi_t) \cos(\theta_t)}{2 \cos(\gamma_1/2)} & \frac{\cos(\phi_{b_1}) \cos(\theta_{b_1}) + \cos(\phi_t) \cos(\theta_t)}{2 \cos(\gamma_1/2)} \\ \frac{\sin(\phi_{b_2}) \cos(\theta_{b_2}) + \sin(\phi_t) \cos(\theta_t)}{2 \cos(\gamma_2/2)} & \frac{\cos(\phi_{b_2}) \cos(\theta_{b_2}) + \cos(\phi_t) \cos(\theta_t)}{2 \cos(\gamma_2/2)} \\ \vdots & \vdots \\ \frac{\sin(\phi_{b_n}) \cos(\theta_{b_n}) + \sin(\phi_t) \cos(\theta_t)}{2 \cos(\gamma_n/2)} & \frac{\cos(\phi_{b_n}) \cos(\theta_{b_n}) + \cos(\phi_t) \cos(\theta_t)}{2 \cos(\gamma_n/2)} \end{pmatrix} \begin{pmatrix} u \\ v \end{pmatrix} = \begin{pmatrix} v_{m_1} \\ v_{m_2} \\ \vdots \\ v_{m_n} \end{pmatrix} \quad (2.30)$$

with ϕ_{b_i}, θ_{b_i} being azimuth and elevation angles at the i 'th bistatic receiver. The azimuth and elevation angle of the transmitting radar are ϕ_t, θ_t , respectively. The scattering angle at the respective bistatic Doppler radar system related to the i 'th bistatic receiver is denoted by γ_i .

This overdetermined equation system can be solved in a least square sense. Therefore, the normal equations are solved as

$$\underbrace{\begin{pmatrix} a_{11} & a_{12} \\ a_{21} & a_{22} \end{pmatrix}}_A \begin{pmatrix} u \\ v \end{pmatrix} = \begin{pmatrix} b_1 \\ b_2 \end{pmatrix}, \quad (2.31)$$

where

$$\begin{aligned} a_{11} &= \sum_{i=1}^n \left(\frac{\sin(\phi_{b_i}) \cos(\theta_{b_i}) + \sin(\phi_t) \cos(\theta_t)}{2 \cos(\gamma_i/2)} \right)^2 \\ a_{12} = a_{21} &= \sum_{i=1}^n \left(\frac{\cos(\phi_{b_i}) \cos(\theta_{b_i}) + \cos(\phi_t) \cos(\theta_t)}{2 \cos(\gamma_i/2)} \frac{\sin(\phi_{b_i}) \cos(\theta_{b_i}) + \sin(\phi_t) \cos(\theta_t)}{2 \cos(\gamma_i/2)} \right) \\ a_{22} &= \sum_{i=1}^n \left(\frac{\cos(\phi_{b_i}) \cos(\theta_{b_i}) + \cos(\phi_t) \cos(\theta_t)}{2 \cos(\gamma_i/2)} \right)^2 \\ b_1 &= \sum_{i=1}^n v_{m_i} \frac{\sin(\phi_{b_i}) \cos(\theta_{b_i}) + \sin(\phi_t) \cos(\theta_t)}{2 \cos(\gamma_i/2)} \\ b_2 &= \sum_{i=1}^n v_{m_i} \frac{\cos(\phi_{b_i}) \cos(\theta_{b_i}) + \cos(\phi_t) \cos(\theta_t)}{2 \cos(\gamma_i/2)}. \end{aligned}$$

The solution of Eq. (2.30) is given as

$$\begin{pmatrix} u \\ v \end{pmatrix} = \frac{1}{\det(A)} \begin{pmatrix} a_{22} & -a_{12} \\ -a_{12} & a_{11} \end{pmatrix} \begin{pmatrix} b_1 \\ b_2 \end{pmatrix}, \quad (2.32)$$

where

$$\det(A) = a_{11}a_{22} - a_{12}^2 \quad . \quad (2.33)$$

The horizontal wind-field can be calculated with

$$u = \frac{1}{\det(A)} \left(a_{22}b_1 - a_{12}b_2 \right) \quad (2.34)$$

$$v = \frac{1}{\det(A)} \left(a_{11}b_2 - a_{12}b_1 \right) \quad . \quad (2.35)$$

The Doppler velocities can be measured by both monostatic and/or bistatic receivers. If the Doppler velocity measurement is achieved by a monostatic Doppler radar, the geometrical parameters change to $\phi_b = \phi_t, \theta_b = \theta_t$, and $\gamma = 0$ as demonstrated in Eq. (2.3).

Generally, wind-vector fields can be estimated either from at least two monostatic receivers (**Case 1**), from one monostatic and at least one bistatic receiver (**Case 2**), or from at least two bistatic receivers (**Case 3**). For more than two receivers, the equation system to calculate the horizontal wind-vector field is overdetermined.

Case 1: Here, the horizontal wind-field is determined by the Doppler velocities measured by n_t monostatic Doppler radar systems ($v_{m_i} = v_{t_j}$). Therefore, azimuth and elevation angles of transmitter and receiver are identical ($\phi_{b_i} = \phi_{t_j}, \theta_{b_i} = \theta_{t_j}$) and $\gamma = 0$. Using, v_{t_j} , measured with the j th monostatic Doppler radar system, the horizontal wind can be calculated from Eq. (2.34) and Eq. (2.35) as

$$u = \frac{1}{\det(A)} \left[\sum_{j=1}^{n_t} \left(v_{t_j} \sin(\phi_{t_j}) \cos(\theta_{t_j}) \sum_{j=1}^{n_t} \cos^2(\phi_{t_j}) \cos^2(\theta_{t_j}) \right) - \sum_{j=1}^{n_t} \left(v_{t_j} \cos(\phi_{t_j}) \cos(\theta_{t_j}) \sum_{j=1}^{n_t} \sin(\phi_{t_j}) \cos(\phi_{t_j}) \cos^2(\theta_{t_j}) \right) \right] \quad (2.36)$$

$$v = \frac{1}{\det(A)} \left[\sum_{j=1}^{n_t} \left(v_{t_j} \cos(\phi_{t_j}) \cos(\theta_{t_j}) \sum_{j=1}^{n_t} \sin^2(\phi_{t_j}) \cos^2(\theta_{t_j}) \right) - \sum_{j=1}^{n_t} \left(v_{t_j} \sin(\phi_{t_j}) \cos(\theta_{t_j}) \sum_{j=1}^{n_t} \sin(\phi_{t_j}) \cos(\phi_{t_j}) \cos^2(\theta_{t_j}) \right) \right] \quad (2.37)$$

where

$$\det(A) = \sum_{j=1}^{n_t} \left(\sin^2(\phi_{t_j}) \cos^2(\theta_{t_j}) \sum_{j=1}^{n_t} \cos^2(\phi_{t_j}) \cos^2(\theta_{t_j}) \right) - \left(\sum_{j=1}^{n_t} \cos(\phi_{t_j}) \sin(\phi_{t_j}) \cos^2(\theta_{t_j}) \right)^2 \quad . \quad (2.38)$$

Case 2: A bistatic multiple-Doppler radar network consists of only one monostatic transmitting/receiving Doppler radar system and $n - 1$ bistatic receivers. The radial velocity measured by the monostatic receiver is set to be $v_{m_1} = v_t$ and $i = 1$, while all Doppler velocities measured by the i 'th bistatic receiver, with $v_{m_i} = v_{e_i}$, are counted with $i \geq 2$. This has to be considered when using Eq. (2.34) and Eq. (2.35) to calculate u and v .

Case 3: Here, the monostatic radar system acts only as a transmitting source. The horizontal wind-field can be determined with at least two bistatic receivers. Hereby, the number of bistatic receivers is n ($n \geq 2$) and the Doppler velocity measured by the i 'th bistatic receiver is set to $v_{m_i} = v_{e_i}$. This affords an opportunity to derive wind-vector fields even when the transmitting radar system can not measure the phase of the received wave (only the phase of the transmitted wave has to be measured). This is a cheap and easy solution to measure horizontal wind-fields, without having to replace existing radar by a Doppler radar.

2.7 Accuracy of the wind-field determination

Apart from the influence of instrumentation effects and meteorological parameters on the accuracy of the wind-field determination, the accuracy of the wind-field is also affected by the location of transmitter, receiver, and target (defined by γ) and the number of Doppler velocity measurements, v_{m_n} , achieved in the same area by n receivers. The influences of instrumentation effects, signal processing, and meteorological parameters on the quality of the wind-field are similar for bistatic and for monostatic Doppler radar systems and will not be discussed in detail in this section. In this work, only the influence of γ and n on the standard deviation of the horizontal wind-field is discussed. Hereafter, the standard deviations of the horizontal wind-field refer exclusively to the geometrical impact.

In the following discussion, the velocity variance of the horizontal wind-field, $\sigma_{|\mathbf{V}_h|}^2$, determined by the bistatic multiple-Doppler radar network at Oberpfaffenhofen, is compared to the velocity variance achieved by the monostatic dual-Doppler wind-field processing. The latter is performed with POLDIRAD and the operational C-band Doppler radar of the German Weather Service (DWD) on Mount Hohenpeißenberg about 37 km south-west of OP (hereafter 'radar HP'). In addition, it is shown how an overdetermination of the equation system to calculate the wind-field reduces $\sigma_{|\mathbf{V}_h|}^2$ compared to dual-Doppler wind-field processing for the bistatic Doppler radar network in OP.

The variance of the estimates of (u, v) independent of the wind-velocity can be expressed by taking the second power of Eq. (2.34) and Eq. (2.35).

It is assumed that monostatic and bistatic receivers have the same variance in the Doppler velocity measurement (only instrumental error), $\sigma_{v_{m_1}}^2 = \sigma_{v_{m_2}}^2 = \dots = \sigma_{v_{m_n}}^2$.

Within a bistatic network, the measured apparent velocity, v_a , has to be projected onto the direction \mathbf{e} . Therefore, the variance of the i 'th Doppler velocity has to be projected as well, which leads to $\sigma_{v_{m_i}}^2 = \sigma_{v_{e_i}}^2 = \sigma_{v_{a_i}}^2 \cos^{-2}(\gamma_i/2)$.

In the following, the horizontal distribution of the standard deviation of the horizontal wind–velocity is discussed for **Cases 1 – 3**. Figure 2.13 illustrates the standard deviation for all three cases normalized by the radial velocity standard deviation which is for most weather radar systems 1 m s^{-1} .

The following discussion is focused on the bistatic Doppler radar network at OP. The standard deviation of the Doppler velocity measurement using POLDIRAD can be assumed to be 0.8 m s^{-1} , a value which is applied to the following discussion.

Case 1: In monostatic multiple–Doppler installation, the radial velocities, v_{t_j} , measured by each individual monostatic Doppler radar are combined [cf. Eq. (2.37) and Eq. (2.38)] to a wind–vector. The unit vectors of two v_{t_j} ’s intersect at an angle called the intersection angle. This angle is identical to the angle γ .

For monostatic dual–Doppler radar processing consisting of POLDIRAD and radar HP, the distribution of the standard deviation¹² of $\sigma'_{|\mathbf{v}_h|}$ at ground level is illustrated in Figure 2.13(a). The horizontal wind–field can be measured with a standard deviation of $1.2 \text{ m s}^{-1} - 1.6 \text{ m s}^{-1}$ within the monostatic dual–Doppler radar network. This range corresponds to an intersection angle ranging between 50° and 140° . The minimum value of $\sigma'_{|\mathbf{v}_h|}$ is at an intersection angle of 90° . If the intersection angle approaches 180° or 0° , $\sigma'_{|\mathbf{v}_h|}$ becomes infinite [cf. Fig. 2.13(a)].

Case 2: Here we discuss the accuracy of the horizontal wind–field using bistatic dual–Doppler processing consisting of POLDIRAD and the bistatic receiver system Lagerlechfeld [cf. Fig. 2.13(b)]; and bistatic quadruple–Doppler processing consisting of POLDIRAD and the three bistatic receivers at Lichtenau, Lagerlechfeld, and Ried [cf. Fig. 2.13(c)]. Within a bistatic multiple–Doppler radar system, v_e and v_t are combined. The intersection angle between these two vectors is identical to $\gamma/2$ (Fig. 2.3).

For a *bistatic dual–Doppler radar system*, the distribution of $\sigma'_{|\mathbf{v}_h|}$ is illustrated in Fig. 2.13(b). A minimum of $\sigma'_{|\mathbf{v}_h|}$ within the bistatic dual–Doppler network is reached at an intersection angle of about 100° . $\sigma'_{|\mathbf{v}_h|}$ ranges at ground level between 1.9 m s^{-1} and 3.2 m s^{-1} which is within $25^\circ \leq \gamma/2 \leq 70^\circ$. If the intersection angle, $\gamma/2$, approaches 90° or 0° , $\sigma'_{|\mathbf{v}_h|}$ becomes infinite [cf. Fig. 2.13(b)].

Additional receivers result in overdetermination of the horizontal wind–field. For *bistatic quadruple–Doppler processing*, $\sigma'_{|\mathbf{v}_h|}$ ranges from 1.2 m s^{-1} to 2.0 m s^{-1} at ground level [Fig. 2.13(c)]. These values are comparable to the standard deviation of monostatic dual–Doppler processing [Fig. 2.13(a)]. As a result, the standard deviation can be reduced by about 1 m s^{-1} in bistatic quadruple–Doppler compared to a bistatic dual–Doppler processing [cf. Figs. 2.13(b) and 2.13(c)]. The effect of an infinite $\sigma'_{|\mathbf{v}_h|}$ at $\gamma = 0^\circ$ or 90° in a dual–Doppler system is reduced in a quadruple–Doppler system because the transmitter–receiver baseline is covered by the additional receivers.

Case 3: Here, the monostatic radar acts as a transmitting source only insofar as the bistatic Doppler velocity measurements are used to determine horizontal wind–field [Fig. 2.13(d)]. Within the observation area, $\sigma'_{|\mathbf{v}_h|}$ ranges between 1.3 m s^{-1} and

¹²To avoid confusion with the standard deviation of the horizontal wind–velocity, denoted as $\sigma_{|\mathbf{v}_h|}$, the standard deviation at a certain grid–point is symbolized by $\sigma'_{|\mathbf{v}_h|}$.

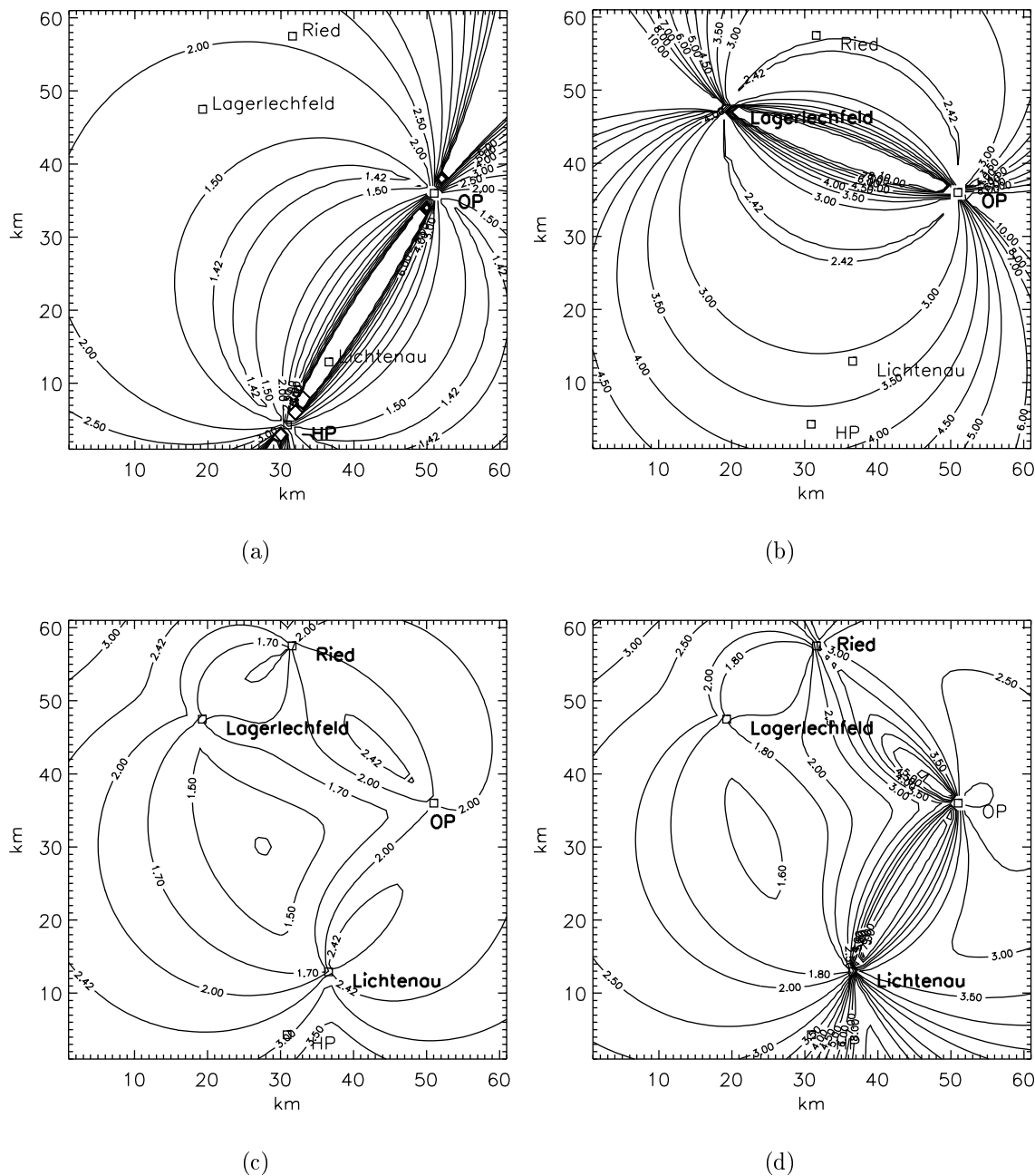


Figure 2.13: Spatial distribution of the $\sigma'_{|v_h|}$ normalized by the radial velocity standard deviation of 1 m s^{-1} for (a) monostatic dual-Doppler processing; (b) bistatic dual-Doppler processing; (c) bistatic quadruple-Doppler processing and; (d) bistatic triple-Doppler processing with only bistatic receivers. Note that the maximum contour line is set at a value of ten.

2 ms^{-1} . Within a triple-Doppler area (consisting of bistatic receivers only) $\sigma'_{|\mathbf{V}_h|}$ can be reduced by $0.5 \text{ m s}^{-1} - 1.2 \text{ m s}^{-1}$ compared to a dual-Doppler radar system [cf. Figs. 2.13(b) and 2.13(d)].

2.8 Optimal arrangement for the bistatic receiver

If the sideward scattered part of the electro-magnetic wave is measured, the position of transmitter, target, and receiver in space, indicated by the scattering angle, influences the spatial resolution, the values of σ'_{v_e} and $\sigma'_{|\mathbf{V}_h|}$, and the intensity of the received power. The area, which can be observed by a bistatic receiver, is restricted by the receiving power pattern of the bistatic antenna (more explanation in Sec. 3.2, Fig. 3.3). The main power can be received with a bistatic antenna within a horizontal aperture of about 60° . Therefore, not only the position of the receiver, but rather the bistatic antenna's view angle has to be arranged to achieve (1) high spatial resolution of the measurement; (2) high accuracy of the Doppler velocity measurement; (3) a low minimum detectable reflectivity factor, $Z_{b_{\min}}$, measurable by the bistatic receiver; and (4) high accuracy of the horizontal wind-field determination based on the combination of v_e and v_t . Figure 2.14 illustrates the dependency of both the spatial resolution and the accuracy of v_e and $|\mathbf{V}_h|$ on the scattering angle. All these four properties are discussed separately in the previous sections and are now combined to find an optimal arrangement of the bistatic receiver within a bistatic dual-Doppler radar system. The observation area can be divided into three areas with the following characteristics:

- (1) **Baseline area.** In this area, the forward-scattered part of electro-magnetic wave is detected by the bistatic receiver (Fig. 2.3, cross-hatched area, $\gamma/2 > 80^\circ$). The length of resolution volume a_b ranges from $12a_t$ up to the length of the baseline (cf. Fig. 2.5, cross-hatched area). Both standard deviations $\sigma_{v_e}, \sigma'_{|\mathbf{V}_h|}$ reach values higher than 5 m s^{-1} close to the baseline [cf. Fig. 2.13(b)]. No Doppler velocity can be measured along the baseline because of signal interferences.
- (2) **Quasi-monostatic area.** This area (Fig. 2.3, hatched area, $\gamma/2 < 10^\circ$) extends the baseline beyond the monostatic radar and the bistatic receiver. The backward scattered part of the electro-magnetic wave is measured by the bistatic receiver. The spatial resolution and the standard deviation of the Doppler velocity measurement reach their minimum (with $\sigma_{v_e}^2 \approx \sigma_{v_a}^2$) and have almost the same values as in the monostatic case [cf. Fig. 2.5]. Values of $Z_{b_{\min}} \geq 0 \text{ dBZ}$ at ground level and $Z_{b_{\min}} \geq 5 \text{ dBZ}$ at 9 km for an electro-magnetic wave transmitted vertically-polarized are required for this area to exceed the noise level of the bistatic receiver (cf. Appendix A). The wind velocity components v_e and v_t are almost identical, the intersection angle is close to 0° , and the determination of the horizontal wind vector-field is impossible due to the large error in $|\mathbf{V}_h|$ [cf. Fig. 2.13(b)].

(3) **Bistatic area.** In this area, the sideward scattered part of the electro-magnetic wave is detected by the bistatic receiver (Fig. 2.3, plain area, $10^\circ \leq \gamma/2 \leq 80^\circ$). The length of the resolution volume varies between 200 m and 1800 m (cf. Fig. 2.5) for transmitting a pulse with a length of 300 m. In this area, the bistatic resolution volume is always larger than the monostatic one. Received power depends on the distance $r_b'^2$, the size of the resolution volume [$\sim \cos^{-2}(\gamma/2)$], and on the three-dimensional scattering process of the transmitted wave [$I_\perp(\chi) \sim \sin^2(\chi)$], as described in Sec. 2.3.2, Eq. (2.20). The minimum requirements to measure a signal by the bistatic receivers are values of $Z_{b_{\min}} \geq -5$ dBZ at ground and $Z_{b_{\min}} \geq 5$ dBZ at 9 km height for a vertically-polarized transmitted wave. Low standard deviation of the Doppler velocity when measured by the bistatic receiver is achieved far away from the baseline due to $\sigma_{v_e}^2 = \sigma_{v_a}^2 \cos^{-2}(\gamma/2)$ (cf. Fig. 2.14). For horizontal wind field determination, $\sigma_{|\mathbf{V}_h|}'$ varies between $2 \text{ m s}^{-1} - 3 \text{ m s}^{-1}$, with a minimum at $\gamma/2 \approx 50^\circ$ [cf. Fig. 2.13(b)].

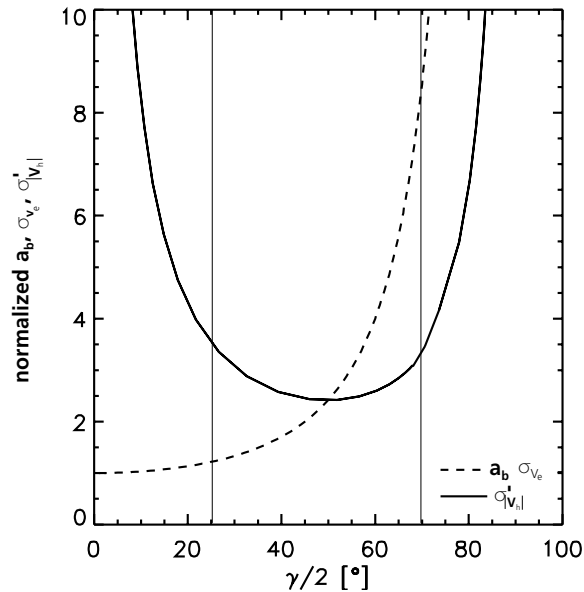


Figure 2.14: Illustration of the dependency of the resolution volume length, a_b , the standard deviations, σ_{v_e} , and $\sigma_{|\mathbf{V}_h|}'$ on the scattering angle. The parameters are normalized to the respective parameter at a monostatic radar. The scattering-angle limit of $50^\circ \leq \gamma \leq 140^\circ$ is indicated by the vertical lines.

The area with $\gamma/2$ ranging between 25° and 70° provides measurements with standard deviation of the horizontal wind-field ranging between $2 \text{ m s}^{-1} - 3 \text{ m s}^{-1}$ (for $\sigma_{v_{m_i}} = 0.8 \text{ m s}^{-1}$) and a resolution ranging between 180 m – 1200 m (for $c\tau = 300 \text{ m}$). As a result, the bistatic antenna should be positioned to observe this area. As shown in Fig. 2.14, the observation area can be extended by setting the lower limit to $\gamma/2 = 20^\circ$ or 15° . On the other hand, the bistatic antenna's view angle should not be rotated closer to the baseline.

A functional relationship is derived by de Elia & Zawadzki (2001) between the distribution of parameters such as size of the resolution volume and standard deviation of the determined wind-field. This relationship can be used to find the optimal layout of bistatic networks.

Beside the view angle of the bistatic antenna, the size of the observation area is defined by the size of the maximum sample ellipsoid together with the distance between receiver and transmitter. The maximum sample ellipsoid is a function of the sample spacing, τ_s , and the number of range-gates¹³, n_{rb} (more information on signal processing can be found in Appendix B).

The signal, measured by the bistatic receiver at a given time, is referred to an ellipsoid of constant delay, which includes all signals with the same propagation time. Since the receiver measures only every τ_s , the main axis of the maximum ellipsoid has a length of $\tau_s c n_{rb}$. If data sampling starts $5 \mu\text{s}$ (four range-gates) before the first pulse reaches the receiver, the maximum ellipsoid has a main axis length of $\tau_s c (n_{rb} - 4) + b$. In addition, the size of the observation area varies with changing the baseline distances.

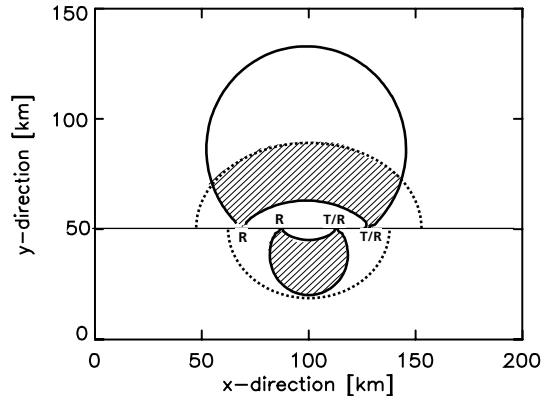


Figure 2.15: Horizontal cross-section of the maximum sample areas corresponding to a baseline length of 60 km (upper part) and to a baseline length of 30 km (lower part). This estimation is limited for both applications by a scattering-angle limit of $50^\circ - 140^\circ$ (solid line). The maximum sampled ellipses for $b = 30$ km and $b = 60$ km are signified by dotted lines. The resulting observation areas are hatched.

A horizontal cross-section of the spatial coverage depending on the baseline length is illustrated in Fig. 2.15. Here, the main axis of the maximum sample ellipsoid has a length of $b + 45.75$ km. The maximum sample ellipsoid is indicated by the dotted line in Fig. 2.15 (radar parameters are related to the DLR system with $\tau_s = 1.25 \mu\text{s}$, $n_{rb} = 126$, cf. Sec. 3 and Appendix A). The scattering angle limit of $50^\circ \leq \gamma \leq 140^\circ$ is marked by dark lines. Therefore, the investigation area is either restricted by the scattering angle limit (Fig. 2.15, lower part) or, with increasing b , by the maximum ellipsoid (Fig. 2.15, upper part). On the other hand, with increasing τ_s , the maximum ellipsoid can be enlarged. The totally-covered area at $b = 60$ km

¹³This can be limited by the bandwidth of the data transfer.

is larger than the areas achieved with $b = 30$ km. It includes also the area with a high accuracy in the horizontal wind-field determination where $\gamma = 100^\circ$ at the outer edge. Note that for $b = 60$ km measurements are only possible above a height of 0.8 km above ground level (for $r_t = 50$ km) and $z = 1.4$ km (for $r_t = 80$ km) for 1° elevation. Furthermore, the size of the sample volume increases with increasing r'_t , due to the 1° beam-width. The wind-field close to the ground can give important information about the weather development. When this wind-field is not available, the accuracy of the weather forecast becomes critical (e.g. for nowcasting of weather events, warning of severe weather, data assimilation into numerical weather prediction models) and for vertical integration of the continuity equation (boundary effects).

3 The bistatic Doppler radar network

3.1 Bistatic network design

The bistatic Doppler radar network at Oberpfaffenhofen consists of the transmitting and receiving monostatic polarimetric Doppler radar system, POLDIRAD (Schroth et al., 1988), a receiver at POLDIRAD, a central bistatic hub computer for data-processing, and several bistatic remote receiver systems as well, as illustrated in Fig. 3.1.

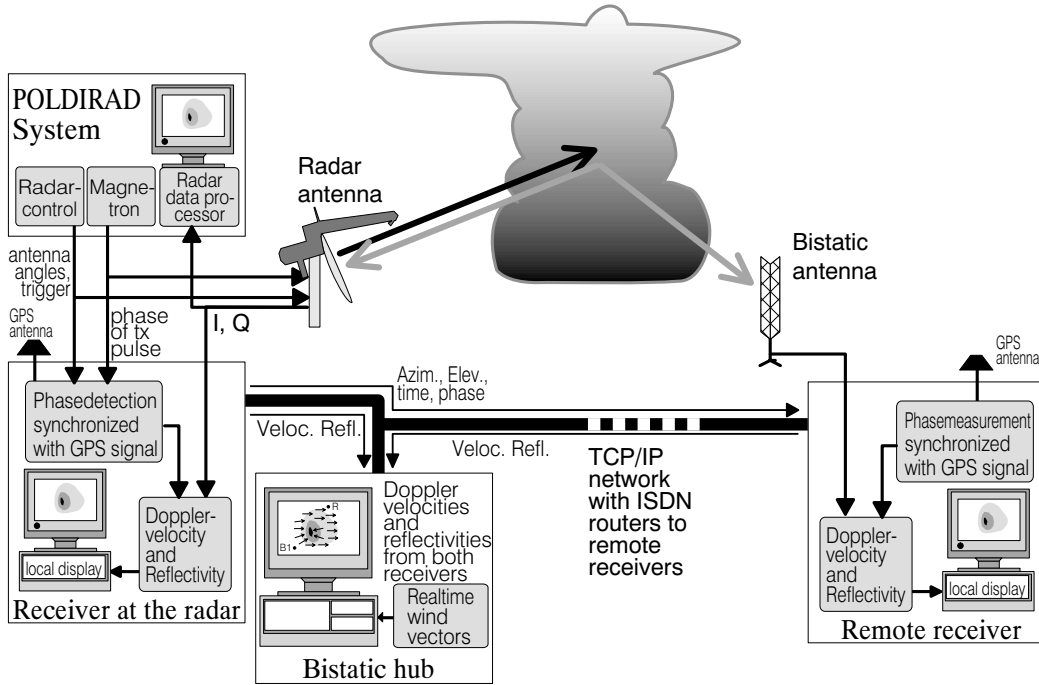


Figure 3.1: Block diagram of the bistatic multiple-Doppler radar network consisting of a transmitting source (POLDIRAD system) and remote bistatic receivers. For compatibility, a receiver independent of POLDIRAD is installed at the transmitting radar site. Real-time wind synthesis is performed by a central bistatic hub computer. The communication between each computer is achieved via a TCP/IP network based on ISDN (The illustration was kindly provided by Martin Hagen).

POLDIRAD is a C-band radar system operating at a frequency of 5.5 GHz ($\lambda = 5.45$ cm). The transmitter is a magnetron, and peak power at the antenna is 250 kW having a horizontal and vertical beam-width of 1° . For Doppler velocity measurements, the pulse length is typically chosen to be $1 \mu\text{s}$, i.e. 300 m, with a pulse-repetition frequency (PRF) of 1200 Hz. With this configuration, the Nyquist velocity, v_{nt} , is calculated as 16.35 m s^{-1} .

Since a magnetron is used as the transmitting source, the phase angle of each transmitted pulse is random and has to be measured. Frequency and timing/gating synchronization between the transmitter and receiver with sub-microsecond accuracy is achieved by using stable local oscillators at each site controlled by GPS signals.

Each bistatic remote receiver consists of an autonomous signal processor and a bistatic antenna (for more details, see Sec. 3.2). At the remote bistatic receivers, 126 range gates are sampled with a gate spacing of $\tau_s = 1.25 \mu\text{s}$ for each ray (cf. Sec. B). Data sampling at each passive bistatic receiver starts $5 \mu\text{s}$ (4 range gates) before the transmit pulse reaches the receiver directly via the baseline b (cf. Fig. 2.2). With 126 range gates separated by $1.25 \mu\text{s}$ and starting $5 \mu\text{s}$ before the pulse reaches the receiver, a maximum elliptical area with a main axis of $b + 45.75 \text{ km}$ can be covered. Communication between the remote receiver and the central bistatic hub computer is achieved via a TCP/IP network based on ISDN communication.

For compatibility between the monostatic radar and bistatic receivers, a receiver independent of the basic POLDIRAD system is installed at the radar site. This receiver detects the phase of the transmitted pulse, obtains azimuth and elevation angles from the POLDIRAD system, and measures reflectivity and Doppler velocity through the monostatic antenna. It transfers to the remote sites azimuth, elevation, phase angles, and time for the transmitted pulse via ISDN.

Doppler velocity, power, and Normalized Coherent Power (NCP)¹⁴ are computed from 64 samples at each bistatic remote receiver and subsequently sent to the central bistatic hub computer (cf. Sec. 3.3). Doppler velocities measured by each bistatic receiver as well as radial velocity measured by the receiver at the radar site are combined to give a horizontal wind-field at the central bistatic hub computer. Because Doppler velocity is collected simultaneously by each receiver, the wind-vector determination can be immediately computed and displayed online in spherical radar coordinates.

3.2 Bistatic antennas

A bistatic radar system with scanning parabolic antennas, as used for monostatic radar systems, would be too expensive to install and too difficult to handle. Therefore, inexpensive and easily constructed slotted waveguides can be used as bistatic antennas (for more details, see Wurman et al. (1993); Skolnik (1990)). Using a transmitting C-band Doppler radar system, the slotted waveguide has a length of 1.5 m surrounded by a triangular reflector having an edge length of 30 cm (Fig. 3.2).

Bistatic antennas are designed to receive only vertical polarization owing to low intensity-reduction for Rayleigh scattering at lower elevations (as investigated in Sec. 2.3.2). The receiving power pattern of all bistatic antennas was measured at an antenna range at the DLR. This was achieved by feeding a weak signal into the bistatic antenna, while an independent receiver measured the beam-pattern of the

¹⁴Index related inversely to the spectral width ranging from zero to one. For further explanation, see App. B.

slotted waveguide 180° horizontally as well as at different elevations. The three-dimensional power pattern, $G_b(\phi_b, \theta_b)$, in spherical coordinates, is necessary in order to convert the received power into reflectivity according Eq. (2.20) and Eq. (2.21).



Figure 3.2: Photograph of a bistatic antenna consisting of a slotted waveguide in the center surrounded by a triangular reflector (front panel removed).

During a weather situations with uniform reflectivity, de Elia (2000) measured the bistatic antenna pattern of the antennas operating within the bistatic Doppler radar network at the McGill University Montreal, Canada. He discovered that one antenna had a pattern with two maxima and assumed that this can be caused by waveguide shift while handling. Irregularities in the antenna pattern of the bistatic antennas operating in the bistatic Doppler radar network at the DLR were not found as illustrated in Fig. 3.3.

The power pattern of all bistatic antennas used in the bistatic Doppler radar network at the DLR were designed to receive the main power with a horizontal angular aperture covering -30° to 30° with a maximum in the principal axis. A horizontal cross-section of the receiving power pattern of a bistatic antenna at 2.5° , 12° , and 20° elevation is shown in Fig. 3.3(a).

The antenna aperture is inversely proportional to the antenna gain. Wide-beam antennas with low antenna gain require high reflectivity values which can be observed during thunderstorms. Therefore a compromise has to be found between the aperture angle and the applications, e.g., thunderstorm probing or investigations within the boundary layer.

To measure wind-fields during thunderstorms (high reflectivities), only antennas that receive the main power between $1^\circ - 23^\circ$ vertically and 60° horizontally are used. A vertical cross-section of the antenna power pattern is exhibited in Fig. 3.3(b). The influence of the antenna's front panel (cf. Fig. 3.4(b) and Fig. 3.2) on the power pattern was also investigated. The impact of the front panel on the antenna pattern is negligible.

To measure wind-fields within the surface layer or to receive weak echoes, antennas receiving the main power between $1^\circ - 9^\circ$ vertically and 60° horizontally were installed. A vertical cross-section of the power pattern of a receiving antenna is shown in Fig. 3.3(c). With the sharp power gradient between 0° and 1° , ground-clutter contamination should be suppressed. This vertical antenna aperture assures measurements up to a maximum height of about 4.7 km – 6.2 km (for $30 \text{ km} \leq r'_t \leq 40 \text{ km}$).

The experimental setup is illustrated in Fig. 1 with POLDIRAD and three bistatic receiver systems located at Lichtenau, Lagerlechfeld, and Ried. A photograph of the antennas installed at the three location is given Fig. 3.4. Each bistatic antenna covers an area of 60° horizontally (as indicated by the hatched area in Fig. 1) and differs

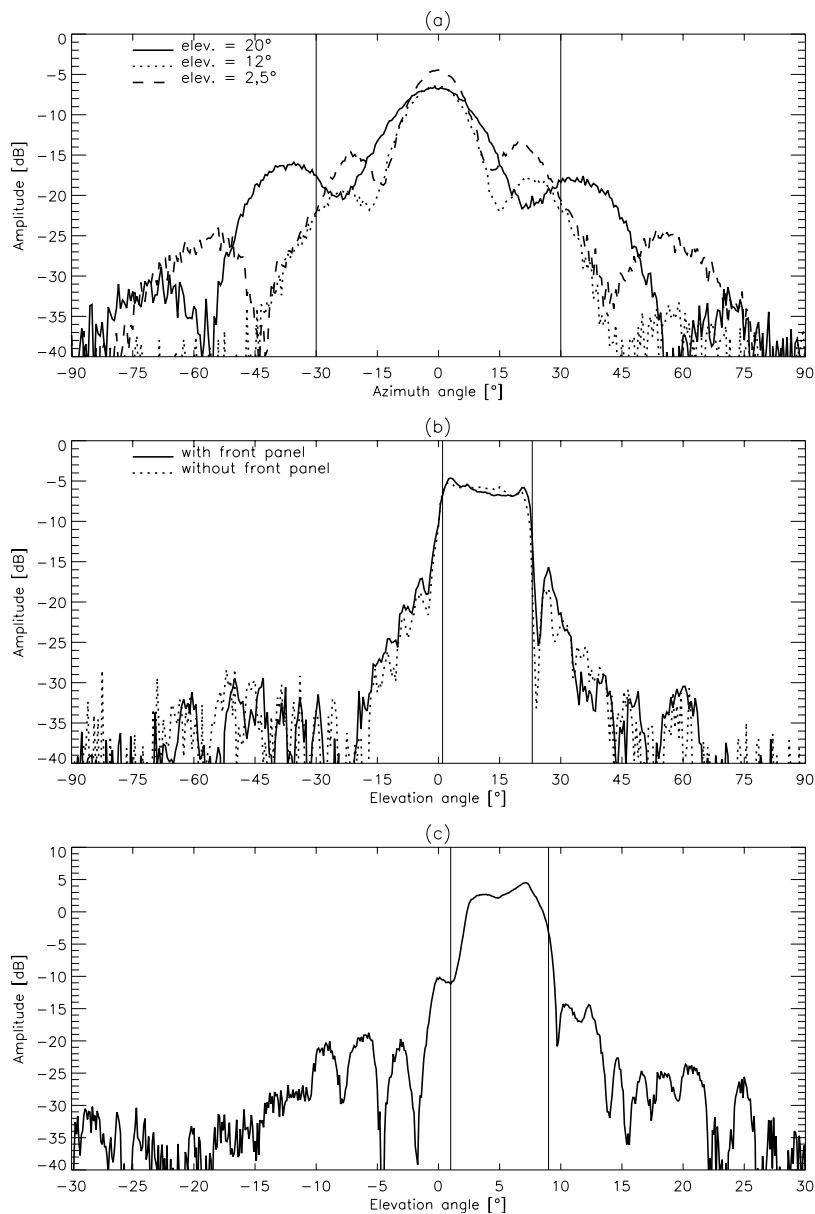


Figure 3.3: One-way receiving power-pattern in dB of vertically polarized bistatic antennas measured in azimuthal direction and for different elevations at an DLR antenna range. (a) The receive power-pattern sampled in azimuthal direction ($-90^\circ \leq \phi_b \leq 90^\circ$) for 2.5° , 12° , and 20° elevation. The angular aperture covering $-30^\circ \leq \phi_b \leq 30^\circ$ is signified by the vertical lines. (b) The receive power-pattern is measured in a vertical direction ($-90^\circ \leq \theta_b \leq 90^\circ$) for an azimuth angle of 0° , with and without the front panel. The vertical angular aperture covering $1^\circ \leq \theta_b \leq 23^\circ$ is symbolized by the vertical lines. (c) As (b), but for an antenna with a vertical antenna aperture of about 8° .

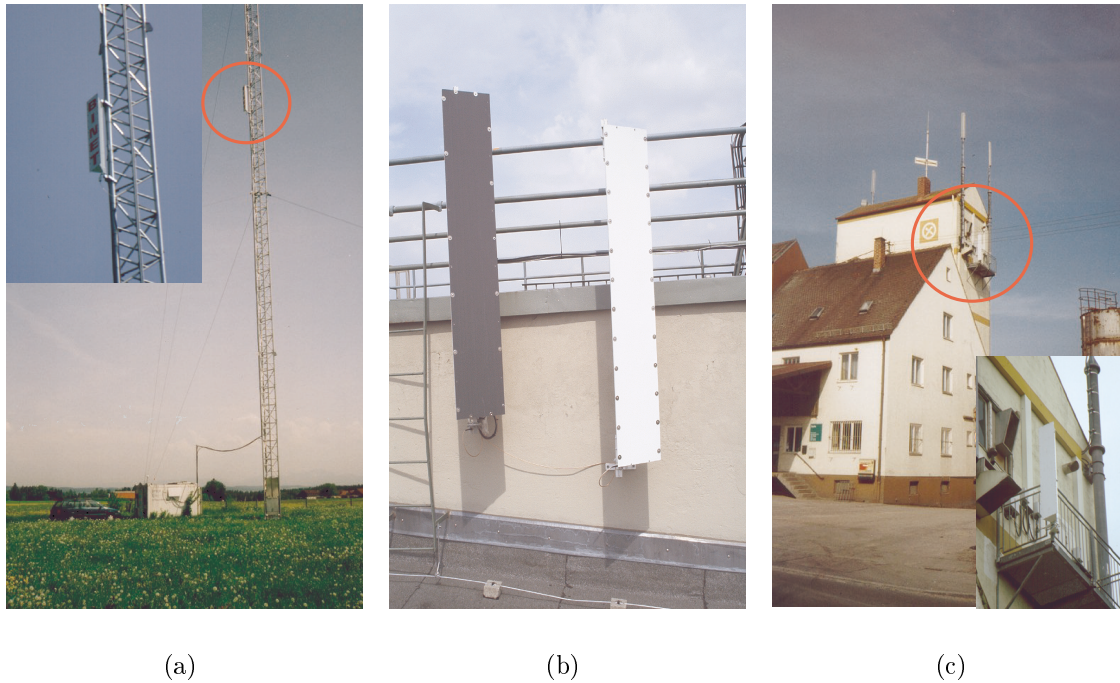


Figure 3.4: An illustration of the bistatic antennas at the three remote sites (a) Lichtenau, (b) Lagerlechfeld (22° -antenna left, 8° -antenna right), and (c) Ried. A GPS antenna for exact timing is seen at the rear at Lagerlechfeld.

only in the vertical antenna aperture. The bistatic receiver systems at Lichtenau and Lagerlechfeld are each equipped with two antennas receiving the main power between $1^\circ - 9^\circ$ and $1^\circ - 23^\circ$ vertically. Depending on the weather condition, the vertical antenna aperture can be selected via a remote switch. At Lichtenau the antenna with a vertical aperture of 8° is north-facing, while the antenna with a vertical aperture of 22° faces eastwards. At Lagerlechfeld the two antennas are both south-facing. The receiver at Ried is equipped with a south-facing antenna with a vertical antenna aperture of 8° .

3.3 Real-time wind synthesis at the central hub computer

To achieve a wind synthesis in real-time, it is important to merge the Doppler velocities to a horizontal wind-field rapidly. The wind synthesis is achieved immediately after the signal is received. At that time the volume-scan is not finished, so that interpolation onto a Cartesian grid, to a reference time, and the quality-control scheme cannot be applied. To assure the quality of the horizontal wind-field, Doppler velocities with NCP value larger than 0.3 (chosen empirically) are used for the wind-field determination. The real-time display being established immediately after the signal was received is very important to give warnings of severe weather events. To apply wind-fields for nowcasting of weather events or for assimilation into numerical

weather prediction models, the Doppler velocities are processed more substantially afterwards (this topic is enlarged upon Sec. 4).

At the remote receiver, data is sampled in an elliptical coordinate system and interpolated onto a spherical one. The horizontal wind–vector determination at the bistatic hub is obtained in the spherical monostatic radar coordinate system (r'_t, ϕ_t, θ_t) without any interpolation of the whole scan to a reference time.

The wind–vector at the central hub computer is always determined with the radial velocity, v_t , and Doppler velocity measured by a bistatic receiver, v_e , as demonstrated in Sec. 2.6 [Eq. (2.34) and Eq. (2.35)]. The horizontal wind–field determination with dual–Doppler processing is exhibited in Fig. 3.5. A PPI¹⁵ at 1° elevation is shown taken during a stratiform precipitation event on 19 June 2001 at 0731 UTC. The radial velocity [color–coded in Fig. 3.5(a)] and the respective Doppler velocity measured by the bistatic receivers Lagerlechfeld, Lichtenau, and Ried [color–coded in Figs. 3.5(b) – (d)] are combined to a horizontal wind–vector field (indicated by arrows in Figs. 3.5(b) – (d) and superimposed on the respective Doppler velocity field).

Each horizontal wind–vector field determined by the dual–Doppler analysis has to be merged into one average wind–field. Therefore, each velocity component u_i , and v_i , determined by the i 'th bistatic dual–Doppler radar system consisting of POLDIRAD and one bistatic receiver, is averaged over the number of bistatic dual–Doppler radar systems, n , covering the same area. In the bistatic multiple–Doppler radar network at Oberpfaffenhofen (Fig. 1), there are areas which are covered by one ($n = 1$), two ($n = 2$), and three ($n = 3$) dual–Doppler radar systems. In the case of $n \geq 2$, the wind–components are weighted according to the respective scattering angle of the i 'th bistatic dual–Doppler radar system. $W_\gamma^{(i)}$ is the weight of the velocity component determined by the i 'th bistatic dual–Doppler radar. The averaged velocity components \bar{u} and \bar{v} can be calculated as

$$\bar{u} = \frac{1}{n} \sum_{i=1}^n W_\gamma^{(i)} u_i \quad , \text{ and} \quad (3.1)$$

$$\bar{v} = \frac{1}{n} \sum_{i=1}^n W_\gamma^{(i)} v_i \quad , \quad (3.2)$$

with

$$W_\gamma^{(i)} = \frac{180^\circ - \gamma_i}{180^\circ}. \quad (3.3)$$

For the stratiform precipitation event on 19 June 2001, the three horizontal wind–vector fields [Figs. 3.5(b) – 3.5(d)] are merged according to Eq. (3.1) and Eq. (3.3) to one average horizontal wind–vector field [Fig. 3.5(a)].

¹⁵ PPI (*plan–position–indicator*) is an intensity–modulated display on which echo signals are shown in plan position with range and azimuth angle displayed in polar coordinates [cited from the glossary by Rinehart (1999)].

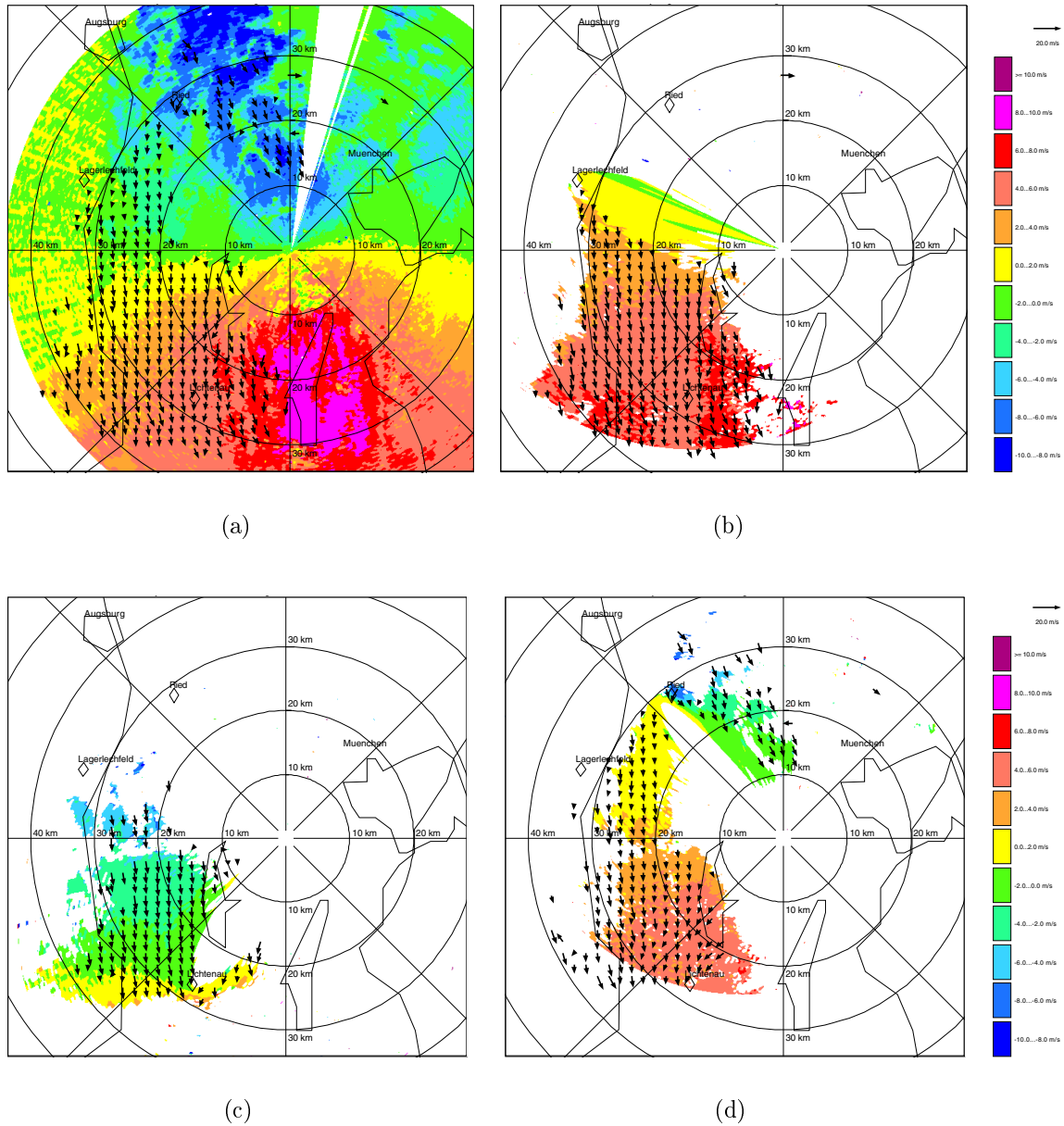


Figure 3.5: PPI of the Doppler velocity superimposed on the horizontal wind–vector field at 1° elevation for a stratiform precipitation event on 19 June 2001 at 0731 UTC. The radial velocity (a) of POLDIRAD and the Doppler velocities of (b) Lagerlechfeld, (c) Lichtenau, and (d) Ried are color–coded. Negative values indicate a movement towards the receiver and positive away from the receiver. Horizontal wind–vector fields determined by v_t and v_e of (b) Lagerlechfeld, (c) Lichtenau, and (d) Ried are superimposed on the respective Doppler velocity field. These three vector–wind fields are averaged into one wind–vector field indicated by arrows in (a).

4 Wind synthesis and quality control

For further usage of radar data, e.g. for nowcasting of weather events or for assimilation into numerical weather prediction models, the measured data is processed more extensively to ensure higher data-quality. To achieve a substantial quality-control the information on the whole volume-scan or additionally the successive volume-scans must be available.

In this section, data-processing algorithms are described in the same sequence as they are applied to the measured data: Section 4.1 describes, how aliasing errors are removed from the Doppler velocity fields in order, first, to interpolate the sampled data of the entire volume-scan onto a Cartesian coordinate system and, second, to interpolate two successive volume-scans to a reference time. Section 4.2 shows, how noisy Doppler velocity data is removed. Furthermore, a weighting factor is defined before the horizontal wind-vector field can be determined. The weighting factor is related to the accuracy of the Doppler velocity measurement and its spatial resolution.

As described in Sec. 4.3, the quality of each horizontal wind-vector is analyzed by means of normalized coherent power (NCP), Doppler velocity, and power. A quality field is determined, which is available together with the measured wind-vector field to the user. Depending on the application of the wind-vector field, each data point can then be chosen or weighted for further processing according to the quality-index field. Furthermore, the entire wind-vector field undergoes a persistence check in time and space and an internal check for data consistency. A suggested method to check the probability of contamination due to the transmitted sidelobes is also presented (Sec. 4.4).

Horizontal wind-vector fields are determined in three different ways depending on the application:

- (1) After the data is sampled and processed at the bistatic receiver, it is then transferred to the central bistatic hub computer. There, the horizontal wind-vector field is determined and shown immediately on the real-time display (cf. Sec. 3.3). Because the volume scan is not yet finished at that time, dealiasing of Doppler velocities and interpolation in time and space cannot be applied. Noisy data is removed and, for the horizontal wind-vector field determination, each measured Doppler velocity is weighted according to its scattering angle (cf. Sec. 3.3, Sec. 4.2). With the horizontal wind-vector field displayed in real-time, areas of severe weather can be identified and warnings can be given immediately for these areas.
- (2) After the volume-scan is finished, data is processed in the same temporal sequence as described in this section to determine a horizontal wind-field from measured Doppler velocities and the quality-index field of the horizontal wind-field. After the quality of the measurements is analyzed by means of the quality-control scheme, quality-controlled horizontal wind-vector fields together with a quality-index field are available for further applications.

- (3) To understand atmospheric phenomena, a knowledge of the three wind-vector components is of significant value. Vertical velocity can be retrieved with a constraining model as explained in more detail in Sec. 5. All algorithms discussed in this section can be applied to determine the wind-vector field. Modifications have to be applied, as discussed in Sec. 4.2. Here, noisy data is removed. The weights are not applied to determine u, v , but to the minimization procedure [Eq. (5.3)].

4.1 Data-processing

4.1.1 Dealiasing of Doppler velocity

There is a limit to the extent to which velocity can be measured unambiguously by a radar system. The phase of the electro-magnetic wave is measured only when the wave is transmitted or received. The Doppler velocity can be derived from the difference in phase shift between two successive pulses. The phase shift at a monostatic radar is expressed as

$$\Delta\phi_t = \frac{4\pi T_s v_t}{\lambda} \quad , \quad (4.1)$$

where λ is the radar wavelength, T_s is the sample time ($T_s = 1/PRF$), and v_t is the radial component of the target's velocity. The phase shift at a bistatic receiver is given as

$$\Delta\phi_b = \frac{8\pi T_s v_e \cos(\gamma/2)}{\lambda} \quad , \quad (4.2)$$

where v_e is the component of the target's velocity perpendicular to the ellipsoid and γ is the scattering angle. The velocity can only be determined unambiguously if the difference in the phase shift caused by a moving particle lies between $-\pi \leq \Delta\phi \leq \pi$. Otherwise it is not clear if the true phase difference is the measured difference plus a multiple of $\pm 2\pi$. Aliasing occurs when the sample frequency $1/T_s$ of the transmitting radar is too high to resolve the phase shift $\Delta\phi$ that occurs between successive pulses reflected by moving particles (cf. Fig. 4.1). Sampling at a rate of, i.e. 1200 Hz will preserve all frequencies up to 600 Hz ($f_N = PRF/2 = 600$ Hz) in the sampled function. The maximum frequency that will produce no aliasing is called Nyquist frequency and is given by

$$f_N = \frac{2v_N}{\lambda} \quad . \quad (4.3)$$

The maximum target velocity guaranteed to produce no aliasing is called the Nyquist velocity and is given for both monostatic and bistatic radar in Tab. 2.1,

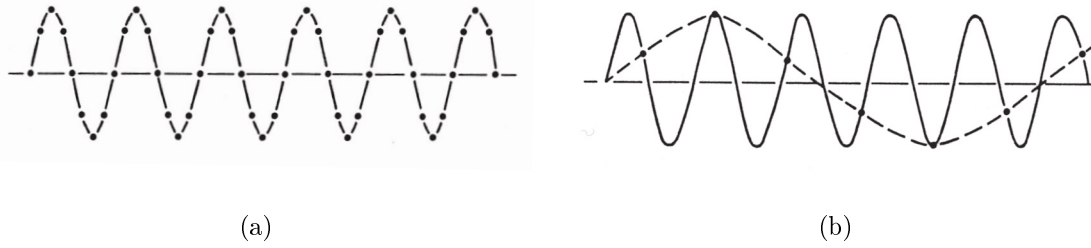


Figure 4.1: Schematic view of (a) sine wave with a frequency lower than the Nyquist frequency and (b) sine wave with a frequency higher than the Nyquist frequency, showing the fictitious frequency.

Sec. 2. When the Doppler velocity measured by a monostatic or bistatic receiver, v_t and v_e , falls outside the respective Nyquist interval $[-v_{nt}, v_{nt}]$, $[-v_{ne}, v_{ne}]$, the velocity is aliased into that interval. The non-aliased Doppler velocity, for a monostatic receiver, \hat{v}_t , and for a bistatic receiver, \hat{v}_e , can be expressed, respectively, as

$$\hat{v}_t = v_t + 2i v_{nt}, \quad i \in \mathbf{Z}, \quad \text{and} \quad (4.4)$$

$$\hat{v}_e = v_e + 2i v_{ne}, \quad (4.5)$$

where i is the aliasing interval (positive or negative). The differences between the monostatic and bistatic Nyquist intervals are discussed in Sec. 2.2 and have to be adapted to Eqs. (4.4) and (4.5), respectively.

A number of dealiasing algorithms have already been developed to recover \hat{v}_t from v_t for a monostatic radar system, e.g. Yamada & Chong (1999); James et al. (2000); James & Houze (2001). In operational meteorology and field research, dealiasing must be achieved automatically because of the vast quantity of radar data received at a given time interval. The efficiency of a dealiasing algorithm depends on both the characteristics of the radar, and the amount and distribution of observational data within the PPI.

To unfold Doppler velocities measured by a bistatic system, the Nyquist velocity interval has to be calculated for each data point due to the variable γ (cf. Tab. 2.1). Alternatively, v_a , which has a constant Nyquist interval, can be unfolded and then transformed into v_e (cf. Eq. 2.1). The apparent velocity, v_a can then be unfolded with the existing algorithms for monostatic radar data, e.g. the 4D dealiasing algorithm developed by James & Houze (2001).

A very efficient dealiasing algorithm was developed in order to dealias Doppler velocities within an uniform wind-field. It dealias Doppler velocities by comparing each measured wind component with a wind component from a reference field and adjusting i so that the difference between \hat{v}_t (\hat{v}_e) and the reference wind-field is less than v_{nt} (v_{ne}). The horizontal reference wind-vector field is determined using

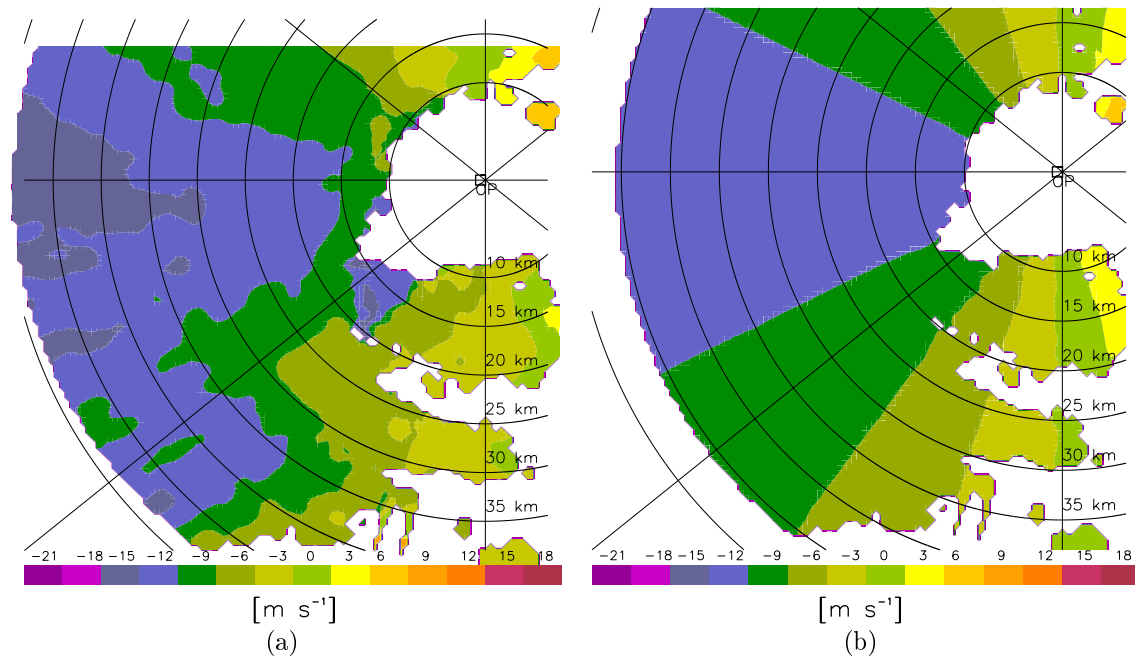


Figure 4.2: A horizontal cross-section at 750 m above MSL of (a) the radial velocity field in m s^{-1} measured by POLDIRAD for a stratiform precipitation event on 10 April 2001, 1317 UTC and (b) the radial velocity reference field in m s^{-1} (positive values indicate a direction away from the receiver, negative towards the receiver). Oberpfaffenhofen is located at the center.

the wind-information from a sounding or a vertical profile of the horizontal wind using the VAD analysis (Lhermitte & Atlas, 1961; Browning & Wexler, 1968). This horizontal reference wind-field is then projected onto the respective velocity component of each individual receiver system. As an example, both the measured and the reference radial velocity-field are shown in Fig. 4.2 during a stratiform precipitation event¹⁶ on 10 April 2001. If the resulting velocity difference between the reference and measured wind components is smaller than $0.5v_{nt}$ and $0.5v_{ne}$ (Hagen & Stockinger, 1991), respectively, then the velocity is assumed to be not folded. Alternatively, the Doppler velocity is recalculated from Eq. (4.4) and Eq. (4.5), adjusting i until the resulting velocity difference is smaller than $0.5v_{nt}$ and $0.5v_{ne}$, respectively. On 10 April 2001 at 2.8 km above MSL the measured radial velocity was folded, as illustrated in Fig. 4.3(a). The folded area occurs west of OP with rapid changes in the velocity values (skip in color). On this wind-field, the dealiasing algorithm is applied. The aliasing interval is $i = \pm 1$. The resulting unfolded velocity field is shown in Fig. 4.3(b).

¹⁶The event is discussed in more detail in Sec. 6.2.1.

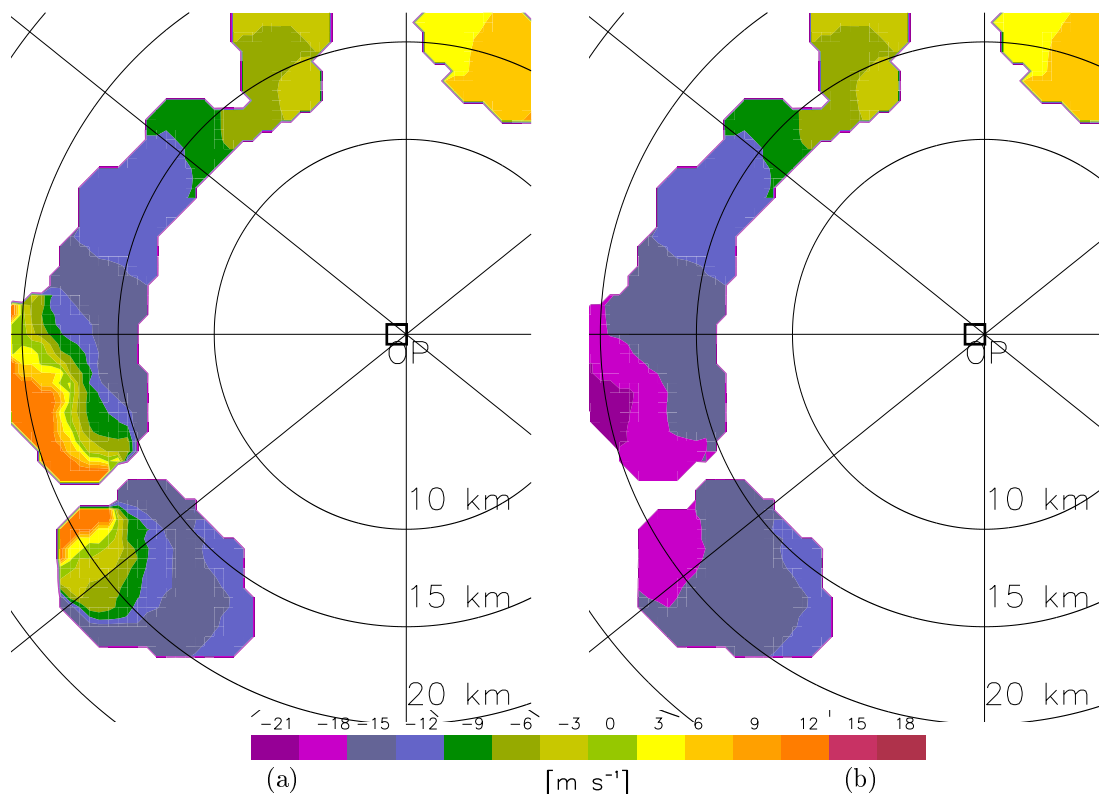


Figure 4.3: Horizontal cross-section at 2.8 km above MSL (a) before and (b) after dealiasing of the radial velocity in m s^{-1} measured by POLDIRAD on 10 April 2001, 1317 UTC during a stratiform precipitation event. Positive values indicate a direction away from the receiver, negative towards the receiver. Aliasing of the wind-field can be seen in the rapid change of wind-velocity west of OP (decrease of negative values and increase in velocity values).

4.1.2 Interpolation onto a Cartesian grid and to a reference time

Monostatic radar systems sample data on a spherical coordinate system [cf. Fig. 4.4(a)], while the data measured by bistatic receivers is sampled on an elliptical coordinate system [cf. Fig. 4.4(b)]. The size and shape of the sample volume vary according to r'_t for a monostatic radar or $r'_t + r'_b$ and γ for a bistatic radar system (cf. Sec. 2.1).

Therefore, for further data-processing, the measured data must be interpolated onto a common Cartesian coordinate system with a uniform grid-spacing. This can be achieved using a linear interpolation method based on the use of a sphere of influence (Protat & Zawadzki, 1999). Here, at each Cartesian grid-point, a sphere of influence is defined in which all measured data points are weighted by their distance to the Cartesian grid-point and averaged to a single value which represents this grid-point. The sphere of influence has a minimum diameter of $\sqrt{2}\Delta x$, with Δx being the horizontal grid-interval (usually $\Delta x = 500$ m). The diameter of the sphere is

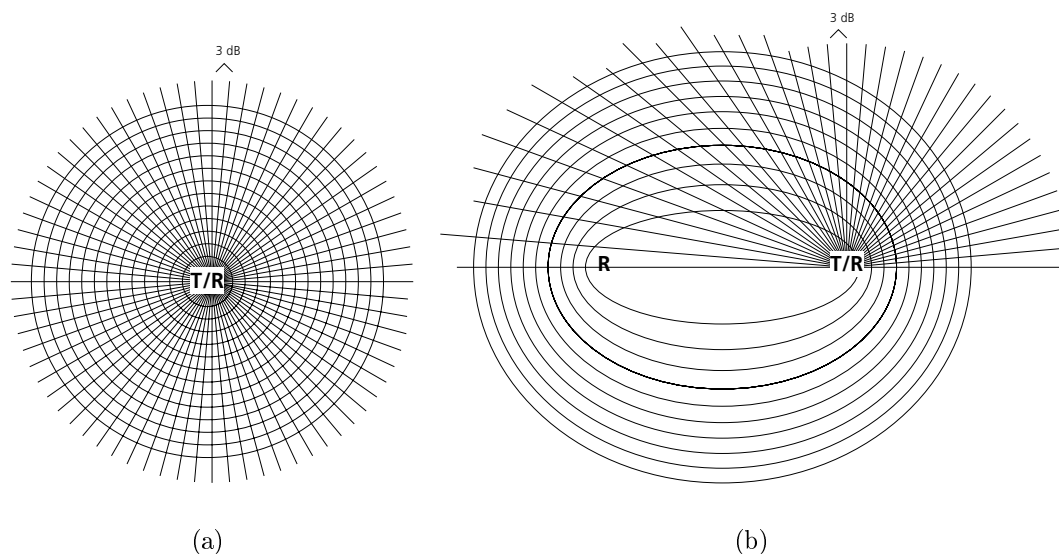


Figure 4.4: Horizontal cross–section of the coordinate system on which the data is sampled by (a) a monostatic and by (b) a bistatic radar system. The two–dimensional cross–section is obtained along the scattering plane. The 3dB beam–width and the surfaces of constant delay are indicated.

adaptively increased to ensure that at least two points are contained within a sphere of influence. The maximum diameter is always less than 3 km.

The local evolution of a weather situation during the time the volume–scan is made (e.g. for 360°–scans, POLDIRAD needs about five minutes for eight elevations) can be very important especially for rapidly moving weather systems. It can also have a great impact on the retrieval quality of the three wind components, u, v, w (Sec. 5). For considering the local evolution, the measurements of two volume–scans are interpolated to a single reference time (Protat & Zawadzki, 1999). A linear temporal evolution of the components measured is assumed. For an effective temporal interpolation, a moving frame of reference is applied [for more detail, see Protat & Zawadzki (1999)].

4.2 Synthesis of the horizontal wind–vector field

First, noisy Doppler velocity data is removed. Then, the horizontal wind is estimated according to Eqs. (2.34) and (2.35), while each Doppler velocity measurement is weighted according to the scattering angle. Both are applied to the measured Doppler velocity on a Cartesian grid as well as on the elliptical/spherical grid, i.e. for the real–time display generated at the central bistatic hub computer.

The signal quality–index (SQI) is used typically in the signal–processing as a

threshold for Doppler velocity measurements. It helps to eliminate signals which are either too weak (high SNR¹⁷) to be useful or which have NCP (normalized coherent power, see Appendix B) values too small to justify further analysis.

The SQI is applied via the relation between NCP and reflectivity factor within the resolution volume. NCP is a measure of the combined effects of wind shear and turbulence, and reflectivity is indirectly a measure of the signal-to-noise ratio.

The idea of the SQI is to consider data with large velocity dispersion (e.g. $NCP \geq 0.3$, empirically chosen) only if the reflectivity factor exceeds a certain threshold, e.g. during thunderstorms, and to reject data with large velocity dispersion and low reflectivity factors as illustrated in Fig. 4.5. Each data point is considered only when its reflectivity factor is larger than the reflectivity factor horizontally averaged over the respective level minus 5 dBZ (empirically chosen). If the reflectivity factor is less than 5 dBZ below the horizontal average, the NCP must exceed a value of 0.3 to be considered for further data-processing. Both thresholds are chosen empirically. For an application on the spherical or elliptical coordinate system (e.g. at the real-time display), only Doppler velocities are used for the horizontal wind-field determination when their NCP value exceeds 0.3.

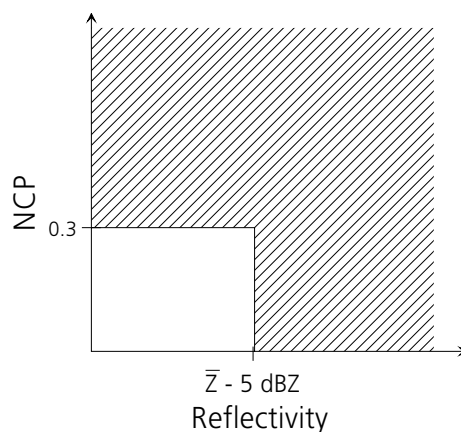


Figure 4.5: Schematic view of the decision criterion combining the reflectivity factor and NCP value. Each data point is considered for further processing (hatched area) when either $NCP \geq 0.3$ or $Z \geq \bar{Z} - 5$ dBZ, or both criteria, are fulfilled.

As an example of the application of the SQI criterion to measured data, Fig. 4.6 presents a horizontal cross-section at 1.6 km above MSL of the horizontal wind-vector field superimposed on the bistatic reflectivity factor, Z_b , measured by the bistatic receiver Lagerlechfeld. In Figure 4.6(a) the SQI criterion is not applied, while in Fig. 4.6(b) noisy data is removed using the SQI criterion. The horizontal wind-vector field is determined by using the Doppler velocities measured by receivers at Oberpfaffenhofen and Lagerlechfeld.

¹⁷ *Signal to noise ratio – a ratio that measures the comprehensibility of data, usually expressed as the signal power divided by the noise power [cited from the glossary by (Rinehart, 1999)].*

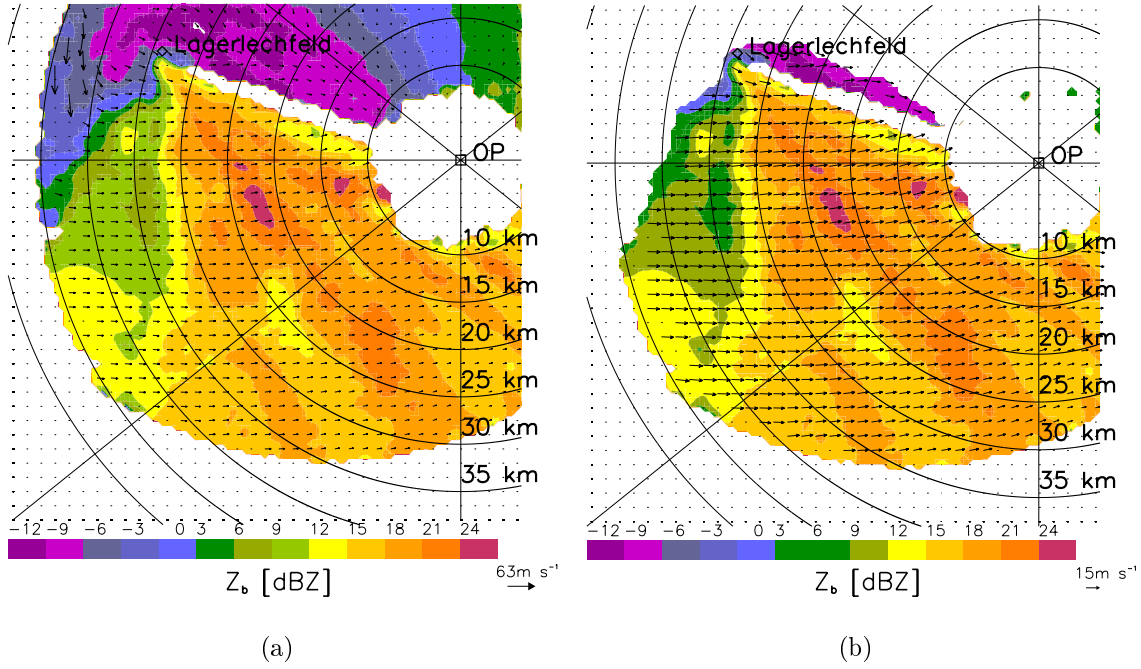


Figure 4.6: Horizontal cross–section at 1.6 km above MSL of the horizontal wind in m s^{-1} (arrows) underlaid by the bistatic reflectivity factor field, Z_b , in dBZ measured by the receiver Lagerlechfeld on 2 February 2000 at 1708 UTC (a) without applying the SQI criterion and (b) with the SQI criterion applied on the measured data. The horizontal wind–vector is determined by using the Doppler velocity sampled by receivers at Lagerlechfeld and OP. For clarity of display, only every third wind–vector is plotted.

As shown in Fig. 2.14, within a bistatic system the spatial resolution and the accuracy of the Doppler velocity measurement depend on the scattering angle, γ . Both, the length of the resolution volume and σ_{v_e} increase with increasing γ as $a_b \approx \cos^{-2}(\gamma/2)$, $\sigma_{v_e} \approx \cos^{-2}(\gamma/2)$. In a bistatic dual–Doppler radar system, high accuracy of the Doppler measurement within small sample volumes is achieved with small γ in the quasi–monostatic area, while low accuracy within large sample volumes occurs close to the baseline b (cf. Fig. 2.14). The dependency of spatial resolution and accuracy of the Doppler measurements is given by the weighting factor W_γ and can be calculated from the formula:

$$W_\gamma = \frac{180^\circ - \gamma}{180^\circ} . \quad (4.6)$$

As an example, the distribution of the weighting factor at ground level is exhibited in Fig. 4.7 within the bistatic dual–Doppler radar system consisting of POLDIRAD and the receiver at Lagerlechfeld (based on the distribution of γ in Fig. 2.3).

Note that both the SQI and the weighting factor can be applied immediately to

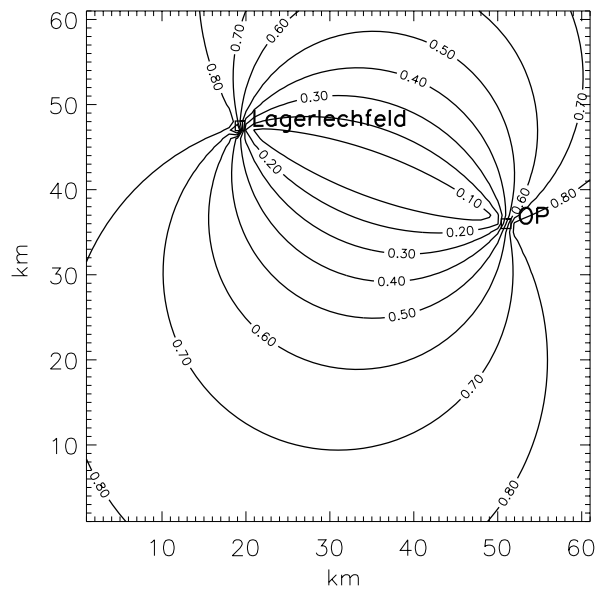


Figure 4.7: Horizontal cross-section at ground level of the W_γ -distribution for the bistatic Doppler radar consisting of Lagerlechfeld and OP.

the measurements independent of the coordinate system (e.g. wind synthesis at the bistatic hub computer see Sec. 3.3). In summary, using the Doppler velocity that passed the SQI criterion, the horizontal wind-field can be determined either with the dual-Doppler processing always using v_t and v_e [cf. Eqs. (2.2) and (2.3)] or, in the case of an overdetermined equation system [Eq. (2.30), in a least square sense [cf. Eqs. (2.34) and (2.35)].

At the central hub computer, the horizontal wind-vector field is determined in the dual-Doppler sense for real-time display. In the case where more than two Doppler velocities are measured at a certain point, the wind components are weighted and averaged according to Eqs. (3.1) and (3.3). Because radial velocity is used for each dual-Doppler-processed horizontal wind, v_t has a much higher weight/priority in the dual-Doppler processing compared to multiple-Doppler processing if there are more than two receivers available.

In the post-processing discussed here, the horizontal wind-vector field is determined in a least square sense. The weights are applied to the equation system. Here, the variables b_1 and b_2 have to be modified to solve Eqs. (2.34) and (2.35) as

$$b_1 = \sum_{i=1}^n W_\gamma^{(i)} v_{m_i} \frac{\sin(\phi_{b_i}) \cos(\theta_{b_i}) + \sin(\phi_t) \cos(\theta_t)}{2 \cos(\gamma_i/2)} \quad (4.7)$$

$$b_2 = \sum_{i=1}^n W_\gamma^{(i)} v_{m_i} \frac{\cos(\phi_{b_i}) \cos(\theta_{b_i}) + \cos(\phi_t) \cos(\theta_t)}{2 \cos(\gamma_i/2)} \quad (4.8)$$

If the bistatic radar system consists of only one bistatic receiver, $W_\gamma = 1$ for all scattering angles. For small numbers of bistatic receivers, the difference between the two methods is negligible.

4.3 Quality-control scheme for horizontal wind-vector fields

Creating a quality-control scheme is a very difficult task. If the scheme is too strict, too much data, even higher quality data, will be rejected. If the scheme is not strict enough, errors can pass. The choice for a tight or a loose quality-control scheme will depend on the weather conditions and the number of measurements required.

Most schemes are based on the setting of thresholds which are chosen mostly empirically. Fixed thresholds give problems when applied to different weather situations and for different scientific purposes. The balance between the quality and the number of measurements must be found according to the scientific question to be investigated.

Furthermore, quality-control schemes will usually succeed when set to accomplish a specific purpose but will fail when applied to other purposes. This being the case, it is impossible to devise an all-purpose quality-control scheme that satisfies the demands of all scientists.

The quality-control scheme defined in this section is divided into four algorithms. First, the signal quality of each range gate is controlled based on power and NCP measurements (Sec. 4.2). Second, influences of fixed parameters, e.g. accuracy of the Doppler velocity measurement or the geometrically induced accuracy of the Doppler velocity measurement are analyzed (Sec. 4.3.1). Third, the influence of weather conditions on the Doppler velocity measurement itself, and therefore, the probability of external contamination are taken into account. For instance, contamination due to sidelobes only becomes critical during weather events having sharp gradients of the reflectivity factor (Sec. 4.3.2, Sec. 4.3.3). Fourth, the measured wind-field can be compared to a 'wind-field model' reproducing the respective weather situation (Sec. 4.4). For instance, wind-shear during a frontal passage or a thunderstorm gives a strong structure in the horizontal wind-field, which can then be tracked in time and space. All structures, including high wind-shear, that cannot be tracked in time and space are then rejected, because only data containing clear meteorological signals should pass the quality-control scheme. The algorithms presented in this section are only a first attempt at a quality-control scheme. They can be supplemented or expanded. The quality-control scheme can be applied immediately after the volume-scan has been completed. Note that always both raw data and data that has passed the quality-control scheme are stored.

In this quality-control scheme, certain algorithms are applied so as to reject or pass data, i.e. SQI criterion, check on temporal and spatial persistence. Others are applied in the fuzzy logic sense with the quality weighted with values ranging from zero to one. The results of each weighting algorithm can be merged to achieve an average quality-control field. All thresholds are set empirically.

In the following sections, three quality-index fields are defined according to: (1)

the accuracy of the horizontal wind–field depending on the configuration of transmitter, target, and receiver, denoted as $F(\sigma'_{|\mathbf{v}_h|})$; (2) the probability of sidelobe contamination, denoted as $F(\nabla Z)$; and (3) the fractional uncertainty of the wind–field measurement, denoted as $F(\sigma'_{|\mathbf{v}_h|}/|\mathbf{V}_h|)$. Note that the standard deviation of the horizontal wind–field, depending on the configuration of transmitter, target, and receiver, is fixed for a chosen experimental setup. By the same token, those quality–index fields, defined by the measured parameters of NCP, power, and Doppler velocity, have to be calculated for each volume–scan.

The influence of each quality–index field on the average quality–index field can be chosen according to the application of those quality–controlled wind–vectors and the weather situation with the respective weights $W_{F(\sigma'_{|\mathbf{v}_h|})}$, $W_{F(\nabla Z)}$, and $W_{F(\sigma'_{|\mathbf{v}_h|}/|\mathbf{V}_h|)}$. The quality fields can then be averaged to a single quality field using

$$\bar{F} = \frac{1}{C} \left(W_{F(\sigma'_{|\mathbf{v}_h|})} F(\sigma'_{|\mathbf{v}_h|}) + W_{F(\nabla Z)} F(\nabla Z) + W_{F(\sigma'_{|\mathbf{v}_h|}/|\mathbf{V}_h|)} F(\sigma'_{|\mathbf{v}_h|}/|\mathbf{V}_h|) \right), \quad (4.9)$$

where

$$C = W_{F(\sigma'_{|\mathbf{v}_h|})} + W_{F(\nabla Z)} + W_{F(\sigma'_{|\mathbf{v}_h|}/|\mathbf{V}_h|)}.$$

Each quality–index field and the average index field range between zero and one. Quality–index fields versus the respective parameter are illustrated in Fig. 4.8 and will be discussed in more detail in the following sections.

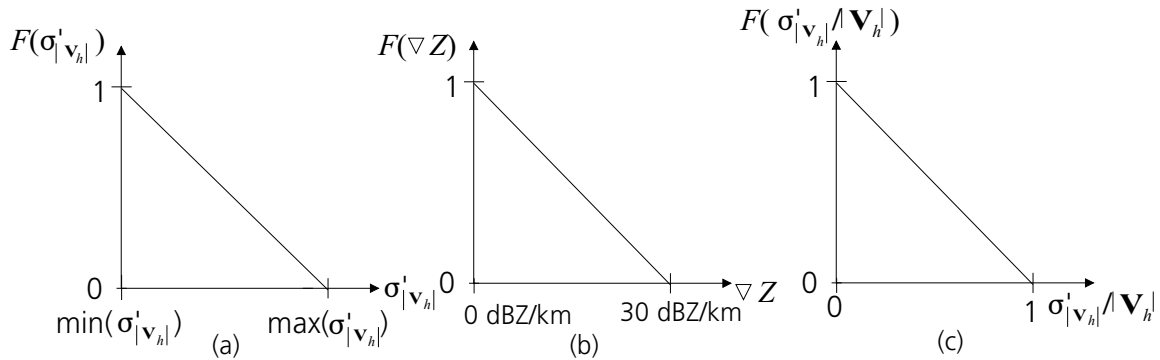


Figure 4.8: Quality–index field versus (a) $\sigma'_{|\mathbf{v}_h|}$, (b) ∇Z measured by the monostatic receiver, and (c) $\sigma'_{|\mathbf{v}_h|}/|\mathbf{V}_h|$.

4.3.1 Utilizing geometrical accuracy

The horizontal wind–field is determined by the velocity components v_t and v_e , measured by the monostatic and bistatic receiver, respectively. The standard deviation

of the horizontal wind-field can be expressed by the quality-index field $F(\sigma'_{|\mathbf{v}_h|})$. It depends only on the geometrical location of transmitter, receiver, and target (cf. Sec. 2.7),

For a dual-Doppler radar system, the highest accuracy in the horizontal wind-field determination is expressed by $F(\sigma'_{|\mathbf{v}_h|}) = 1$ at $\min(\sigma'_{|\mathbf{v}_h|})$ and lowest accuracy by $F(\sigma'_{|\mathbf{v}_h|}) = 0$. Due to the large values of $\sigma'_{|\mathbf{v}_h|}$ close to the baseline, the upper limit of $\sigma'_{|\mathbf{v}_h|}$ ($\max(\sigma'_{|\mathbf{v}_h|})$) has to be chosen empirically. For a bistatic dual-Doppler radar system, the standard deviation reaches its minimum at a scattering angle of about 100° with $\min(\sigma'_{|\mathbf{v}_h|}) = 2.42$, and $\max(\sigma'_{|\mathbf{v}_h|})$ set empirically to 5.0 [covering an area with a scattering angle limit of 20° to 75° , see Fig. 2.14]. The definition of $F(\sigma'_{|\mathbf{v}_h|})$ [Fig. 4.8(a)] is given by

$$F(\sigma'_{|\mathbf{v}_h|}) = \frac{\max(\sigma'_{|\mathbf{v}_h|}) - \sigma'_{|\mathbf{v}_h|}}{\max(\sigma'_{|\mathbf{v}_h|}) - \min(\sigma'_{|\mathbf{v}_h|})}. \quad (4.10)$$

A horizontal cross-section of the distribution of the quality-index field $F(\sigma'_{|\mathbf{v}_h|})$ for the bistatic dual-Doppler radar system (POLDIRAD + Lagerlechfeld) is shown in Fig. 4.9(a).

Since W_γ and $F(\sigma'_{|\mathbf{v}_h|})$ are fixed for a chosen experimental setup, they can be averaged also to one field. In this case, the averaged field consists of the accuracies of $\sigma'_{|\mathbf{v}_h|}$ and σ_{v_e} which are fixed for an experimental setup. Note that only the influence of the configuration of transmitter, target, and receiver on the accuracy is considered (cf. Sec. 2.7). In Fig. 4.9(b), the average between W_γ and $F(\sigma'_{|\mathbf{v}_h|})$ is shown for the dual-Doppler configuration POLDIRAD and the receiver at Lagerlechfeld. Within the area where this average field exceeds the value of 0.5 (being at $50^\circ \leq \gamma \leq 140^\circ$) wind-velocity measurements are provided with the accuracy of the Doppler velocity measurement ranging between $\sigma'_{|\mathbf{v}_h|} = 2 \text{ m s}^{-1} - 3 \text{ m s}^{-1}$ and spatial resolution varying between 200 m and 700 m (cf. Sec. 2.8). This averaged field can be applied to the real-time display.

4.3.2 Utilizing signal quality based on the reflectivity gradient

In this section, the influence of the weather situation on the measurements is investigated. The investigation focuses on the gradient of the reflectivity factor which gives information about the probability of sidelobe contamination. For a better illustration, the reflectivity factor field of the simulated idealized supercell storm is used (Klemp & Wilhelmson (1978), the storm is described in more detail in Sec. 5.3.1). A horizontal cross-section of the reflectivity factor field at 2 km above MSL is shown in Fig. 4.10(a).

The probability that data measured by the bistatic receiver is contaminated by sidelobes of the transmitted antenna pattern can be expressed by the gradient of the reflectivity factor, $\nabla Z = (\frac{\partial Z}{\partial x}, \frac{\partial Z}{\partial y}, \frac{\partial Z}{\partial z})$. The absolute value of the reflectivity factor gradient can be expressed by the quality-field $F(\nabla Z)$, as seen in Fig. 4.8(b) with

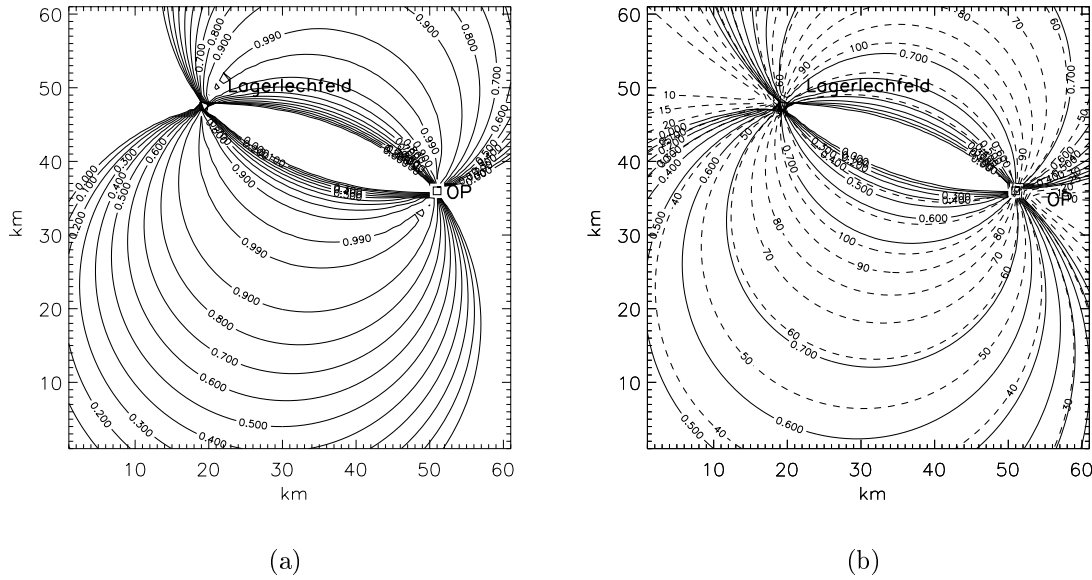


Figure 4.9: Horizontal cross-section at ground level of the quality-index field (a) $F(\sigma' | \mathbf{V}_h)$ and (b) the average field between W_γ and $F(\sigma' | \mathbf{V}_h)$ (solid line) and the scattering angle (dashed line) for the bistatic dual-Doppler radar system consisting of OP and Lagerlechfeld.

$$F(\nabla Z) = \left(30 \text{ dBZ/km} - \sqrt{\left(\frac{\Delta Z}{2\Delta x}\right)^2 + \left(\frac{\Delta Z}{2\Delta y}\right)^2 + \left(\frac{\Delta Z}{2\Delta z}\right)^2} \right) / \left(30 \text{ dBZ/km} \right) . \quad (4.11)$$

The gradient is calculated from the reflectivity factor field measured by the monostatic receiver. For narrow-beam antennas, sidelobe contamination can be ignored, because the signal transmitted through the weak sidelobe is also received by the weak sidelobe (cf. Sec. 2.5). As a result, the reflectivity factor field measured by the monostatic radar can be used as reference. The upper-limit value of 30 dBZ/km is derived from the beam pattern of the transmitting antenna (Fig. 2.11). Here, the first sidelobe of the transmitted beam pattern occurs at about 1.7° away from the main beam, with a reduction of about 32 dB when compared to the mainlobe. Thus, assuming a uniform receiving beam pattern of the bistatic antenna, the gradient of the reflectivity factor has to be about 30 dBZ per 1.7° in order to measure the same signal intensity from the sidelobe as that obtained from the mainlobe by the bistatic receiver.

On a Cartesian grid, the gradient is calculated with centered differences. With a horizontal grid-spacing of about 500 m and a vertical one of about 250 m, the

quality-index field related to the gradient of the reflectivity factor ranges between 0 dBZ/km and 30 dBZ/km. At $F(\nabla Z) = 0$, the probability of sidelobe contamination is very high, while at $F(\nabla Z) = 1$, sidelobe contamination hardly occurs. As an example, the horizontal distribution of $F(\nabla Z)$ is analyzed in Fig. 4.10(b) for the reflectivity factor field of the convective cell [Fig. 4.10(a)]. It should be emphasized again that contamination from sidelobes does not appear in the area of highest reflectivity factor, but within the area of highest ∇Z . Only in this area, the mainlobe of the transmitting antenna points towards weak reflectivity factor, whereas the sidelobe of the transmitting antenna indicates to an area of high reflectivity factor. In case of high sidelobe contamination, the measurements should be dismissed. The impact of $F(\nabla Z)$ on the averaged quality-index field is set by the weighting matrix $W_{F(\nabla Z)}$.

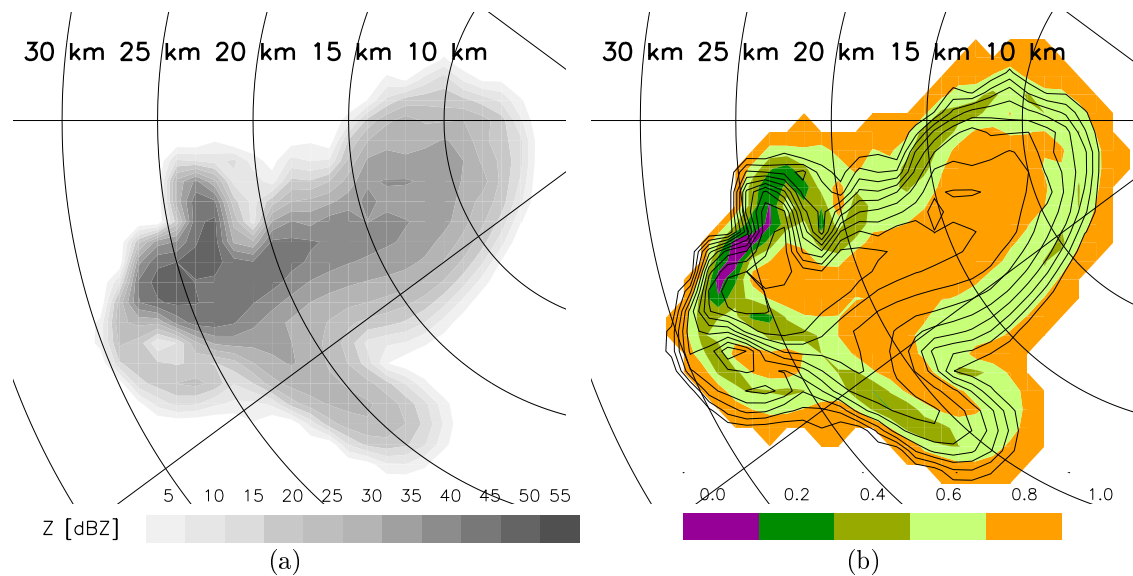


Figure 4.10: Horizontal cross-section at 2 km above MSL of (a) the reflectivity factor field in dBZ for a simulated idealized supercell storm and (b) of $F(\nabla Z)$ (color-coded) calculated from the reflectivity factor field in (a). The isolines indicating the gradient of reflectivity factor are plotted every 5 dBZ starting at the outside of the cell with the 5 dBZ-isoline.

4.3.3 Utilizing signal quality based on fractional uncertainty

The fractional uncertainty field, $\sigma'_{|\mathbf{v}_h|}/|\mathbf{V}_h|$, is used to give information about the percentage accuracy of the horizontal wind-field measurement. The quality-index field $F(\sigma'_{|\mathbf{v}_h|}/|\mathbf{V}_h|)$, related to the wind-field variability, is derived linearly from $\sigma'_{|\mathbf{v}_h|}/|\mathbf{V}_h|$, as exhibited in Fig. 4.8(c) using

$$F(\sigma'_{|\mathbf{v}_h|}/|\mathbf{V}_h|) = \begin{cases} 1 - \frac{\sigma'_{|\mathbf{v}_h|}}{|\mathbf{V}_h|} & \text{for } \sigma'_{|\mathbf{v}_h|} < |\mathbf{V}_h| \\ 0 & \text{for } \sigma'_{|\mathbf{v}_h|} \geq |\mathbf{V}_h| \end{cases} . \quad (4.12)$$

For $\sigma'_{|\mathbf{V}_h|} \ll |\mathbf{V}_h|$, $F(\sigma'_{|\mathbf{V}_h|}/|\mathbf{V}_h|)$ approaches a the value of one. Figure 4.11 shows the horizontal distribution of $F(\sigma'_{|\mathbf{V}_h|}/|\mathbf{V}_h|)$ for the simulated convective cell. The horizontal wind-field of the simulated supercell storm at 2 km above MSL [Fig. 4.11(a)] is used to calculate $F(\sigma'_{|\mathbf{V}_h|}/|\mathbf{V}_h|)$ for the dual-Doppler configuration consisting of POLDIRAD and the receiver at Lagerlechfeld. Because the wind-velocity measurement is an absolute measurement, low wind-speeds lead to low values of $F(\sigma'_{|\mathbf{V}_h|}/|\mathbf{V}_h|)$. In addition, high standard deviations, e.g. close to the baseline or in the quasi-monostatic area, cause low values of $F(\sigma'_{|\mathbf{V}_h|}/|\mathbf{V}_h|)$. The influence of $F(\sigma'_{|\mathbf{V}_h|}/|\mathbf{V}_h|)$ on the average quality-control field is controlled by the weight of $W_{F(\sigma'_{|\mathbf{V}_h|}/|\mathbf{V}_h|)}$.

The weight of this quality-index field on the average quality-index field should be set low within those weather conditions having high wind-shear. For example, as illustrated in Fig. 4.11(b) at an azimuth angle of $200^\circ \leq \phi_t \leq 225^\circ$ and at a range of $r'_t = 20 \text{ km} - 25 \text{ km}$, the wind-speed is very weak and causes $F(\sigma'_{|\mathbf{V}_h|}/|\mathbf{V}_h|)$ to be close to zero, even though $\sigma'_{|\mathbf{V}_h|}$ is low and the wind represents realistic conditions within this area. To avoid a wrong interpretation of $F(\sigma'_{|\mathbf{V}_h|}/|\mathbf{V}_h|)$, $W_{F(\sigma'_{|\mathbf{V}_h|}/|\mathbf{V}_h|)}$ should be set high during stratiform precipitation with wind-speed values larger than 5 m s^{-1} and low during situations with high wind-shear, e.g. convective situations.

The fractional uncertainty can be applied also to the direction of the horizontal wind.

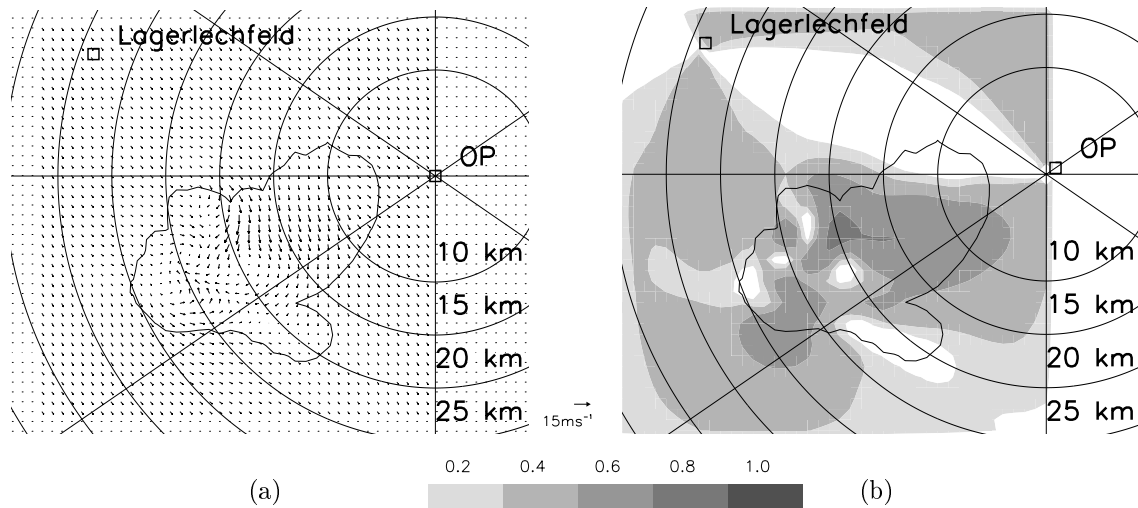


Figure 4.11: Horizontal cross-section at 2 km above MSL of (a) the horizontal wind-vector of the simulated convective cell and (b) the respective quality-index field $F(\sigma'_{|\mathbf{V}_h|}/|\mathbf{V}_h|)$. The 5 dBZ-isoline indicating the shape of the supercell storm is marked.

4.4 Utilizing data consistency

Radar measurements can be contaminated by echoes related to permanent clutter, anomalous propagation above land and sea, aluminum flakes (chaff) used by military

to distract enemy radars, flocks of birds, or swarms of insects (Alberoni et al., 2000). Due to the short scan distance of 50 km used in the bistatic Doppler radar network, contamination due to anomalous propagation can be ignored. Data achieved from the closest 5 km to the radar is always ignored in order to avoid contamination due to ground-clutter in the measured data. Chaff, birds, and insects, however, can contaminate radar data much more heavily. WSR-88D¹⁸ S-band radars have observed reflectivity factors from swarms of insects ranging from -5 dBZ to 20 dBZ in the warm season and from birds even up to 35 dBZ during heavy migration events (Serafin & Wilson, 2000; Gauthreaux & Belser, 1998). Since insects follow air flow and, therefore, can be an aid in measuring wind in the boundary layer, migration of birds, on the other hand, create reflectivity factors and Doppler velocity values which do not represent meteorological processes. Therefore, the quality-control scheme finishes with both an identification and evaluation of perturbations within the horizontal wind-field and their persistence in time and space. A general control proves an errorless operation of each receiver, e.g. ensure the synchronization between transmitter and receiver. To apply the algorithm, information about the entire wind-field of the successive volume-scans is necessary.

4.4.1 Utilizing data consistency based on a persistence check

The persistence check algorithm should help in identifying regions where wind-shear is higher than the mean flow. The regions identified are then tracked in space by means of wind-fields at different elevations and at different time steps (e.g. successive volume-scans). When high wind-shear is identified at different levels and/or in the successive volume-scans, the wind-shear can be related to atmospherical processes. Otherwise, the perturbation is removed.

The persistence check is carried out as follows. The standard deviation in the horizontal wind-velocity, $\sigma_{|\mathbf{v}_h|}$, and direction are calculated. The area is marked, when the difference between the vector mean value, $\overline{\mathbf{V}_h}$, minus the i 'th measured horizontal wind-vector, \mathbf{V}^i is larger than the vector standard deviation, $\sigma_{\mathbf{v}_h}$. For the horizontal wind-velocity this is given as

$$\sigma_{|\mathbf{v}_h|} - |\overline{\mathbf{V}_h} - \mathbf{V}^i| \leq 0 \quad . \quad (4.13)$$

Figure 4.12 shows an example of how this algorithm is applied using the horizontal wind-field of the idealized supercell storm. The shape of the supercell storm is indicated by the 5 dBZ-isoline. The wind-shear within the storm is much higher than the surrounding air flow. Therefore, the area having high wind-shear is marked. Note that if the area marked gray is present in the successive volume scans as well as at neighboring levels, the marked area can then be identified as a signal which is

¹⁸ 'WSR' is *Weather Surveillance Radar*; commissioned in 1988; 'D' is *Doppler capability* used by the National Weather Service, the FAA, and the Department of Defense in the USA [cited from the glossary by Rinehart (1999)]. They are also called NEXRAD.

related to meteorological processes. Otherwise, wind-vectors within this area will be removed. In the case of the supercell storm in Figure 4.12, this convective cell was also visible at neighboring levels and in the volume-scan at the next time step.

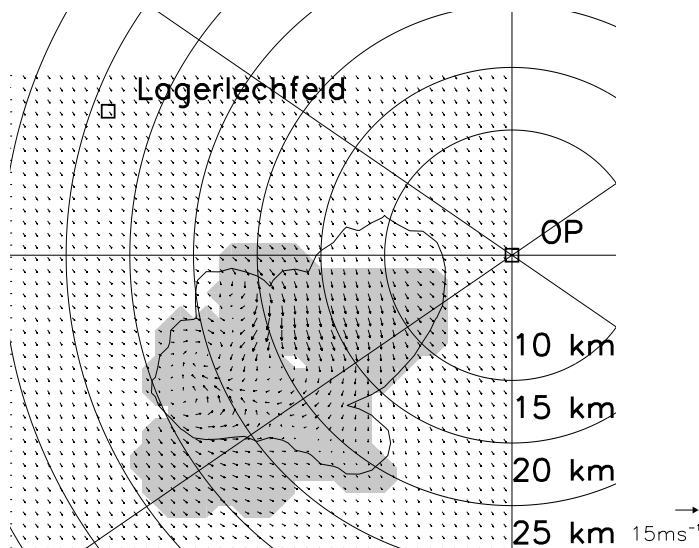


Figure 4.12: Horizontal cross-section of the horizontal wind-vector in m s^{-1} at 2 km above MSL of an idealized supercell storm. The area with wind-shear (direction and absolute value) higher than mean flow is marked. The 5 dBZ-isoline indicating the shape of the supercell storm is marked.

4.4.2 Utilizing data consistency based on an internal check

By means of an internal consistency check, contamination caused by the sidelobe of transmitting beam pattern, migration of birds, and internal hardware problems, e.g. receiver synchronization, can be detected. However, there is a limitation to this control because contamination can only be identified within these areas where the equation system to determine a horizontal wind-field is overdetermined. Checking internally for consistency of data is shown for the wind-vector fields measured during a stratiform precipitation event in the morning hours of 19 June 2001. The Doppler velocities measured by the receivers at Oberpfaffenhofen, Lagerlechfeld, Lichtenau, and Ried as well as the horizontal wind-vector fields are illustrated in Fig. 3.5.

The horizontal wind-field was determined with Doppler velocities measured by two receivers (e.g. receiver #1, receiver #2). From this horizontal wind-field, the Doppler velocities, which should be measured by the two remaining receivers (e.g. receiver #3, receiver #4) were reconstructed [according to Eqs. (2.2) and (2.3)]. The reconstructed and the actual observed Doppler velocities of receiver #3 and receiver #4 were then compared. All six possible combinations were used employing bistatic dual-Doppler processing with Doppler velocities measured by four different receivers.

Figure 4.13 shows the difference between the Doppler velocity measured by Lichtenau and that reconstructed from the bistatic dual-Doppler analysis (OP and Lager-

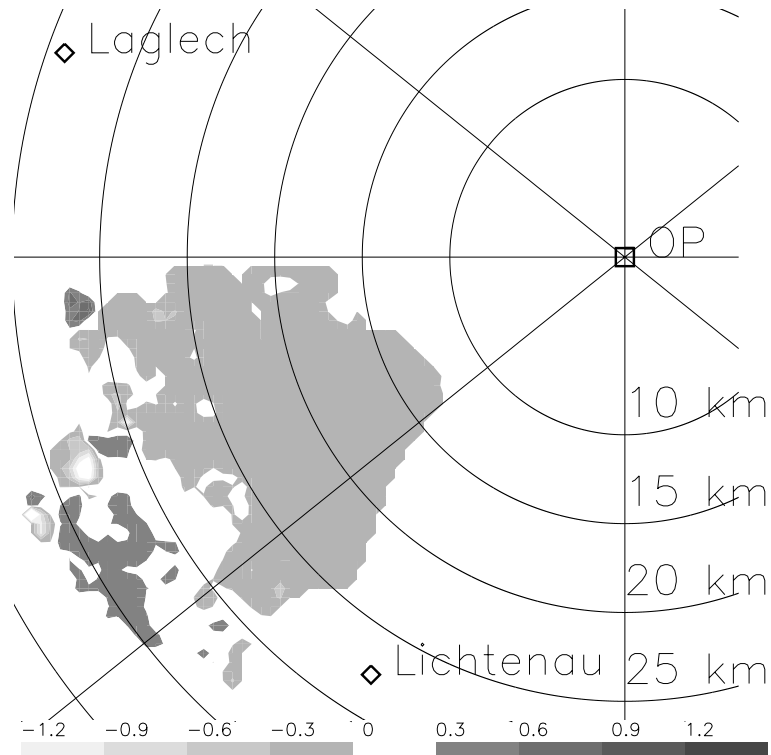


Figure 4.13: Horizontal cross-section at ground level showing differences in m s^{-1} between the Doppler velocity, v_e , when measured by the receiver Lichtenau and reconstructed Doppler velocity for a stratiform precipitation event on 19 June 2001 at 0730 UTC. The reconstructed Doppler velocity is determined from the horizontal wind-field (OP + Lagerlechfeld) which is then projected onto the direction of v_e -Lichtenau.

lechfeld). The difference was on the order of 0.5 m s^{-1} . Other combinations of received Doppler velocities gave similar differences for that stratiform precipitation event. The differences were in the same order for combinations using only bistatic receivers.

The consistency check succeeds when the differences for the whole volume-scan are below $\pm 2 \text{ m s}^{-1}$, which is the same order of magnitude as the accuracy of the wind-field measurements. When major differences occur, for example, when the receivers are not synchronized. Sidelobe contamination can also cause the internal check to fail.

According to de Elia (2000), sidelobe contamination will be present in the radar data of all bistatic receivers when they cover the same area. As a result, it may not be possible to identify which receiver is affected by sidelobe contamination. It is possible only to indicate that sidelobe contamination has occurred when comparing measured and estimated Doppler velocities.

In order to identify n incorrectly-working receivers with this internal check, there has to be $n + 3$ number of receivers covering the same area. Assuming only one receiver fails in a quadruple-Doppler network, the receiver incorrectly operating can be identified by an 'exclusion procedure', as illustrated in Fig. 4.14. First, the internal

OP	Li	La	Ri
x	x	0	0
x	0	x	0
x	0	0	x
0	x	x	1
0	x	1	x
0	1	x	x

OP	Li	La	Ri
x	x	0	0
x	0	x	1
x	0	1	x
0	x	x	0
0	x	0	x
1	0	x	x

OP	Li	La	Ri
x	x	0	1
x	0	x	0
x	1	0	x
0	x	x	0
1	x	0	x
0	0	x	x

OP	Li	La	Ri
x	x	1	0
x	1	x	0
x	0	0	x
1	x	x	0
0	x	0	x
0	0	x	x

Figure 4.14: Schematic view of the possible results achieved with an 'exclusive procedure' for the four receivers, Oberpfaffenhofen (OP), Lichtenau (Li), Lagerlechfeld (La), and Ried (Ri). The horizontal wind-field is estimated by the two receivers marked by a 'x' and is then reconstructed to the respective component of the two remaining receivers. When the consistency check fails it is marked by 0, while when it succeeds it is denoted by 1. The names of the correctly working receivers are colored in black, while the not-correctly working one is colored in gray. More explanation in the text.

check has to be carried out in all possible combinations (in this example there are six combinations for four receivers). If the differences between the reconstructed and measured velocities are smaller than $\pm 2 \text{ ms}^{-1}$, they are considered to be consistent and designated by 1 in Fig. 4.14. Otherwise, they are considered to be inconsistent (designated by a zero). The complete list of results achieved by the internal check must then be compared to the tables shown in Fig. 4.14. In the case of one receiver failure, the result should agree with one of those tables. The names of those receivers correctly working are marked in black, while the name of the receiver working incorrectly is colored gray (in the receiver column no success is designated).

This internal consistency check can be applied also when at least two receiving antennas cover the same area. If this is not the case, in a bistatic Doppler radar network, some antennas could be equipped with a motor, which enables them to be rotated once or twice a day to the area where at least three components of the wind field can be measured. During that time, it is possible to check for receiver synchronization and contamination due to the transmitting sidelobes. Note that while in this case a failure can be detected, the corresponding receiver cannot be identified.

4.4.3 Utilizing data consistency based on a sidelobe contamination check

Targets illuminated by transmitting sidelobes can bias reflectivity, Doppler velocity, and NCP when measured by a bistatic receiver (cf. Sec. 2.5). One source of contamination at low elevations is ground-clutter, which is characterized by having high reflectivity values and zero Doppler velocity. This type of contamination can be reduced by proper filtering (Lee et al., 1995; Hagen, 1997; Seltmann, 2000). If the sidelobes hit those moving targets having intense reflectivity cores, the contamination in the data measured by the bistatic receiver is neither easy to detect nor to filter

out. By reducing the sidelobes of the transmitting antenna pattern in comparison to the mainlobe by about 32 dB per 1.7° (e.g. at POLDIRAD), sidelobe contamination can become critical if gradients of the reflectivity factor exceed about 32 dB per 1.7° . This is the case in situations having strong bright band or during thunderstorms (cf. Sec. 2.5).

To apply the detection algorithms suggested here to a bistatic radar system, it is assumed that the monostatic reflectivity factor is not contaminated by sidelobe effects (see explanations see Sec. 2.5) and, therefore, it is used as a reference field. To detect sidelobe contamination within a bistatic Doppler radar system, however, two solutions are suggested:

(1) Comparing power fields: One way to detect sidelobe contamination is to subtract the reference power field measured by the monostatic receiver from that achieved by a bistatic receiver. The difference can then be linked, for instance, to sidelobe contamination¹⁹. Before applying a direct comparison, however, monostatic and bistatic receivers have to be adjusted. The first step is to correct the power measurements for the receiver–target distance and for the Rayleigh scattering process. According to Eq. (2.20), the range– and scattering–normalized power at a bistatic receiver is calculated as $P_r r_b'^2 \cos^2(\gamma/2) \sin^2(\chi)$ for vertical transmission and reception. For a monostatic receiver, the range–normalized power is given as $P_r r_t'^2$. Second, differences between the upper and lower limits in the dynamic range²⁰ of the two receiver systems have to be taken into account in weather situations reaching those limits. POLDIRAD has a much larger dynamic range than the bistatic receiver. Third, considering other sources, e.g. the transmitting and receiving antenna pattern, $G_t(\phi_t, \theta_t), G_b(\phi_b, \theta_b)$, power measured by the monostatic and bistatic receivers has to be adjusted directly. Therefore, an autark bistatic system consisting of a receiver and a bistatic antenna has to be installed at the monostatic radar site in order to compare the range– and backscattered–normalized power data. This adjustment is best carried out during weather situations having a low probability of sidelobe contamination, e.g. during stratiform precipitation.

When isolated cells of strong reflectivity factor are present as, e.g. during thunderstorms, sidelobe contamination can be easily detected. In the case where the mainlobe of the transmitting power pattern points outside of the cell while the sidelobe hits the main cell, no power can be measured at the monostatic radar system, while power is received by the bistatic site. The ellipsoid of the respective time sample is contaminated. However, these areas can be detected by comparing the normalized power measured by the monostatic and bistatic receiver. One example of sidelobe contamination during a convective situation is given in Fig. 9 and Fig. 10 by de Elia & Zawadzki (2000). The reflectivity factor measured by the monostatic radar system is assumed not to be contaminated (cf. Sec 2.5). Strong contamination is detected at the bistatic receivers along the ellipsoid of constant delay.

¹⁹Receiver synchronization must be guaranteed for this conclusion.

²⁰*The ratio, usually expressed in decibels, of the maximum to the minimum signal that a system can handle. Used to describe limits of receivers [cited from the glossary by Rinehart (1999)].*

(2) Simulation of measured power: By means of the monostatic radar equation, the backscattering cross-section can be derived from power measured by the monostatic receiver. For most weather radar systems ($\lambda \geq 3$ cm) almost all raindrops can be considered small when compared to the wavelength, enabling the Rayleigh approximation to be applied (Rinehart, 1999). The bistatic scattering cross-section can be calculated according to Eqs. (2.10) and (2.11). With this information plus a knowledge of the three-dimensional antenna pattern for both monostatic and bistatic antennas, the power that would have been measured by the bistatic receiver can be calculated according to Eq. (2.20). This calculated power field can then be compared to the measured one and sidelobe contamination can be detected. An example of a sidelobe detection algorithm based on a simulation of the reflectivity field achieved by a bistatic receiver was given by de Elia & Zawadzki (2000).

5 A variational analysis method to determine the vertical velocity

5.1 State of the art

The Doppler velocity when measured by a bistatic receiver consisting of an antenna with a narrow vertical aperture angle ($1^\circ \leq \theta_b \leq 8^\circ$ or $1^\circ \leq \theta_b \leq 22^\circ$) is dominated by the horizontal wind-components u, v . The vertical component of the measured Doppler velocity is very small close to the ground because of low elevations. As a result, the horizontal wind-field can be directly determined from the measured Doppler velocities, while the vertical wind cannot be estimated with sufficient accuracy. Vertical velocities can be determined by integrating the continuity equation vertically.

The idea of combining physical constraints and radar observations to a constraining model is explored to avoid problems associated with the simple vertical integration of the continuity equation. By using a constraining model, it is possible to determine the three components of the wind-vector.

Constraining models were first developed using monostatic single-Doppler radar measurements to retrieve the wind-vector (Tuttle & Foote, 1990; Sun et al., 1991; Qiu & Xu, 1992; Xu et al., 1994; Laroche & Zawadzki, 1994, 1995; Lazarus et al., 1999). Therein, observations of reflectivity and radial velocity were combined with physical constraints. Vertical profiles of the horizontal wind can be used as additional constraints in order to find the absolute minimum of the cost function in the wind retrieval. The wind profiles can be determined from analytical methods, e.g. velocity azimuth display, VAD (Lhermitte & Atlas, 1961; Browning & Wexler, 1968; Orr & Kropfli, 1999), volume velocity processing, VVP (Easterbrook, 1975; Waldteufel & Corbin, 1979), tracking of radial velocity pattern (Smythe & Zrnić, 1983), uniform wind (Persson & Andersson, 1987; Hagen, 1989), and tracking algorithm, TREC (Zawadzki, 1973; Tuttle & Foote, 1990). The constraining models are being constantly improved, e.g. by adding noise filtering techniques (Wüest et al., 2001) or improving vertical integration of the continuity equation (Protat & Zawadzki, 1999).

Notable deficiencies in the results of constraining model are apparent, nevertheless, including uncertainties in the wind-vector determination due to spatial and temporal interpolation errors as well as due to contamination caused by side-lobe and ground-clutter effects. The temporal variations of weather during the volume scan can influence the quality of the wind retrieval also. In the case of monostatic measurements, some of these deficiencies were discussed and solutions were suggested (e.g. filtering, interpolating) in more detail by O'Brien (1970); Miller & Strauch (1974); Doviak et al. (1976); Gal-Chen (1982); Chong et al. (1983); Chong & Testud (1983); Testud & Chong (1983); Shapiro & Mewes (1999).

The most pronounced sources of error affecting the vertical-velocity retrieval are the choice of upper and lower boundary-condition when integrating the continuity equation and the irregular data density due to the scanning character of the mono-

static radar in a spherical coordinate system. Irregular data density can yield unrealistic boundary conditions for the vertical integration of the continuity equation. Usually weather radar systems start scanning at an elevation of 0.5° in order to avoid echos induced by ground-clutter. At 0.5° elevation, for instance, the first radar echo can be expected at a height of 870 m above the radar and at a distance of 50 km.

The measured velocities represent the partical velocity with a terminal fall velocity of w_T [Eqs. (2.2) and (2.3)]. The calculation of w_T when derived from reflectivity values Z may introduce an additional error, e.g. in a severe storm where hail is present, but is not diagnosed as such (Bohne & Srivastava, 1976). Table 5.1 gives an example of the calculation of w_T using the linear radar reflectivity factor z for different weather situations. The variance in the vertical velocity W is given by $\sigma_W^2 = \sigma_w^2 + \sigma_{w_T}^2$, with σ_{w_T} -values of about 2 m s^{-1} – 3 m s^{-1} for raindrops (Atlas et al., 1973) and about 0.5 m s^{-1} for snow (Bohne & Srivastava, 1976). In the following constraining model, the relation between the fall-velocity and the reflectivity-factor is given by (Joss & Waldvogel, 1970; Heymsfield, 1977) as

$$w_T = \begin{cases} -0.33 \cdot 10 \cdot \log_{10}(z) \sqrt{\rho_0/\rho} & \text{for } z < 10^{1.2} \\ -2.6z^{0.107} \sqrt{\rho_0/\rho} & \text{else} \end{cases} \quad (5.1)$$

The second term is the density correction with height, where ρ_0 is the air density at ground level. Furthermore, when the dynamic range of the radar receiver is low it causes problems in measuring strong reflectivity close to the radar (saturation) or low reflectivity far away (low signal-noise ratio).

Table 5.1: An example of the choice of variables for the relation between fall-velocity and reflectivity-factor $w_T = -az^b$ with w_T in m s^{-1} and z in $\text{mm}^6 \text{m}^{-3}$ by Miller & Strauch (1974)

Precipitation type	Source	a	b	σ_{w_T} [m s^{-1}]
Stratiform rain	Rogers (1964)	3.8	0.071	± 1
Thunderstorm	Sekhon & Srivastava (1971)	4.32	0.052	
Widespread rain	Lhermitte (1971)	2.0	0.087	± 0.3
Rain (av. of severe storms)	Joss & Waldvogel (1970)	2.6	0.107	± 1

5.2 Methodology

Laroche & Zawadzki (1994) developed a constraining model for the purpose of retrieving all three components of the wind-vector using monostatic single-Doppler radar observations. Protat & Zawadzki (1999) extended this constraining model for the use of multiple-Doppler data and bistatic Doppler radar data.

The principle in the constraining model is to combine observations with certain physical constraints, as explained by Laroche & Zawadzki (1994, 1995). If the constraint is applied as a strong one, it must satisfy exactly the defined constraining model. Otherwise, if observational errors, assumptions or approximations are allowed, the constraint is set as weak one. In constraining model discussed here, the continuity equation is applied as a strong constraint, while the velocity measurements are used as weak constraints. Observational errors are allowed. The sum of the weak constraints is minimized in the model using the method of conjugate gradients.

5.2.1 The minimization procedure

Here, a sequence for the minimization procedure is given. A detailed description of the constraining model can be found in Laroche & Zawadzki (1994) and Protat & Zawadzki (1999). Those variables u, v, w to be retrieved are called 'control variables'.

1. The control variables u, v are initialized. They can be either set to zero or the translation velocity obtained by the retrieval at the previous time step can be applied as the first guess.
2. The anelastic form of the continuity equation is used to calculate the vertical wind-component w from the retrieved 'control variables' u, v

$$\frac{\partial u}{\partial x} + \frac{\partial v}{\partial y} + \frac{1}{\rho} \frac{\partial}{\partial z}(\rho w) = 0 \quad (5.2)$$

with ρ as the mean air density as a function of z . The retrieved variable w has to satisfy the equation of continuity exactly due to its application as a strong constraint.

3. The differences between the measured Doppler velocities (with a monostatic and bistatic receiver) and the respective Doppler velocities calculated from the control variables are computed by the cost function J_v as

$$J_v = (\mathbf{V}_t - \mathbf{V}'_t)^T W_t (\mathbf{V}_t - \mathbf{V}'_t) + \sum_{p=1}^n (\mathbf{V}_{e_p} - \mathbf{V}'_{e_p})^T W_b(p) (\mathbf{V}_{e_p} - \mathbf{V}'_{e_p}) \quad . \quad (5.3)$$

Here \mathbf{V}_t is a vector containing all the radial components of the wind-field, defined at a given grid-point i by v_{ti} , and \mathbf{V}'_t contains the corresponding observations. The vector containing all the Doppler velocities, measured by the p 'th bistatic receiver, is \mathbf{V}_{e_p} , defined at a given grid-point i by v_{eip} , and \mathbf{V}'_{e_p} contains the corresponding observations. Herein, n is the number of bistatic receivers and $W_t, W_b(p)$ are the weighting matrices for monostatic and bistatic data, respectively. If all the quality criteria are fulfilled according to Sec. 4.3, the weights for the monostatic Doppler velocity observations are set to one. The Doppler velocities measured by the bistatic receiver are weighted according to the scattering angle γ [$W_b(p) = W_\gamma^{(i)}$ in Eq. (3.3)]. The transposed matrix is

denoted by an upper-case T . Moreover, a horizontal smoothness penalty function is applied to prevent the retrieved wind-field from being too noisy. The smoothness constraint, suggested by Wahba & Wendelberger (1980)²¹, is given by

$$J_s = \xi \sum_{\zeta} \sum_{xyz} \left[\left(\frac{\partial^2 \zeta}{\partial x^2} \Delta x^2 \right)^2 + \left(\frac{\partial^2 \zeta}{\partial y^2} \Delta y^2 \right)^2 + 2 \left(\frac{\partial^2 \zeta}{\partial x \partial y} \Delta x \Delta y \right)^2 \right], \quad (5.4)$$

where ζ presents the control variable (u, v) and ξ is the weighting factor. Smoothing is applied as a weak constraint.

Retrieval of the three wind components is then performed by minimizing the following cost function:

$$J = J_v + J_s \quad (5.5)$$

4. The minimization procedure is iterated until the convergence criterion is met. For setting the convergence criterion, balance has to be found between computation time (number of iterations) and a reasonably converged solution. The optimal number of iterations is case dependent. An appropriate number is estimated by examining the behavior of the cost function. To obtain a reasonably converged solution, 200 iterations are used in the following tests on the vertical integration using simulated radar data. The minimization procedure is terminated when the change in the cost function becomes small ($[(J^{i-1} - J^i)/J^i] < 1 \times 10^{-20}$) or the number of iterations is reached. If these predefined convergence criteria have not been met, a new estimate of the control variables u, v is calculated with the conjugate-gradient method for a new iteration (Powell, 1977). The gradient of the cost function is used to determine the search direction.

5.2.2 Vertical integration of the equation of continuity

On a non-staggered grid, the vertical component can be estimated by discretizing the continuity equation with a trapezoidal scheme starting at ground level:

$$w_{x,y,z} = \sum_{xyz} \left[\left(1 + \frac{\Delta z}{H} \right) w_{x,y,z-1} - \frac{\Delta z}{4\Delta x} (u_{x+1,y,z} - u_{x-1,y,z} + u_{x+1,y,z-1} - u_{x-1,y,z-1}) - \frac{\Delta z}{4\Delta y} (v_{x,y+1,z} - v_{x,y-1,z} + v_{x,y+1,z-1} - v_{x,y-1,z-1}) \right], \quad (5.6)$$

where $H^{-1} = \Delta(\ln \rho)/\Delta z$. The lower boundary condition is given by

$$w_{x,y,1} = -\frac{\Delta z}{2\Delta x} (u_{x+1,y,1} - u_{x-1,y,1}) - \frac{\Delta z}{2\Delta y} (v_{x,y+1,1} - v_{x,y-1,1}) \quad (5.7)$$

²¹For more details see also Laroche & Zawadzki (1995) and Wüest et al. (2001).

The main difficulty lies in specifying the upper and lower boundary conditions of w . Zero vertical velocity at the ground is the most natural physical condition (Miller & Strauch (1974); Doviak et al. (1976)). Ray et al. (1980) demonstrated that upward integration of vertical velocity is unreliable because the bias error in the divergence field increases exponentially with height. To reduce the accumulation error, Ziegler (1978) suggested setting $w = 0$ at $z = 0$ and $w = -w_T$ at the upper data boundary [fall-velocity can be derived from the reflectivity factor see Eq. (5.1)]. Note that for radar observations, the lower data boundary often lies hundreds of meters above ground level. Horizontal divergence can be strong near the ground (e.g. for shallow low-level inflows into thunderstorms), which makes it critical to extrapolate analyzed velocities down to ground level.

At lower altitudes the airflow follows the underlying terrain. This has to be considered when calculating w at ground. Topography can be implemented when using the following formula

$$w = u \frac{\partial h}{\partial x} + v \frac{\partial h}{\partial y} \quad , \quad (5.8)$$

with h being the terrain height (Georgis et al., 2001).

5.3 Testing vertical integration with simulated radar data

In the following section, the impact of the integration technique and the influence of irregular data density on the quality of the vertical-velocity retrieval is investigated. Doppler radar data, simulated by a numerical model, were utilized in order to evaluate five different methods for integrating the continuity equation vertically. In a first experiment, integration methods were evaluated by using simulated Doppler radar data at each point over the entire 3D model domain in order to recover all three components of the wind-vector using the constraining model. In the second experiment, the amount (density) of the simulated Doppler radar data was restricted to both the vertical and horizontal antenna apertures of a bistatic antenna.

5.3.1 Experimental design

A well-documented life cycle of an idealized supercell storm (Klemp & Wilhelmson, 1978) was simulated with the French Meso-NH model²² (Lafore et al., 1998; Stein et al., 2000) in a high-resolution domain of 40 km × 40 km × 10 km. The model output was interpolated onto a Cartesian grid with a uniform grid interval of 1 km horizontally and 0.5 km vertically. The simulation was performed over a flat terrain and with open lateral boundary conditions. The convection was initiated by a low-level thermal bubble which was superimposed on an unstable homogeneous environment with high CAPE and 2D wind shear, as given by Klemp & Wilhelmson

²²The simulation data were kindly provided by Evelyne Richard and Jean-Pierre Pinty, Laboratoire d'Aerologie in Toulouse, France.

(1978). This type of sounding is very favorable for the development of a severe long-lived storm which moves, splits, and regenerates several times. The microphysical scheme (Stein et al., 2000) simulated the multiple interactions between water vapor, cloud droplets, small ice crystals, raindrops, snowflakes, and graupel.

After 1 h into the simulation, the initial storm attained a structure typical of an intensifying supercell storm. Figure 5.1 shows horizontal and vertical cross-sections of the storm-relative wind, vertical velocity [vertical section is plotted through the line in Fig. 5.1(a)] and reflectivity at 1 h. A strong updraft associated with a low-level downdraft was evident near the center of the domain. High shear in direction and absolute value of the horizontal wind was present in the whole domain.

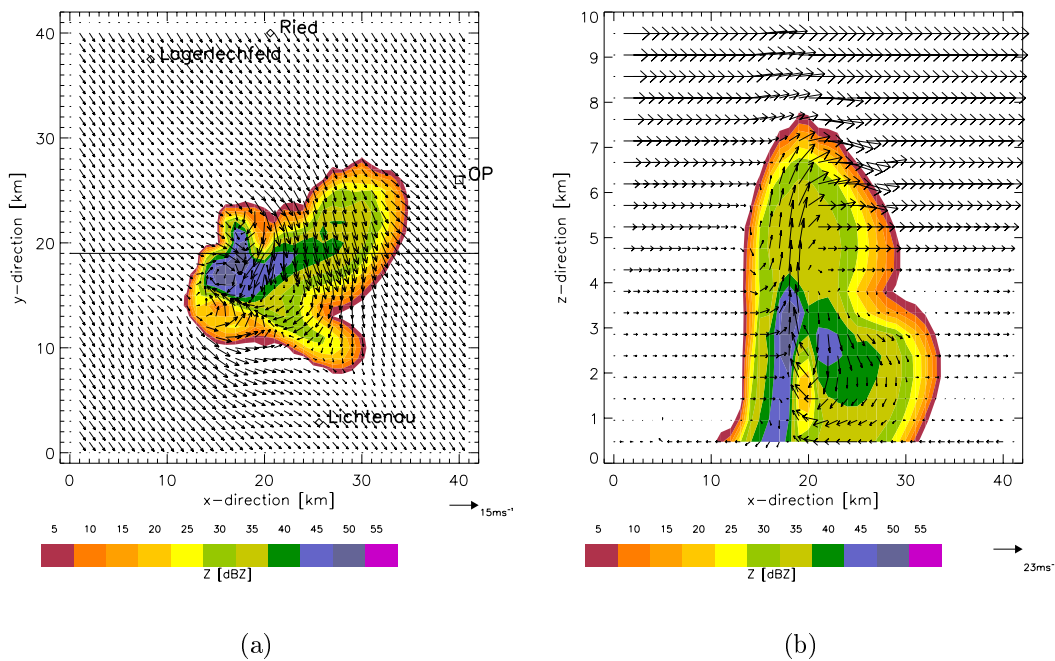


Figure 5.1: The simulated horizontal wind-vectors, u, v , and vertical motion, u, w , in ms^{-1} overlaid by the simulated reflectivity field (color-coded) in dBZ of the supercell storm at 1 h. (a) Horizontal cross-section at $z = 3$ km. (b) Vertical cross-section at $y = 19$ km through line in (a).

Two sets of retrieval experiments were carried out each with a different data density. One set of retrieval experiments assumed no limited horizontal and vertical aperture of the bistatic antennas. Here, the Doppler velocity information at each grid point for the entire $40 \text{ km} \times 40 \text{ km} \times 10 \text{ km}$ model domain was used for the retrieval. The second set of retrieval experiments which was related to realistic conditions within a bistatic Doppler radar network, covered a horizontal area having a scattering angle limit, γ , lying between $50^\circ \leq \gamma \leq 140^\circ$. The vertical antenna aperture, θ_b , was chosen to be $0^\circ \leq \theta_b \leq 8^\circ$. Note that to avoiding contamination due to ground-

clutter, the power pattern of the bistatic antenna is constructed to receive the main power between 1° and 9° vertically. In this experiment, the vertical antenna aperture ranged between 0° and 8° in order to have data close to the ground.

For statistical analysis, the experiment was named according to the integration technique, while the results relating to the second set of experiments were additionally denoted by the index 'bi'. To distinguish between the results achieved by the numerical model and those accomplished by the constraining model, the former was specified by 'simulated' and the latter by 'retrieved'.

It was assumed that the simulated u, v, w -components at 1 h were sampled by the bistatic multiple-Doppler radar network at OP, located as illustrated in Fig. 5.1(a). The wind-components u, v , and $w - w_T$ from the model output were transformed according to Eqs. (2.2) and (2.3) into the Doppler velocities v_t and v_{ei} of the i 'th receiver. The Doppler velocities were used as input data for the constraining model. Afterwards, the retrieved vertical wind, the absolute value of the velocity, and the direction of the horizontal wind were compared to the respective parameters of the numerical simulation. The elapsed time for the volume scan of the pseudo monostatic radar was neglected and simultaneous measurements for all Doppler velocities were assumed. For both sets of experiments, w was set to be zero at the lower and upper-level boundary. The lower boundary was at $z = 0$, while the upper one was located at $z_{top} + \Delta z$, which was at 10.5 km above MSL with $\Delta z = 500$ m.

Different integration techniques were compared to study the integration of the continuity equation:

Upward integration (SUPI): The vertical component was calculated for each grid-column from horizontal divergence fields by integrating the continuity equation upward starting from at ground level using the lower-level boundary condition ($w = 0$). In this case, errors in estimating u, v accumulated upward. Evaluation using this techniques was referred to as SUPI.

Downward integration (SIDO): The continuity equation was integrated downward from the storm top level using the upper-level boundary condition ($w = 0$). Horizontal divergences were calculated when the first radar echo was reached from the top. Errors in the estimation of u, v accumulated downward. When downward integration was used in the constraining model, it was referred to as SIDO.

Averaged integration (AVUDO): This integration technique took advantage of both upward and downward integration using the ground-level and the upper-level boundary conditions ($w = 0$). The results of the separate up- and downward integration at each level were averaged, henceforth AVUDO. The error accumulation was reduced by combining data having a high bias error with data having a lower error. With this technique, the continuity equation was not satisfied exactly.

Weighted up- and downward integration (WUDO): A weighted average of both up- and downward integration was implemented by Protat & Zawadzki (1999) in order to reduce accumulated errors. A linear weight from one at ground and zero at the upper-level boundary height was given for the upward integration (vertical velocity is denoted as w_\uparrow). For the downward integration (vertical velocity is denoted

as w_\downarrow), the weight increased linearly from zero at ground level to one at the highest level. In this way, a strong weighting is given to the integration with the least error for each retrieval height:

$$w = \left(1 - \frac{z}{z_{top}}\right)w_\uparrow + \left(\frac{z}{z_{top}}\right)w_\downarrow \quad . \quad (5.9)$$

The simulation using this integration methods was called WUDO.

Note that WUDO and AVUDO, do not satisfy the continuity equation exactly [see Eq. (5.2)] although, the continuity equation was applied as a strong constraint in the constraining model. The differences between the up- and downward integration create a residual. Montmerle et al. (2001) found that, although the results were consistent and realistic while using radar data, this method led to some non-realistic features in the case where the areas without measurements were supplemented with a background field. Especially at the border between the sampled domain and the background wind-field in a clear-air environment, a non-negligible residual was obtained.

Minimization of up- and downward integration (FUDI): To satisfy the continuity equation exactly, the results of the separate up- and downward integration were minimized within the cost function. The equation of continuity was modified by adding a new weak constraint to the retrieval process (Montmerle et al., 2001). The differences between the up- and downward integration was therefore minimized leading to

$$J_w = \sum_{xyz} [(\mathbf{w}_\uparrow - \mathbf{w}_\downarrow)^T W_w (\mathbf{w}_\uparrow - \mathbf{w}_\downarrow)], \quad (5.10)$$

where W_w is the weighting factor for the vertical velocity. The vector \mathbf{w}_\uparrow contains all vertical components of the wind-field achieved by the upward integration, while \mathbf{w}_\downarrow includes all vertical components of the wind-field achieved by the downward integration defined at a given grid-point. J_w has to be added to the cost function [Eq. (5.5)] leading to $J = J_v + J_s + J_w$. Wind-velocity retrieval based on the minimization of up- and downward integration was referred to as FUDI (forced up- and downward integration).

5.3.2 Results of the retrieval

The results from the two sets of experiments outlined in the previous section are presented below. The statistical analysis is based on the differences between the retrieved and simulated w and the horizontal wind, which were averaged horizontally over each integration level (Figs. 5.2, 5.5) and averaged over the entire domain (Tabs. 5.2, 5.3). The root mean square error (rms), the relative root mean square error (rerms), and the correlation coefficient (cc) were calculated. For statistical analysis, the vertical velocity and the horizontal wind can be assumed to be Gaussian-distributed.

The retrieved wind–field must fulfill the continuity equation and must represent the observations. The continuity equation is a diagnostic equation from which vertical motion is retrieved only. Therefore, it is not a very effective constraint on the horizontal wind. On the other hand, a larger impact on the wind–vector is expected by the minimization procedure using the whole wind–vector. The large differences between the results of the first iteration and the absolute minimum of the cost function (optimally analyzed) can imply a large temporal and computational expense (a large number of iterations) in order to find the global minimum for the cost function.

To begin with, the results of the **first set of experiments**, horizontally averaged over each integration level, are discussed (Fig. 5.2). The choice of the integration technique hardly influenced the horizontal wind [cf. Figs. 5.2(a) – 5.2(c)]. Exceptions were found at the boundary–levels, which can be related to the upper and lower boundary–level conditions chosen for the vertical integration of the continuity equation. Figure 5.3 exhibits the simulated vertical velocity at the upper and lower boundary–level. In the constraining model, w was set to zero at $z = 0$ and at 500 m above the echo top of the supercell storm (upper and lower boundary–level conditions). As approved in Fig. 5.3(a), w can be set to zero at the lower boundary–level. The assumption of $w = 0$, at $z = 10.5$ km was not the right choice as exhibited in Fig. 5.3(b). Here, the vertical velocity, obtained by the numerical simulation, ranged between $\pm 5 \text{ m s}^{-1}$ at a height of 10 km. Therefore, the differences between the results from the simulation and from the retrieval at the 10 km height level were larger for all integration techniques. At the boundaries, the horizontal wind was comparatively well retrieved by the two–way–integration techniques, AVUDO, WUDO, and FUDI. Large differences between the retrieved and simulated horizontal wind were achieved with the one–way–integration techniques, SUPI, SIDO, i.a. at 8 km height $cc_{\mathbf{V}_h}^{\text{SIDO}} = 0.6$ [Fig. 5.2(a)]; between a height of 8 km to 10 km $\text{rms}_{\mathbf{V}_h}^{\text{SUPI}} = 3 \text{ m s}^{-1} - 6 \text{ m s}^{-1}$ [not completely shown in Fig. 5.2(b)]. At lower levels (2 km – 8 km), \mathbf{V}_h was retrieved sufficiently by all integration techniques with cc ranging between 0.8 and 1 [Fig. 5.2(a)], and with a rms increasing from 0.5 m s^{-1} to 2 m s^{-1} [Fig. 5.2(b)].

The statistical analysis of the retrieved and simulated vertical velocities for this supercell storm evidenced that one–way–integration techniques SUPI and SIDO, did not solve the continuity equation sufficiently. The error accumulations for SUPI and SIDO were clearly demonstrated by the correlation coefficients seen in Fig. 5.2(d) with cc below 0.6 for SIDO, and a cc decreasing from 0.7 to zero for SUPI. The highest error accumulation in the vertical wind estimation resulted from the upward integration as already proposed by Ray et al. (1980). The bias of w using classical up– or downward integration was also evident in the vertical profile of the rms (Fig. 5.2(e); $1 \text{ m s}^{-1} \leq \text{rms}_w^{\text{SIDO}} \leq 2.5 \text{ m s}^{-1}$; $\text{rms}_w^{\text{SUPI}}$ increased in height from 0.5 m s^{-1} to 12 m s^{-1}) and in the rerms (Fig. 5.2(f); $1 \leq \text{rerms}_w^{\text{SIDO}} \leq 3$; $\text{rerms}_w^{\text{SUPI}}$ increases in height from 0.5 to 9). The vertical velocity was well retrieved using AVUDO between a height of 2 km to 7 km (Figs. 5.2(d) – 5.2(f); $0.7 \leq cc_w^{\text{AVUDO}} \leq 0.8$, $\text{rms}_w^{\text{AVUDO}} \approx 1 \text{ m s}^{-1}$, $\text{rerms}_w^{\text{AVUDO}} \approx 0.5$). At the upper and lower boundaries, w was

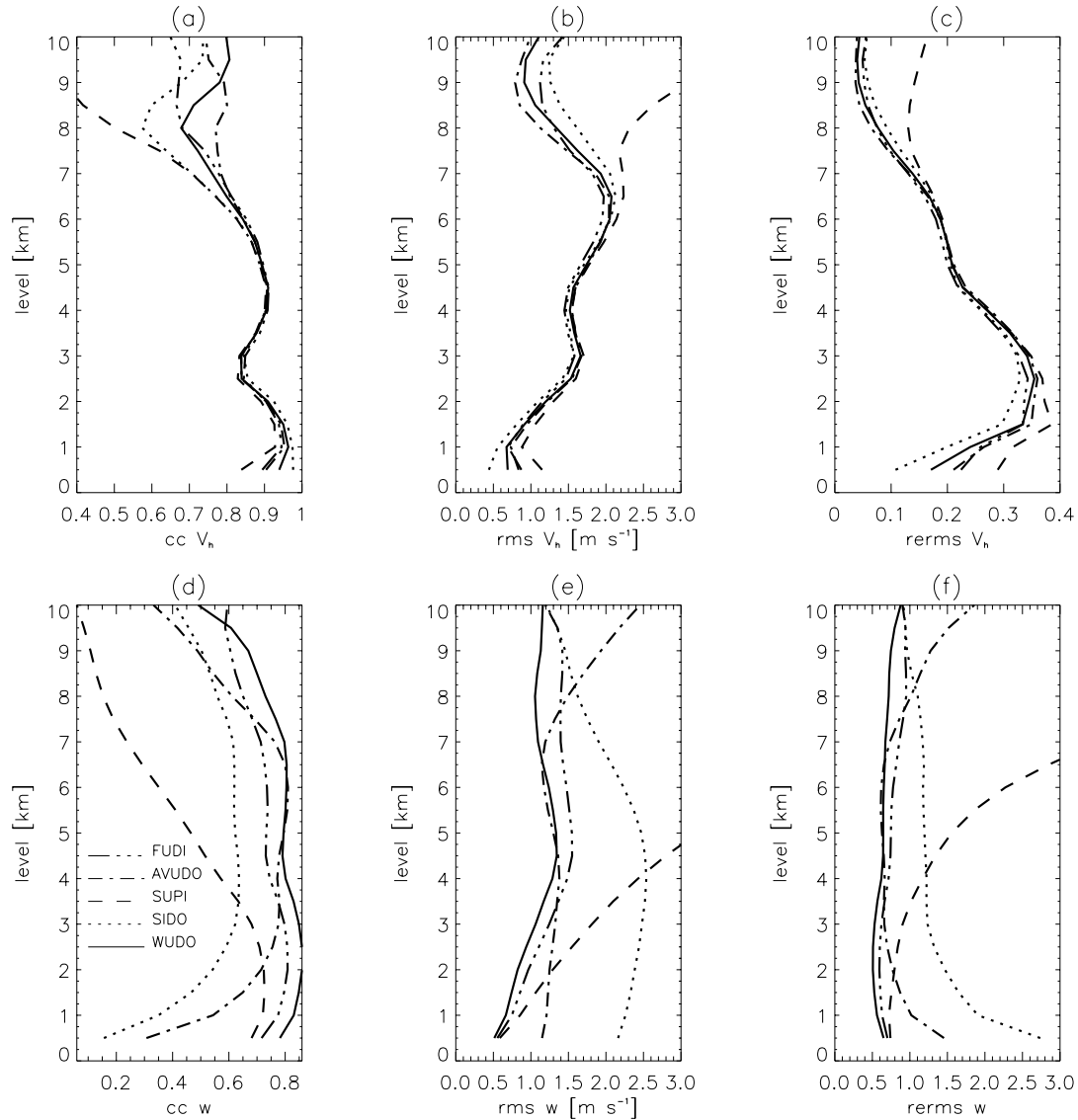


Figure 5.2: Vertical profile of the statistical analysis consisting of the differences between the retrieved and the simulated horizontal wind (a)–(c) and the vertical velocity (d)–(f) averaged over each level height. The simulated Doppler velocities of the entire 3D numerical model domain ($40 \text{ km} \times 40 \text{ km} \times 10 \text{ km}$) were used as input data for the constraining model. The differences between the simulated and the retrieved results were quantified by the correlation coefficient, cc , [(a), (d)], the root mean square error, rms , [(b), (e)], and the relative root mean square error, $rerrms$, [(c), (f)]. The respective integration technique used in the constraining model was signed by FUDI, AVUDO, SUPI, SIDO, and WUDO. More explanations in the text.

retrieved not sufficiently by AVUDO due to the high error accumulation of SUPI at upper levels and SIDO at lower levels. The best results were achieved at all levels with the integration techniques FUDI and WUDO ($0.7 \leq cc_w \leq 0.8$, $rms_w \leq 1.5 \text{ m s}^{-1}$ and

$\text{rerms}_w \leq 1.5$).

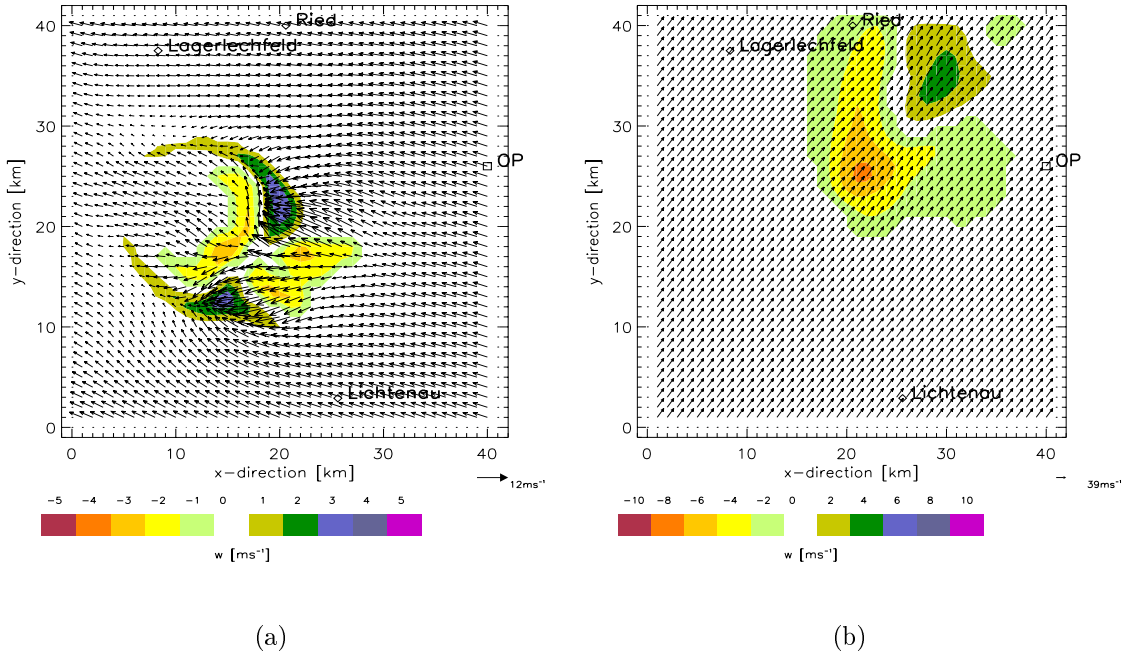


Figure 5.3: Horizontal cross-section of the simulated vertical velocity superimposed on the simulated horizontal wind-vector at (a) $z = 0.5$ km and (b) $z = 10$ km. Downdraft is indicated by negative values and updraft by positive values.

The statistical analysis generated over the entire 3D model domain (Tab. 5.2) showed similar results as the analysis for each level height. The differences between the simulated and retrieved horizontal wind using SIDO, AVUDI, WUDO, and FUDI were small over the whole domain (Tab. 5.2, $\text{rerms}_{\mathbf{v}_h} \approx 0.11 - 0.16$). Although, they were not small for the vertical velocities ($\text{rerms}_w = 0.6 - 1.12$; $cc_w = 0.6 - 0.78$), the general flow structure at each level height correlated well with the results from the numerical simulation (figures not shown). The vertical velocities, calculated with the one-way-integration technique, SUPI (Tab. 5.2; $cc_w^{\text{SUPI}} = 0.23$, $\text{rms}_w^{\text{SUPI}} = 5.8 \text{ m s}^{-1}$), were not sufficiently retrieved. Again, the vertical velocities were determined well by using the integration techniques WUDO and FUDI ($0.72 \leq cc_w \leq 0.78$).

In the **second set of experiments**, the impact of a reduced data density on the quality of the wind retrieval was analyzed. In general, owing to the transmission and reception in spherical coordinates, the data density is reduced, especially, when either close to the ground and far away from the receiver, or at high altitudes and close to the receiver.

Although, the supercell storm was located in the center of the observation domain, it could only be completely observed up to a vertical extension of 2.5 km. Figure 5.4

Table 5.2: The results of the statistical analysis averaged over the entire 3D numerical model domain ($40 \text{ km} \times 40 \text{ km} \times 10 \text{ km}$). The differences between the simulated and the retrieved horizontal wind (\mathbf{V}_h , left) and vertical velocity (w , right) were quantified by the correlation coefficient, cc , the root mean square error, rms , and the relative root mean square error, $rerms$. The respective integration techniques, used in the constraining model, were signed by SUPI, SIDO, AVUDO, WUDO, and FUDI. More explanation in the text.

\mathbf{V}_h/w	SUPI	SIDO	AVUDO	WUDO	FUDI	SUPI	SIDO	AVUDO	WUDO	FUDI
cc	0.97	0.98	0.99	0.99	0.99	0.23	0.61	0.67	0.78	0.72
rms	2.12	1.47	1.39	1.42	1.40	5.78	1.89	1.47	1.08	1.30
[m s^{-1}]										
rerms	0.16	0.11	0.18	0.11	0.11	3.41	1.12	0.87	0.64	0.77

illustrates a horizontal cross-section at 3 km height of the vertical velocity superimposed on the horizontal wind-vector. The simulated supercell storm [Fig. 5.4(a)] could not be covered completely by the vertical aperture of the bistatic antenna as seen in Fig. 5.4(b). At a height of 3 km and 3.5 km, the southern updraft and the main downdraft areas were partly covered by the bistatic receivers, while the northern updraft region was totally out of the observation area [for $z = 3 \text{ km}$ see Fig. 5.4(b)]. For $z \geq 4 \text{ km}$, the supercell storm could not be covered by the bistatic Doppler radar network. Therefore, the integration height was set to 5.5 km. The statistical analysis was limited to the lower five levels (0.5 km – 2.5 km).

The correlation between the results obtained by the numerical simulation and by the constraining model in the second set of experiments was similar to the first set [cf. Figs. 5.4(a) – 5.4(f), Figs. 5.5(a) – 5.5(f)]. Again, the horizontal wind-field was almost unaffected by the integration technique. The vertical profiles of the cc , the rms , and the $rerms$ of the horizontally averaged wind speed resembled to the first set of experiments. Differences between the two sets were to be expected at the upper boundary-level, because of the unrealistic condition of $w = 0$ at 5.5 km height.

The impact of the reduced data density on the vertical integration is clearly seen by the cc exhibited in Fig. 5.5(d). It shows that with the one-way-integration technique, SIDO, w cannot be reproduced ($0 \leq cc_w^{\text{SIDO}} \leq 0.2$). The downward integration started at a height of 5.5 km with w set to zero. At that height, strong divergence was present within the simulated horizontal wind-field. On the other hand, the vertical velocities could be retrieved much better using the upward integration technique, SUPI, with cc_w^{SUPI} ranging between 0.8 and 0.9. In this case, the boundary condition for w was more realistically adjusted than for SIDO. Therefore, the retrieved vertical velocity correlated much better with the simulation results.

The low correlation of the downward integration technique had a large impact on the results achieved with AVUDO ($0.4 \leq cc_w^{\text{AVUDO}} \leq 0.8$). Again, high correlation between the results of the retrieval and the numerical simulation were obtained by using WUDO and FUDI ($0.8 \leq cc_w \leq 0.9$).

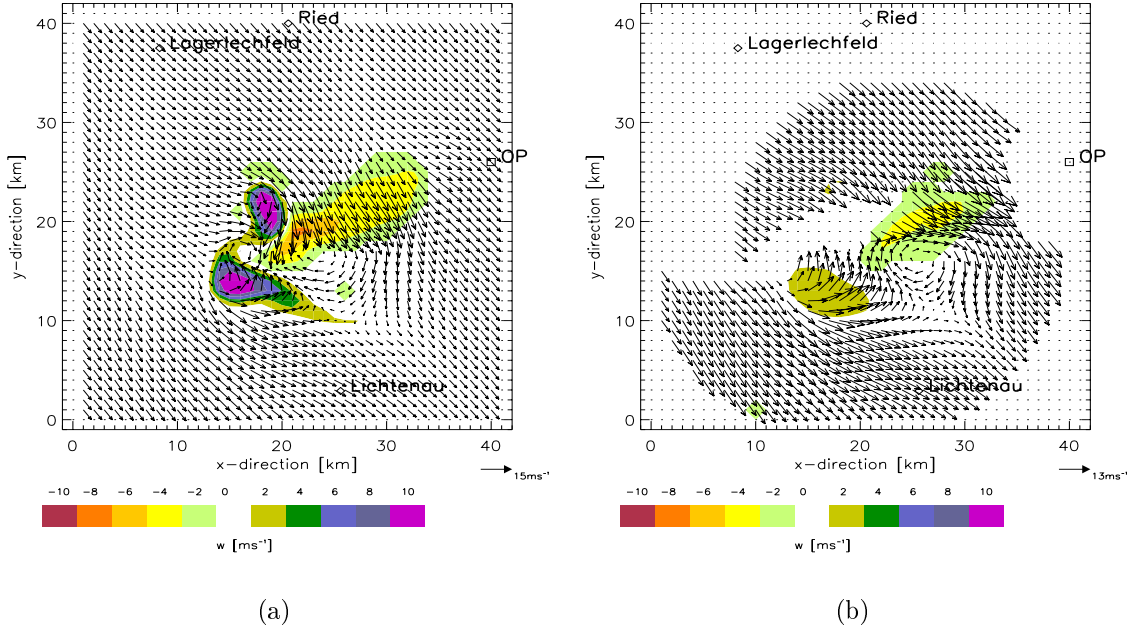


Figure 5.4: Horizontal cross-section at 3 km above MSL of vertical velocity in m s^{-1} superimposed on the horizontal wind-vector field in m s^{-1} obtained by (a) the numerical simulation and (b) the constraining model using FUDI. Upward motion is indicated by positive values and downward motion by negative values. The amount of data, applied in the constraining model, was limited by the aperture of the bistatic antenna with $40^\circ \leq \gamma \leq 140^\circ$ horizontally and $0^\circ \leq \Delta\Theta_b \leq 8^\circ$ vertically.

The comparison between the retrieved and simulated vertical wind-field at each level (figures not presented) showed that both the up- and downdraft motions were overestimated in magnitude using SUPI. But the structure of the northern and southern updraft, and the downdraft area in the center of the domain was well obtained. In stark contrast, the one-way downward integration techniques, SIDO, could hardly give the structure of the three cells. There was no correlation, however, between the simulated and retrieved vertical wind-fields. Using AVUDO, WUDO, and FUDI, the size of the updraft region was larger than in the simulation, while the values of downdraft were overestimated. The vertical wind-field was well represented by WUDO and FUDI.

Comparing the statistical parameters generated over the whole 3D domain of the first set of experiments to the second, the impact of the upper boundary conditions on the quality of the vertical-velocity retrieval was only clearly evident by the downward integration (Tab. 5.3, $cc_w^{\text{SIDO}} = 0.47$, $cc_w^{\text{SIDO}bi} = 0.20$). In all other cases, the cc, the rms, and the rerm of the whole domain were similar. The retrieval of the wind components was less sensitive to the limited amount of data than expected. The results achieved with lower data density in Tab. 5.3 (denoted by *bi*) should not be

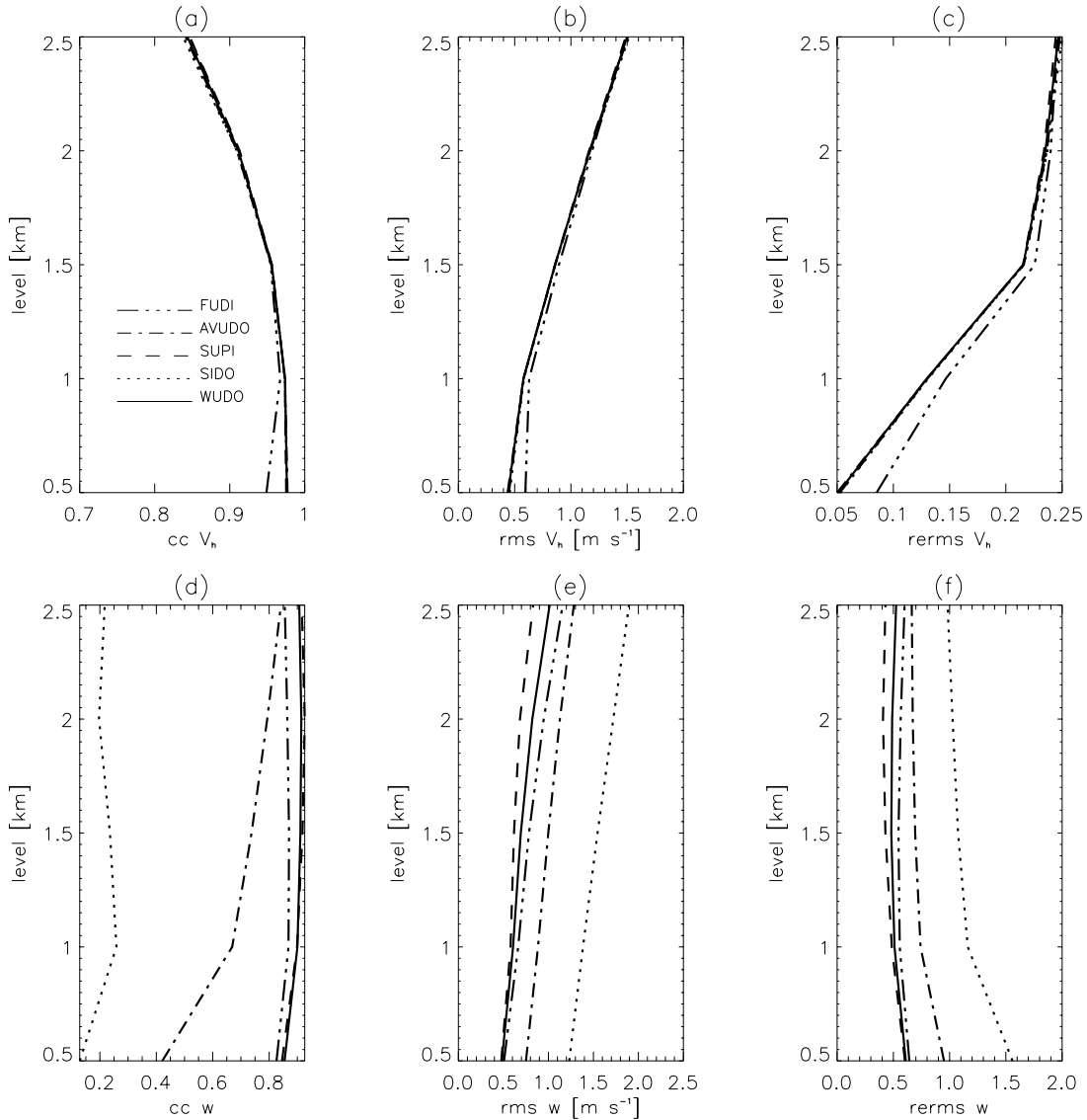


Figure 5.5: As Fig. 5.2, but the amount of data used in the constraining model was reduced. The observation area of the three bistatic receivers was restricted by $40^\circ \leq \gamma \leq 140^\circ$ horizontally and $0^\circ \leq \Delta\Theta_b \leq 8^\circ$ vertically.

overestimated. The differences in the cc between the first and the second set of experiments can be related to the different numbers of samples.

5.3.3 Assessment and discussion

Sampling up to the echo top of a convective cell can become critical for a bistatic antenna receiving the main power within 1° to 9° vertically. But the knowledge of the echo top height is essential for choosing the right integration technique with realistic boundary conditions. For measurements in convective situations, it is suggested

Table 5.3: The results of the statistical analysis for the lower five levels (0.5 km - 2.5 km). The simulated w was averaged over $40 \text{ km} \times 40 \text{ km} \times 2.5 \text{ km}$ (5240 samples) and the retrieved w , denoted by b_i , was averaged over the area, which was restricted by the aperture of a bistatic antenna (5024 samples). The differences were quantified by the correlation coefficient, cc , the root mean square, rms , and the relative root mean square, $rerm$ s. The integration techniques applied in the constraining model were signed by SUPI, SIDO, AVUDO, WUDO, and FUDI, respectively. More explanations the text.

w	SUPI	SUPI $_{b_i}$	SIDO	SIDO $_{b_i}$	AVUDO	AVUDO $_{b_i}$	WUDO	WUDO $_{b_i}$	FUDI	FUDI $_{b_i}$
cc	0.71	0.91	0.47	0.20	0.65	0.73	0.85	0.90	0.79	0.86
rms	1.12	0.64	2.32	1.56	1.23	1.02	0.75	0.74	0.87	0.83
[m s^{-1}]										
rerm s	0.79	0.44	1.63	1.08	0.86	0.70	0.53	0.51	0.61	0.58

that the echo top height be determined with an RHI measurement²³ or a complete volume scan. If the echo top cannot be reached for sure due to the limited vertical antenna aperture of the bistatic antenna, and sampling finishes within an area of high reflectivity and high convergences in the horizontal wind-field, the upward integration technique has to be used to calculate w . Otherwise, minimizing the results of the up- and downward integration is favorable. Here, the ground-level and upper-level boundary conditions are taken into consideration.

Setting $w = 0$ at the upper and lower boundary conditions is easy to accomplish and sufficient for this case. Even though the condition $w = 0$ at the upper-level boundary is not met in the second set of experiments, only the quality of the wind retrieval using the one-way integration technique, SIDO, was influenced by starting with a very high gradient in the vertical velocity at the upper boundary-level (at a height of 3 km $w = 0$, and at a height of 2.5 km $w = \pm 5 \text{ m s}^{-1}$).

The assumption of $w = -w_T$ as upper boundary condition as suggested by Ziegler (1978) could not be applied in this case study because w_T is zero at the upper boundary. At the highest level containing reflectivity (9 km), the terminal velocity w_T is about 1 m s^{-1} (figure not shown) within the downdraft area in Fig. 5.3(b) ($x = 20 \text{ km}$, $y = 24 \text{ km}$ with a radius of 5 km). At a height of 8.5 km, the downdraft of this area reaches values of about 1 m s^{-1} to 4 m s^{-1} (figure not shown). At that height (8.5 km), $w = -w_T$ represents the realistic upper-level boundary condition (Fig. 5.3). Since the true vertical velocity is unknown, this shows the difficulties of setting $w = -w_T$.

For a more precise statement on the impact of data density and boundary conditions on the quality of the retrieved wind-vector, these experiments have to be extended for a large number of different weather situations.

²³ 'Range-Height Indicator - An intensity-modulated display with height as the vertical axis and range as the horizontal axis. A cross-section in a vertical plane passing through the radar [cited from the glossary by Rinehart (1999)].'

6 Retrieval of wind-fields

6.1 Stratiform precipitation in a frontal system: 2 February 2000

6.1.1 Meteorological situation and data analysis

On the afternoon of 2 February 2000, a cold frontal system passed over southern Germany from the northwest. The pre-frontal wind was mainly from southwesterly and westerly directions, ranging from between 10 m s^{-1} – 15 m s^{-1} and increasing and veering more to a westerly flow as the cold front approached. As recorded by three meteorological surface observation stations (Oberpfaffenhofen, Lagerlechfeld, Dießen; for their location see Fig. 1), the surface front passed the investigation area between 1630 UTC – 1830 UTC, reaching Lagerlechfeld at 1630 UTC, passing Oberpfaffenhofen (OP) between 1715 UTC – 1725 UTC, and reaching Dießen between 1720 UTC – 1745 UTC (Fig. 1). Precipitation started within the warm sector of the frontal system at 1435 UTC in Lagerlechfeld, 1530 UTC in Oberpfaffenhofen, and 1600 UTC in Dießen.

Volume scans were performed every ten minutes by POLDIRAD and the receiver system at Lagerlechfeld, during a time period of seven hours (1200 UTC – 1900 UTC). Wind synthesis was performed, as described in Sec. 4.1 and in Sec. 4.2. Radar data were interpolated onto a Cartesian grid with a horizontal resolution of 500 m and a vertical resolution of 250 m, starting at 600 m above MSL, i.e. at the height of POLDIRAD, up to a height of 2.85 km above MSL. The measured velocities, v_t and v_e , were used as input data for the constraining model in order to retrieve the three components, u, v, w of the wind-vector (Sec. 5). The vertical integration was achieved with the FUDI-technique because with this two-way-integration, the continuity equation is satisfied exactly and the technique considers both ground-level and upper-level boundary conditions (cf. Sec. 5.3). The quality control scheme was applied to the horizontal wind-vector and the averaged quality index field (Sec. 4.3) was calculated.

6.1.2 Assessment and discussion

During the whole investigation period, up- and downward motion with values of up to $\pm 1.5 \text{ m s}^{-1}$ were observed. Pre-frontal (between 1200 UTC – 1700 UTC), the vertical motion was dominated by ascending air, with w about 0.6 m s^{-1} (figure not shown), while shortly after the front passed, downward motions were dominant within the observation area. Figures 6.1(a) and 6.2(a) show the horizontal wind-vector underlaid by the vertical velocity during the frontal passage at 1708 UTC and after the frontal passage at 1758 UTC, respectively. At 1708 UTC, the frontal system was located SW of OP (between $220^\circ \leq \phi_t \leq 230^\circ$), heading southeast. In Fig. 6.1(a), a perturbation can be detected SW of OP with a slight change in wind direction (from SW to W), with pre-frontal upwinds and post-frontal downwinds.

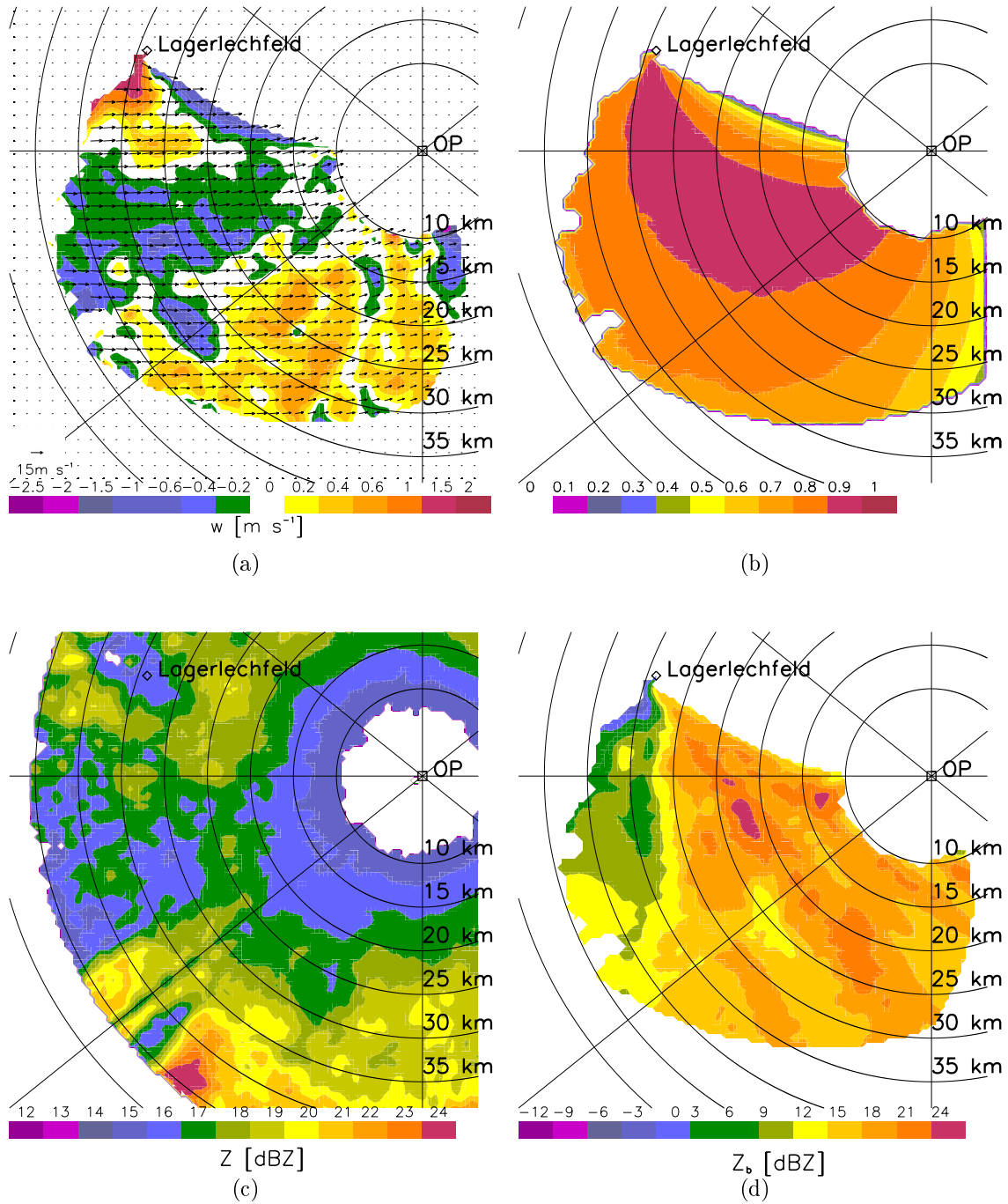


Figure 6.1: Horizontal cross-section at a height of 1.6 km above MSL of the (a) retrieved horizontal wind-vector underlaid by vertical velocity in m s^{-1} , (b) the respective quality index field of the horizontal wind, (c) the reflectivity factor field measured by POLDIRAD in dBZ, and (d) the bistatic reflectivity factor field in dBZ measured by the receiver Lagerlechfeld on 2 February 2000 at 1708 UTC. Updraft motions are indicated by positive values, and downdraft by negative values. For clarity of display, only every third wind vector is plotted.

At 1758 UTC, the direction of the horizontal wind-vectors changed to NW, and the wind velocity increased up to 20 m s^{-1} . Downward motions, indicated by negative values, dominated. The averaged quality index fields of the horizontal wind-vector at 1708 UTC and at 1758 UTC are exhibited in Fig. 6.1(b) and Fig. 6.2(b), respectively. In this case, which shows a weather situation with a relatively homogeneous flow, the average quality-index field, \bar{F} , is dominated by the accuracy of the horizontal wind-field, $F(\sigma'_{|\mathbf{V}_h|})$ [cf. Sec. 4.3.1 and Fig. 4.9(a)]. The quality-index fields $F(\nabla Z)$ and $F(\sigma'_{|\mathbf{V}_h|}/|\mathbf{V}_h|)$ are very small. Only wind-vector and values of reflectivity factor where the average quality index field exceeded a value of 0.6 (empirically chosen) were plotted. Within this area, the confidence in the Doppler velocity measurements was high (cf. Sec. 2.8), and a large number of data points was available.

The bistatic reflectivity factor field, Z_b , measured by the bistatic receiver Lagerlechfeld (cf. Sec. 2.4), and the reflectivity factor field measured by POLDIRAD, are shown in Figs. 6.1(c) and 6.1(d) for 1708 UTC and in Figs. 6.2(c) and 6.2(d) for 1758 UTC, respectively. By means of the reflectivity factor field, the vertical motion of microphysical processes can be derived. As a simple approach, higher reflectivity factors are expected more in updraft regions as compared to downdraft areas. Within stratiform precipitation this approach cannot be applied within the bright band. At 1708 UTC, a downdraft [Fig. 6.1(a)] was related to low reflectivity factors ranging between 16 dBZ and 18 dBZ, while an updraft was visible in the region SSW of OP having higher reflectivity factors ranging between 20 dBZ and 24 dBZ. As downward motion dominated the area after the frontal passage at 1758 UTC, the reflectivity was weaker than at 1708 UTC. The upward motion to the south of OP [Fig. 6.2(a)] was still linked with the area of higher reflectivity at 1758 UTC.

The bistatic reflectivity factor field measured by the bistatic receiver Lagerlechfeld can only illustrate the received power-pattern of its antenna. Comparing Fig. 6.1(d) and Fig. 6.2(d) with the measured antenna power-pattern in Fig. 3.3(a), the mainlobe and the secondary lobes of the bistatic antenna were visible in the bistatic reflectivity factor field measured on 2 February 2000.

In order to show that the vertical velocity-field has a clear meteorological signal, several sensitivity studies on the impact of observation errors on the retrieved components, u, v, w were carried out. This investigation showed that the retrieval algorithm including smoothing as a constraint (Sec. 5) is not susceptible to random measurement errors. Therefore, prior to starting the wind retrieval, a random number was added to the measured velocities v_t and v_e after the interpolation onto a Cartesian grid. Smoothing was applied only in the minimization procedure [Eq. (5.4)]. The retrieved components, u, v, w at 1758 UTC, with an artificially added error ranging between -2 m s^{-1} to 2 m s^{-1} onto v_t and v_e , can be seen in Fig. 6.3. The comparison between this wind-vector field (Fig. 6.3) and the wind-field at 1758 UTC without an added error [Fig. 6.2(a)] shows that the retrieval has a low sensitivity to measurement errors. Even when allowing for a margin of error of between -5 m s^{-1} to 5 m s^{-1} (which corresponds to 25 % for 20 m s^{-1} ; figure not shown) up- and down-draft

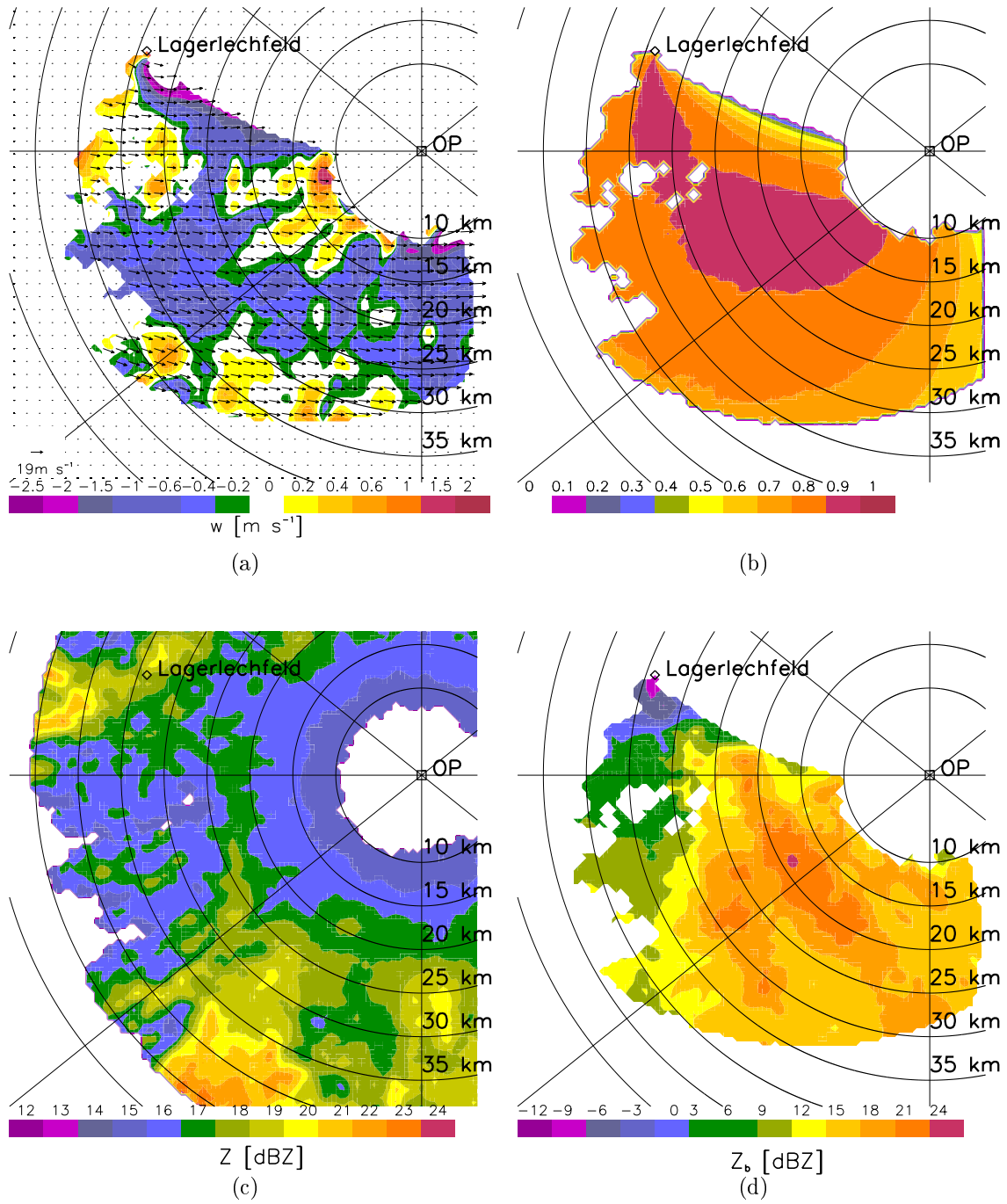


Figure 6.2: As Fig. 6.1, but at 1758 UTC.

structures, as in Fig. 6.2(a), are visible.

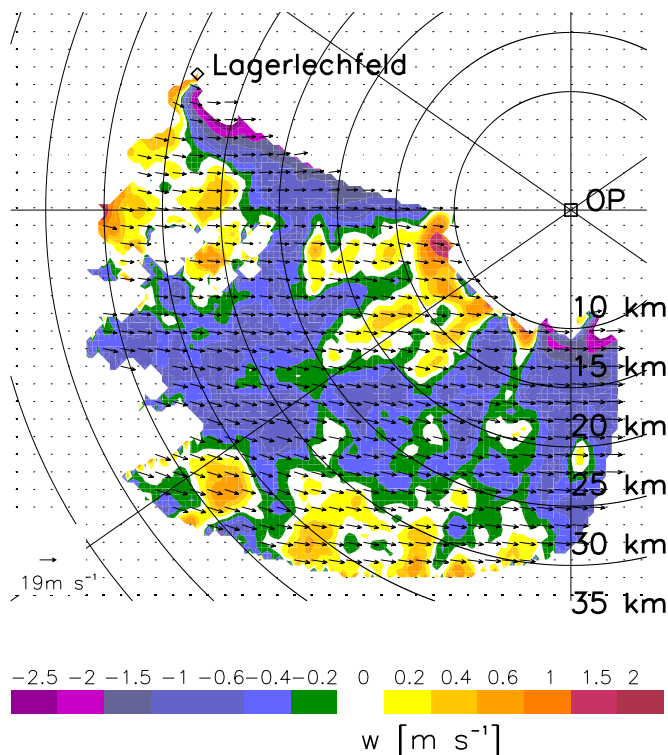


Figure 6.3: As Fig. 6.2a, but before starting the retrieval procedure, a random number ranging from between -2 m s^{-1} to 2 m s^{-1} was added onto each v_t and v_e .

As a result, clear meteorological structures in the vertical velocity were visible within the observation area. The overall structure of the vertical motion associated with a frontal passage can be verified.

6.2 Stratiform precipitation in a frontal system: 10 April 2001

6.2.1 Meteorological situation and data analysis

In the second case, a weak cold front with stratiform precipitation passed the investigation area in the afternoon of 10 April 2001 between about 1600 UTC – 1700 UTC. Because precipitation was mainly within the warm sector of the frontal system, velocity measurements with the bistatic Doppler radar network could only be obtained until 1530 UTC.

Before the frontal system reached the investigation area, the wind was characterized by a relatively homogeneous southwesterly flow, with velocities ranging between 10 m s^{-1} and 15 m s^{-1} . With the front's approach, the horizontal wind varied between westerly and northwesterly directions but did not change in magnitude.

Volume scans were performed every ten minutes by POLDIRAD and the receiver system Lichtenau and Lagerlechfeld during a time period of about three hours (1230 UTC – 1530 UTC). Wind synthesis was performed as for the first case (cf. Sec. 6.1.1). The Doppler velocities measured by the receivers Oberpfaffenhofen, Lichtenau, and Lagerlechfeld were used as input data for the constraining model. Note that with two bistatic receivers, the equation system to determine the horizontal wind–field was mainly overdetermined within the observation area. The vertical velocity was retrieved using the FUDI technique (cf. Sec. 5.3.1). The time levels of the retrieval were at 1327 UTC, 1427 UTC, and 1447 UTC before the frontal passage.

6.2.2 Assessment and discussion

The vertical wind–field superimposed on the horizontal wind–vector field, and the corresponding average quality index field of the horizontal wind between 1327 UTC and 1447 UTC are illustrated in Fig. 6.4 and Fig. 6.5, respectively. The influence of an overdetermined equation system for the horizontal wind–field calculation on the averaged quality index field can be seen clearly when comparing Fig. 6.1(b) and Fig. 6.4(b). According to the quality index field [Figs. 6.4(b) and 6.4(d); Fig. 6.5(b)], the confidence in the horizontal wind–field is high within the whole observation area with values ranging between 0.7 and 0.8.

At all three time levels, the retrieved vertical velocity was characterized by relatively small up– and downward motions due to the low values of horizontal convergence. At 1327 UTC, the wind came mainly from westerly and southwesterly direction, with velocities ranging from 10 m s^{-1} to 15 m s^{-1} [Fig. 6.4(a)]. A horizontal convergence in the wind–field was observed in the northern and southern parts which could be linked to upward motion with values of w up to 1 m s^{-1} . This convergence occurred at all height levels (figures not shown). When the wind changed to a more westerly direction, at 1437 UTC [Fig. 6.4(c)] and at 1447 UTC [Fig. 6.5(a)], the most southern region of convergence disappeared and the upward motion reduced. The most northern region of convergence was still present at 1437 UTC and 1447 UTC. Generally, very low subsidence occurred over the whole observation area.

6.3 Wind–vectors within a convective system: 3 May 2000

6.3.1 Meteorological situation and data analysis

On the afternoon of the 3 May 2000, two convective systems formed southwest and later northwest of Oberpfaffenhofen. The cell located within the investigation area started developing around 1400 UTC and stayed within the observation area for one hour. At about 1445 UTC, a second cell located northwest of Oberpfaffenhofen formed. The 1° elevation PPI of the reflectivity factor field measured by POLDIRAD at 1435 UTC and the lightning observations between 1330 UTC and 1530 UTC shown in Fig. 6.6 illustrate the position of the convective system. The most active part of the system located southwest of OP (i.e. related to the maximum of the reflectivity

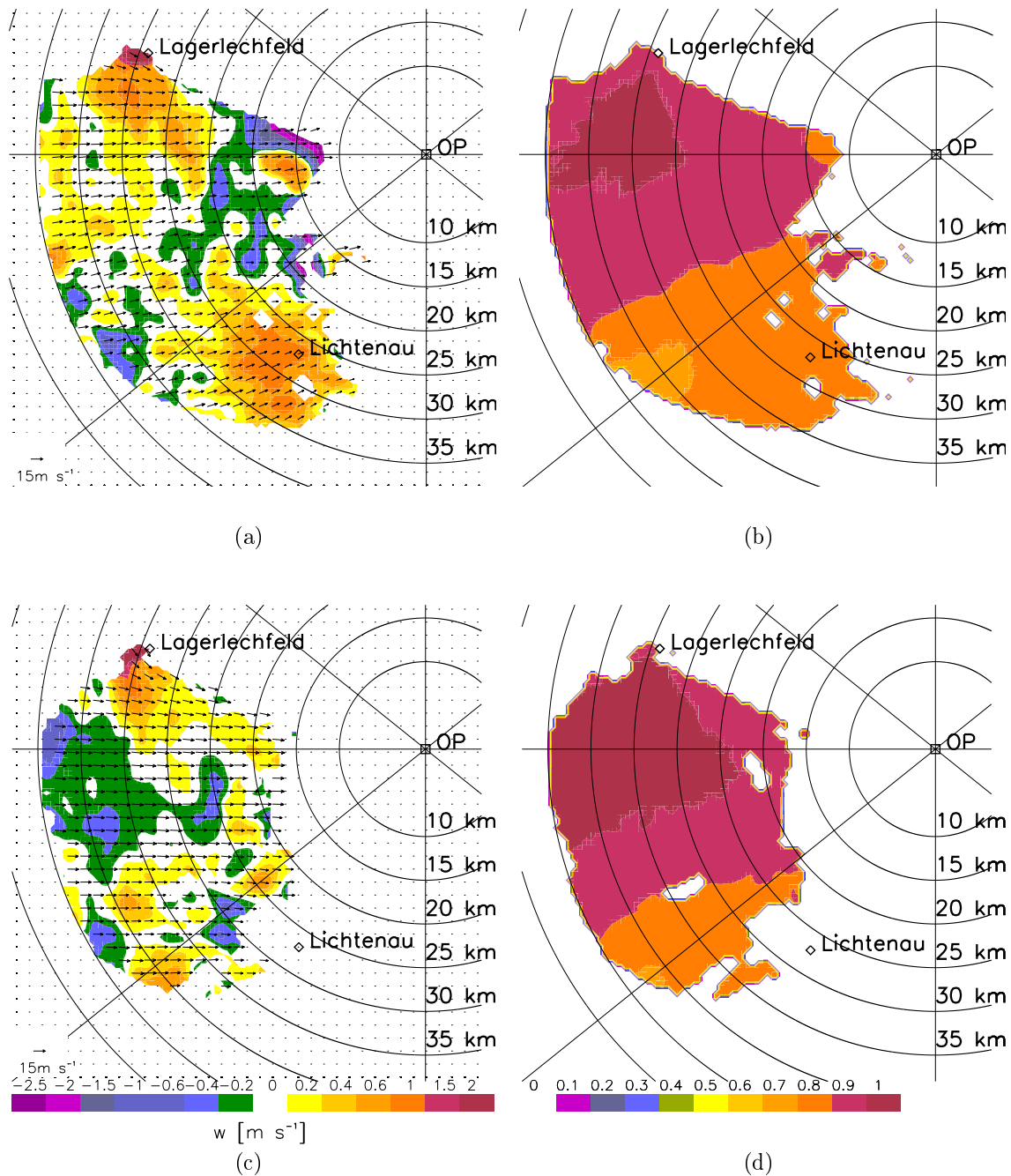


Figure 6.4: Horizontal cross-section at a height of 1.6 km above MSL of the retrieved horizontal wind-vector underlaid by vertical velocity in m s^{-1} (left column) and the respective quality index field (right column) of the horizontal wind measured on 10 April 2001 at (a), (b) 1327 UTC and (c), (d) 1427 UTC. Data were sampled by the receivers Oberpfaffenhofen, Lichtenau, and Lagerlechfeld. Upwinds are indicated by positive values, while negative values are downwinds. For clarity of display, only every third wind vector is plotted.

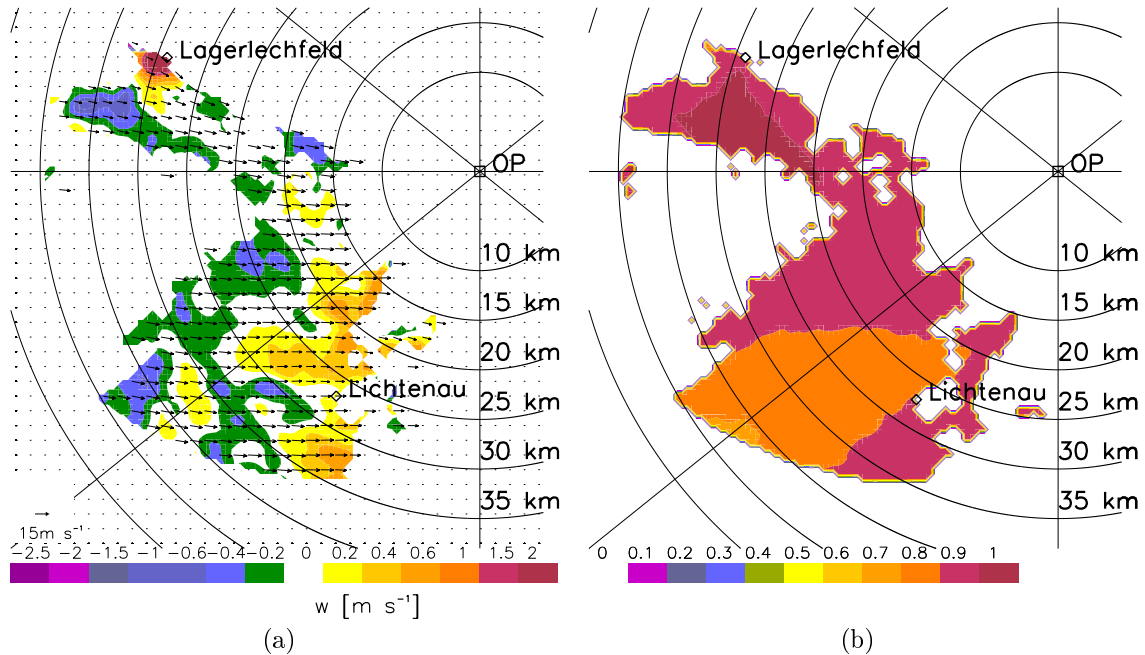


Figure 6.5: As Fig. 6.4, but at 1447 UTC.

factor) consisted of a stationary cell located between $225^\circ \leq \phi_t \leq 280^\circ$ at a range of $15 \text{ km} \leq r'_t \leq 30 \text{ km}$.

To observe the temporal evolution of the convection, volume scans were performed by POLDIRAD every ten minutes. With a scanning rate of about 40 seconds per revolution, eight antenna elevations were scanned starting at 1° and running up to an elevation of 20° with smaller elevation intervals near ground level and larger intervals with increasing height. Due to a maximum scanning elevation of 20° and a limited vertical aperture of the bistatic antenna of about 1° to 9° , data were only sampled up to a height of 7.5 km to 11 km above MSL located at $r'_t = 20 \text{ km} - 30 \text{ km}$.

Contamination due to the secondary lobes of the transmitting power pattern (cf. Sec. 2.5) did not occur during this convective situation. Figure 6.7 shows the bistatic reflectivity factor field measured by the receiver Lagerlechfeld at 1.6 km above MSL at 1455 UTC. If the data measured by the bistatic receiver were found to be contaminated by the transmitted secondary lobe, the bistatic reflectivity factor would be extended in the direction of the ellipsoid of the respective range gate (cf. Sec. 2.5). As illustrated in Fig. 6.7, the maximum reflectivity factor expands in the radial direction from the bistatic receiver according to the received power-pattern and not along the ellipsoid. An example of a sidelobe-contaminated bistatic reflectivity factor field measured by a bistatic receiver is given in Fig. 9 and Fig. 10 in de Elia & Zawadzki (2000). In addition to the conclusion drawn from the reflectivity factor field, no contamination can be found in the Doppler velocity field (Figure not shown). The comparison between the Doppler velocity measured by the monostatic and bistatic

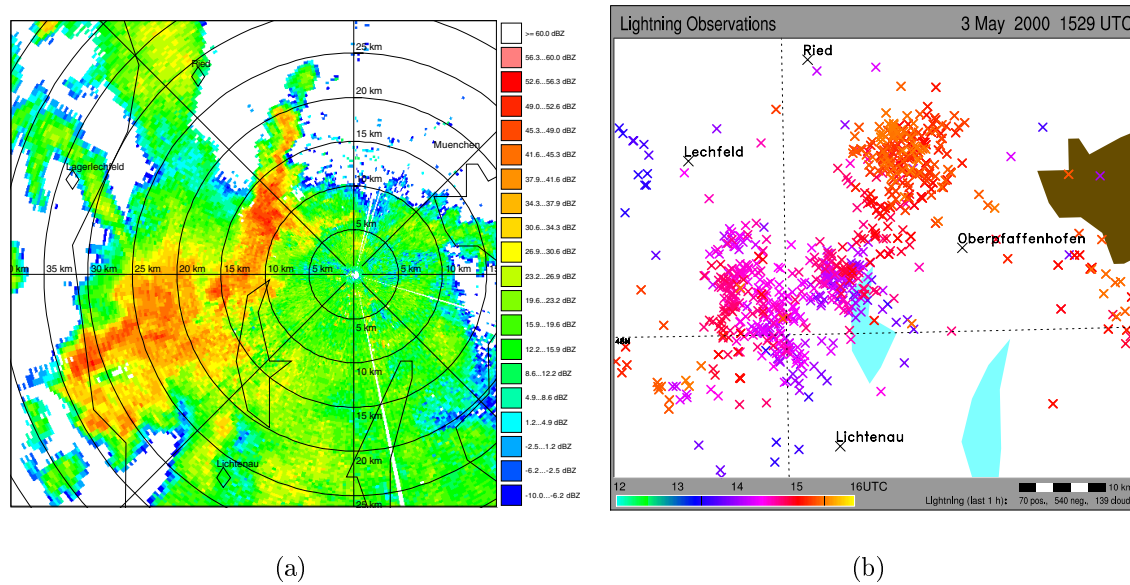


Figure 6.6: PPI at 1° elevation of the reflectivity factor field in dBZ measured by POLDI-RAD at 1435 UTC. (b) Position and color-coded time of the observed lightning between 1330 UTC and 1529 UTC.

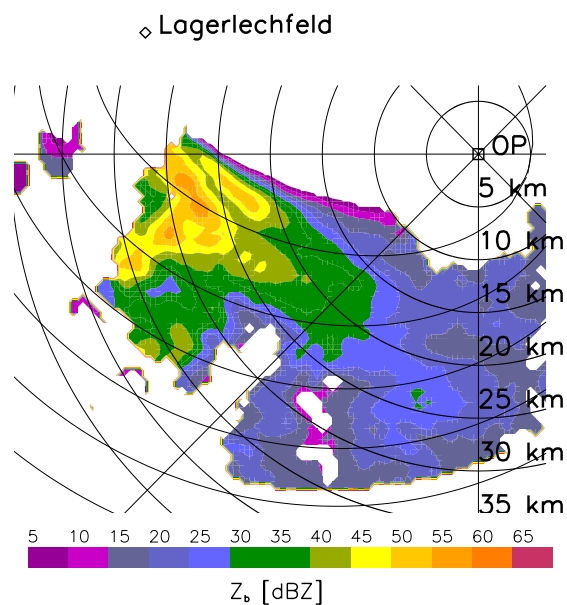


Figure 6.7: Horizontal cross-section of the bistatic reflectivity factor field in dBZ measured by the bistatic receiver Lagerlechfeld at 1455 UTC at a height of 1.8 km above MSL. Spheres and ellipsoids of constant delay are indicated.

receivers in the area where both unit vectors, \mathbf{e} , \mathbf{t} , were pointing in the same direction ($\gamma \leq 10^\circ$) showed differences of less than about $\pm 0.5 \text{ m s}^{-1}$. These values were of the same order of magnitude as the accuracy of the Doppler velocity measurement.

The wind-field retrieval was performed in a $40 \text{ km} \times 40 \text{ km} \times 10 \text{ km}$ domain and interpolated onto a Cartesian grid with a horizontal and vertical resolution of 500 m. The retrieval domain consisted of 20 height levels, beginning at 600 m above MSL and reaching up to a height of 10.6 km above MSL. Interpolation to a reference time was applied. The vertical velocity was retrieved by the scheme that minimizes the up- and downward integration (FUDI). Owing to the high variability in wind direction and speed, the weights for the quality index related to $F(\sigma'_{|\mathbf{v}_h|}/|\mathbf{V}_h|)$ were set to zero. Furthermore, the probability of sidelobe contamination was investigated separately. Therefore only data with a scattering angle limit, γ , varying between 50° and 140° were considered in this case study.

6.3.2 Assessment and discussion

The temporal development of the convective system is shown in the horizontal wind-vector underlaid by the vertical velocity for the earlier state (1401 UTC – 1422 UTC) and for the full development of the convection (1445 UTC – 1505 UTC). Figure 6.8 shows the retrieved vertical velocity field superimposed on the horizontal wind-vectors at a height of 1.8 km above MSL for the earlier states and at 3.8 km above MSL for the later states.

At ground level [Figs. 6.8(a) – 6.8(c)], strong convergence was observed with an inflow from the north into the northern part of the storm and from the south into the southern part of the storm. The horizontal convergence increased with time. The northern part consisted of an alternating band of up- and downdrafts, while the southern part of the storm was dominated by subsidence.

At higher altitudes and as time progressed [cf. Fig. 6.8(d) – 6.8(f)], the direction of the inflow turned to northwest towards the main cell, while in the southern part westerly winds dominated. Up- and downdraft intensified with the temporal development in the convective system. The main cell was fully developed at 1455 UTC. It was located at $225^\circ \leq \phi_t \leq 280^\circ$ and at a range of $15 \text{ km} \leq r'_t \leq 30 \text{ km}$ with a maximum of updraft of about 8 m s^{-1} .

Figure 6.9 shows the retrieved horizontal wind-vector underlaid by the vertical velocity at 1455 UTC at a height of (a) 1.35 km, (b) 2.85 km, (c) 4.35 km and (d) 5.35 km above MSL. The horizontal wind-vector in the lower troposphere showed strong divergence and convergence with an easterly and westerly flow at 1.35 km above MSL including the existence of a cyclonic circulation at 2.85 km above MSL [Fig. 6.10(a)]. Aloft, northwesterly to westerly winds dominated [Figs. 6.9(c) and 6.9(d)], with a noticeable confluence of the outflow on the southern part of the most active part of the system [Fig. 6.10(b)]. The vertical velocity fields [cf. Figs. 6.9(a) – 6.9(d)] were characterized by a well-defined region of ascent located at $230^\circ \leq \phi_t \leq 270^\circ$ at a range of $15 \text{ km} \leq r_t \leq 25 \text{ km}$ and a downdraft area south of it. Maximum values of 6 m s^{-1} at a height of 5.35 km above MSL were reached in the updraft region and val-

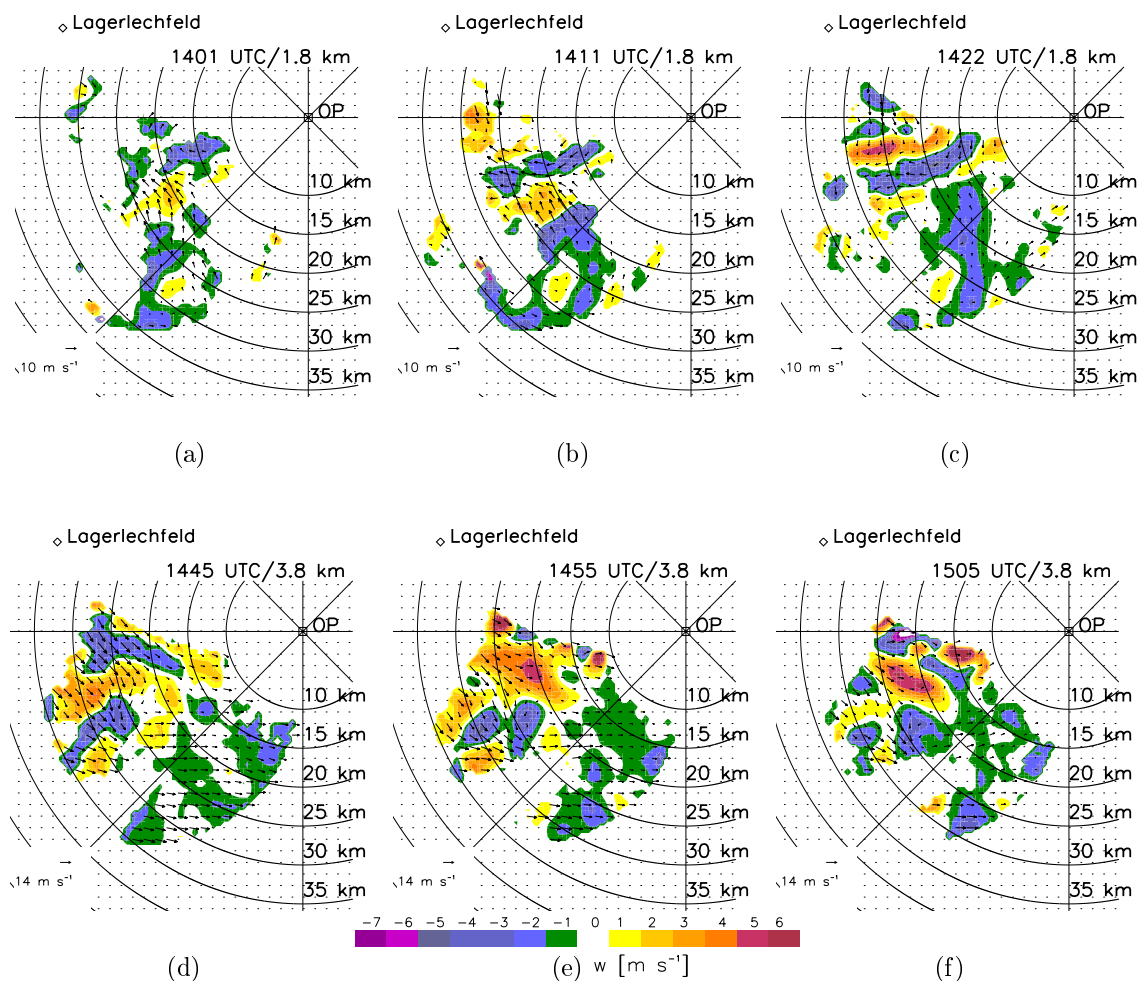


Figure 6.8: Temporal development of a convective system formed within the investigation area on 3 May 2000 between 1400 UTC and 1500 UTC as observed by POLDIRAD and receiver Lagerlechfeld. The horizontal wind-vector is underlaid by the vertical velocity in m s^{-1} (a)–(c) at a height of 1.8 km above MSL representing the earlier state and (d)–(f) at 3.8 km above MSL to show the full development. Ascent is indicated by positive values, decent by negative values. For clarity of display, only every third wind-vector is plotted.

ues of -5 m s^{-1} at 5.35 km above MSL in the southern downdraft region [Fig. 6.9(d)]. Both positive and negative values of horizontal divergence were observed in the main updraft area [Fig. 6.10(b)].

Isotachs of the vertical velocity underlaid by the reflectivity factor measured by POLDIRAD are shown in Fig. 6.11. Here, a east–west vertical cross-section is shown through the downdraft region 13 km south of OP, while another one is through the region with the main updraft (5 km south of OP). In Fig. 6.11(a), the maximum downdraft was found at high altitudes (1.85 km and 2.85 km above MSL). The updraft

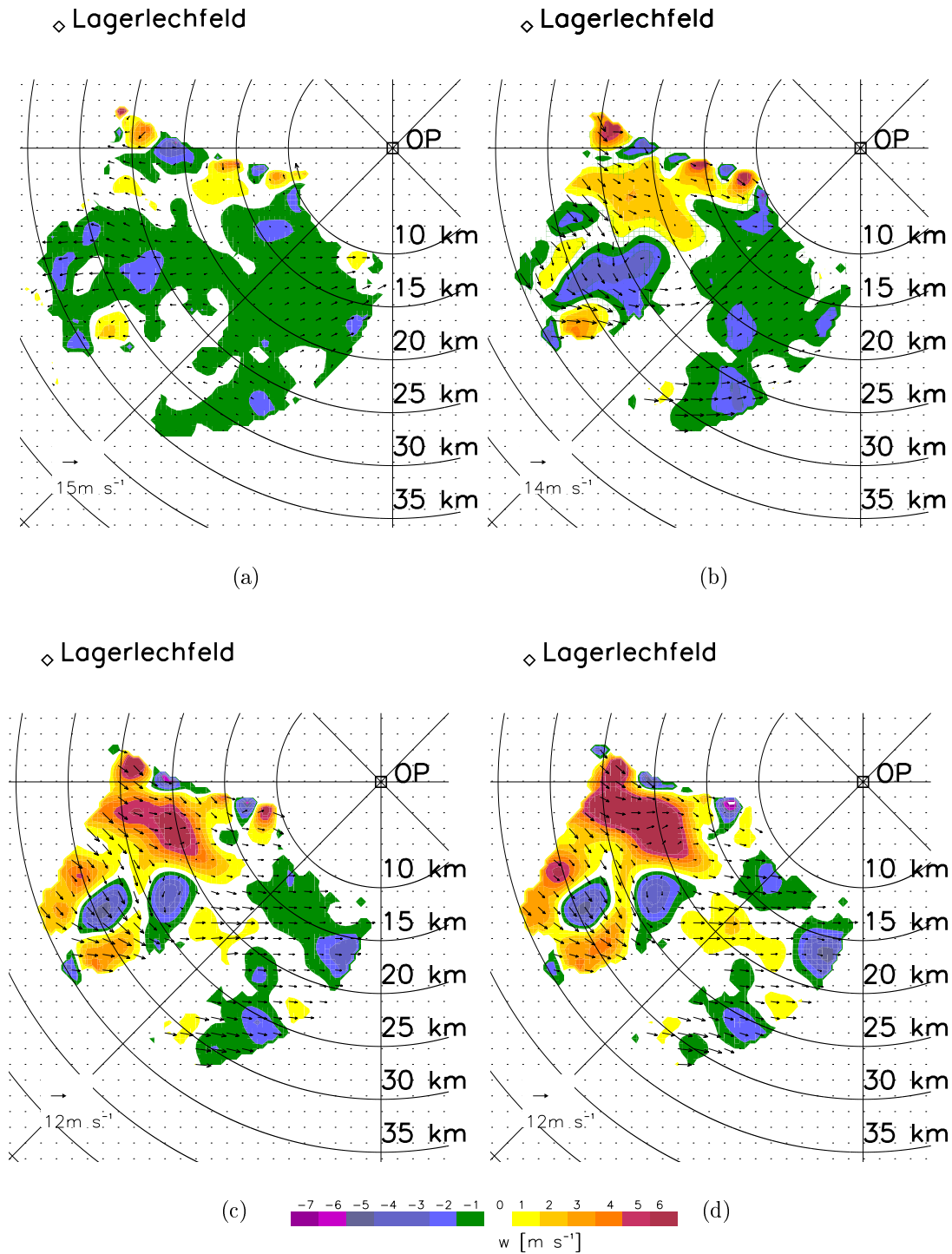


Figure 6.9: Horizontal cross-section of the horizontal wind-vector in m s^{-1} at a height of (a) 1.35 km, (b) 2.85 km, (c) 4.35 km, and (d) 5.35 km above MSL underlaid by the vertical velocity in m s^{-1} for 3 May 2000, at 1455 UTC. The horizontal wind was determined by the Doppler measurements of the receivers Oberpfaffenhofen and Lagerlechfeld. Ascent is indicated by positive values, while negative values indicate descent. For clarity of display, only every third wind-vector is plotted.

core was linked to the maximum of reflectivity factor. The successive changes between updraft and downdraft can be forced by the downward pressure perturbation force found on either side of a buoyant element (Houze, 1993). As shown in Fig. 6.11(b), the updraft increases with height up to values of 8 m s^{-1} to 10 m s^{-1} . Beside the upper-level downdraft at 10 km west of OP, no downdraft appeared in this cross-section.

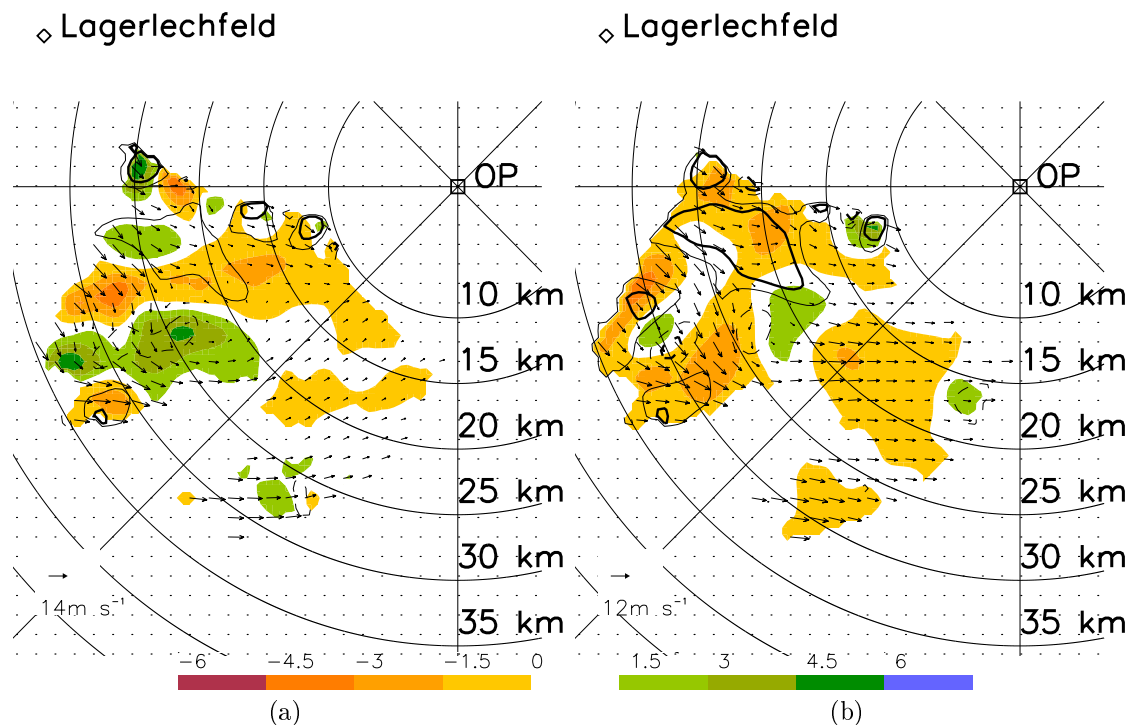


Figure 6.10: Horizontal cross-section of the (a) relative vorticity [10^{-3} s^{-1}] at 2.85 km above MSL and (b) divergence [10^{-3} s^{-1}] at 4.35 km above MSL for 3 May 2000, 1455 UTC. The horizontal wind-vectors (arrows) and the vertical velocities (lines) in m s^{-1} are superimposed. Updraft is indicated by solid lines while downdraft by dashed lines every 2 m s^{-1} . Thick lines indicate the velocity value of ± 2 , ± 4 , respectively.

6.4 Wind-fields within non-precipitating situations: 18 August 1998

On 18 August 1998, subtropical warm air with maximum temperatures around 30° C were dominant over southern Germany. Radar measurements showed clear-air echos with reflectivity factors around 0 dBZ. The wind-velocities were very weak and uniform having values of about 2 m s^{-1} - 3 m s^{-1} at ground level and of about 3 m s^{-1} - 5 m s^{-1} at a height of 1 km. The horizontal wind varied between easterly and south-easterly directions.

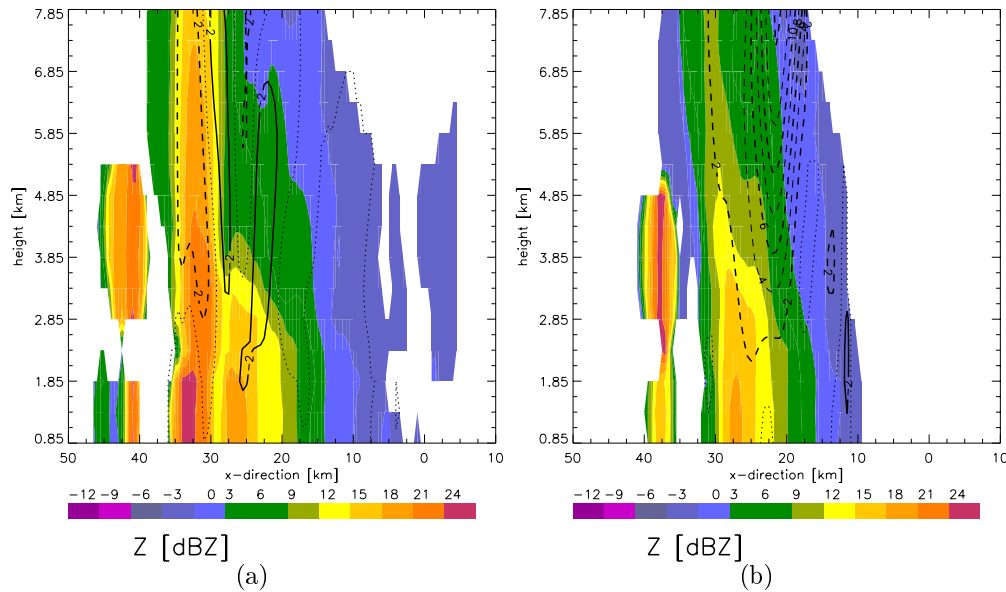


Figure 6.11: Vertical cross-section from the west to the east through (a) the downdraft region 13 km south of OP and (b) the updraft region 5 km south of OP on 3 May 2000, at 1455 UTC. Isotachs of the vertical velocity in m s^{-1} are underlaid by the reflectivity factor, measured by POLDIRAD, in dBZ. Solid lines indicate downdraft and dashed lines updraft. The zero isotach is indicated by the dotted line.

During this clear-air situation, Doppler velocities close to Lichtenau were observed. Data was sampled by the receiver Oberpfaffenhofen and Lichtenau over an area of about $12 \text{ km} \times 8 \text{ km} \times 2 \text{ km}$. At that time, the bistatic antenna at the receiver Lichtenau with a vertical aperture of 8° faced eastwards. Due to the high relative error at low wind-velocities and the small amount of data, the interpolation onto the Cartesian grid and the wind retrieval were not performed. The main focus of this case study is to show that horizontal wind-fields are also measurable by a bistatic receiver even within non-precipitating air.

Volume scans were performed every 15 minutes with vertical elevations of 1° – 4° and 6° by POLDIRAD. Figure 6.12 exhibits the horizontal wind-vector underlaid by the power field measured by the bistatic receiver Lichtenau at 1° elevation and 3° elevation. The influence of ground friction within the boundary-layer can be seen at 1° elevation indicated by southeasterly winds having values of about 2 m s^{-1} , and at 3° elevation indicated by values of 3 m s^{-1} – 5 m s^{-1} with easterly flow. With increasing height, the wind speed increased from 2 m s^{-1} – 3 m s^{-1} to 3 m s^{-1} – 5 m s^{-1} , while the direction changed from 40° – 60° to about 90° .

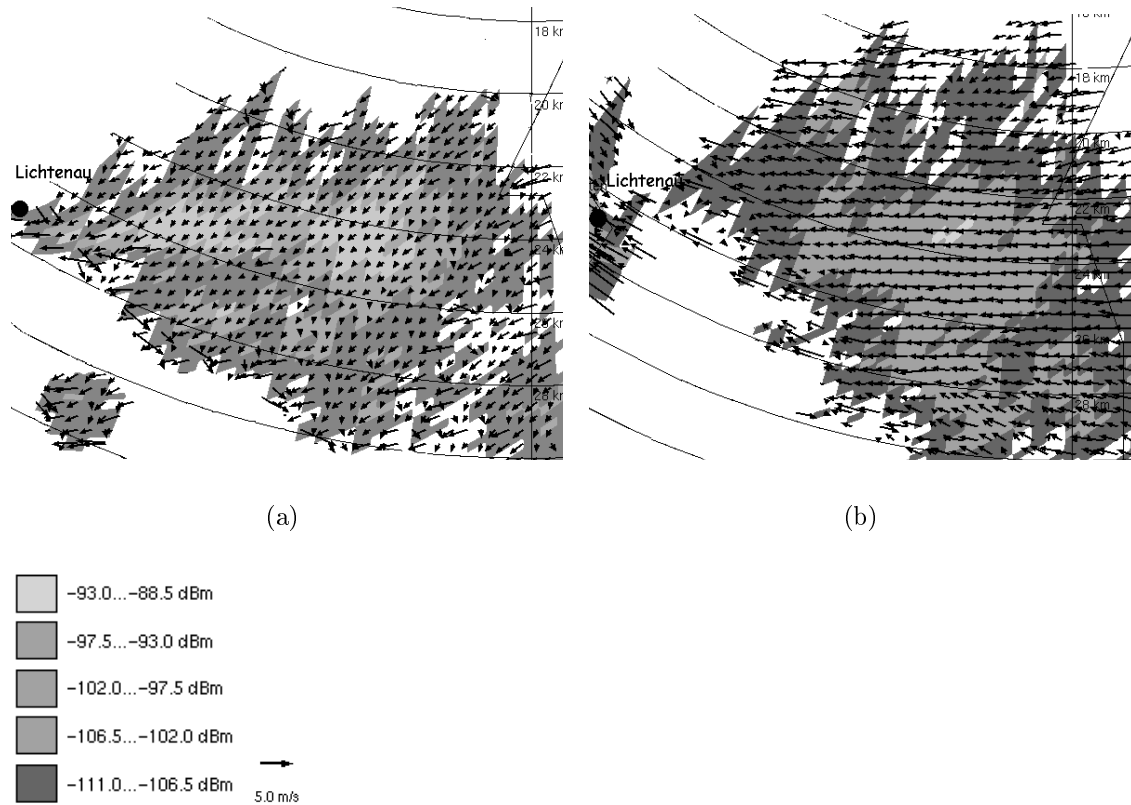


Figure 6.12: PPI of the horizontal wind-vector in m s^{-1} underlaid by the power field in dBm measured by the receiver Lichtenau during a clear-air situation on 18 August 1998 at 1055 UTC at (a) 1° elevation and (b) 3° elevation. The horizontal wind-field was determined by the Doppler velocity measurements achieved by receivers Oberpfaffenhofen and Lichtenau. The range rings are centered at Oberpfaffenhofen.

6.5 Assessment and discussion

One of the aims of this work was to show that all three wind-components could be determined for different weather situations. This was achieved by showing the performance of data-processing, wind synthesis, quality control, and wind retrieval for stratiform precipitation during a frontal passage, for convective precipitation, and within a clear-air situation.

Data-processing (Sec. 4.1) included dealiasing of Doppler velocities (necessary only for data measured on 10 April 2001), interpolation onto a Cartesian grid, and to a reference time (applied to data measured on 2 February 2000, 10 April 2001, 3 May 2000).

Wind synthesis (Sec. 4.2) was applied to the measurements obtained during all four cases. All four algorithms (Sec. 4.3, Sec. 4.4.1 – Sec. 4.4.3) of the quality-control scheme were applied to the data measured during stratiform and convective precipitation. However, the comprehensiveness and the emphasis to the quality-control scheme varied according to the weather situations.

During the stratiform precipitation event, for instance, the average quality-index field was determined according to Eq. (4.9) setting all weights to one. In this case, the quality of horizontal wind is dominated by the accuracy of σ_{v_e} and $\sigma'_{|\mathbf{v}_h|}$, which are both fixed for an experimental setup. A separate investigation on sidelobe contamination was not performed, because of the low values of $F(\nabla Z)$.

The emphasis on the quality control was set differently by the convective case. For instance, $F(\sigma'_{|\mathbf{v}_h|}/|\mathbf{V}_h|)$ could not be applied owing to the high wind-shear. On the other hand, the control for data consistency, such as the persistence check in time and space and investigation on sidelobe contamination, was more important.

The cases discussed here show clearly that quality-control algorithms must be flexibly and separately applicable.

For the stratiform and convective cases, all three wind-components were retrieved using the constraining model and the integration scheme FUDO. Clear meteorological structures in the vertical velocity were visible. The overall structure of the vertical motion according to the frontal passage and the development of convective cells could be verified.

Although the specific case studies could be validated only by ground-based observations and reflectivity data, the estimated wind-vector field represented significant characteristics of the respective weather situations.

As a result, the wind-vector fields measured by the bistatic Doppler radar network or retrieved by the constraining model are utilizable for meteorological purpose such as regional surveillance application, hazard warning, nowcasting of weather phenomena, or assimilation into numerical weather prediction models. They are available either quality-controlled by the decision procedure (Sec. 4.2, Sec. 4.4) or together with the averaged quality-index field (Sec. 4.3).

Further case studies have to show how data-processing, wind-synthesis, quality control, and wind retrieval have to be applied for operational usage.

7 Evaluation of horizontal wind-fields

7.1 Intercomparison to monostatic Doppler radar measurements

A reliable evaluation of horizontal wind-fields can only be achieved with an independent monostatic Doppler radar system. Advantages using monostatic Doppler radar systems for evaluating bistatic Doppler radar measurements arise from their ability to sample both data in time and space with a resolution of a hundred meters and to measure wind-fields during the same weather conditions. However, these advantages are not necessarily given when comparing radar data with point measurements (e.g. in-situ flight measurements, radiosoundings) or with spatially covered measurements (e.g. lidar observations).

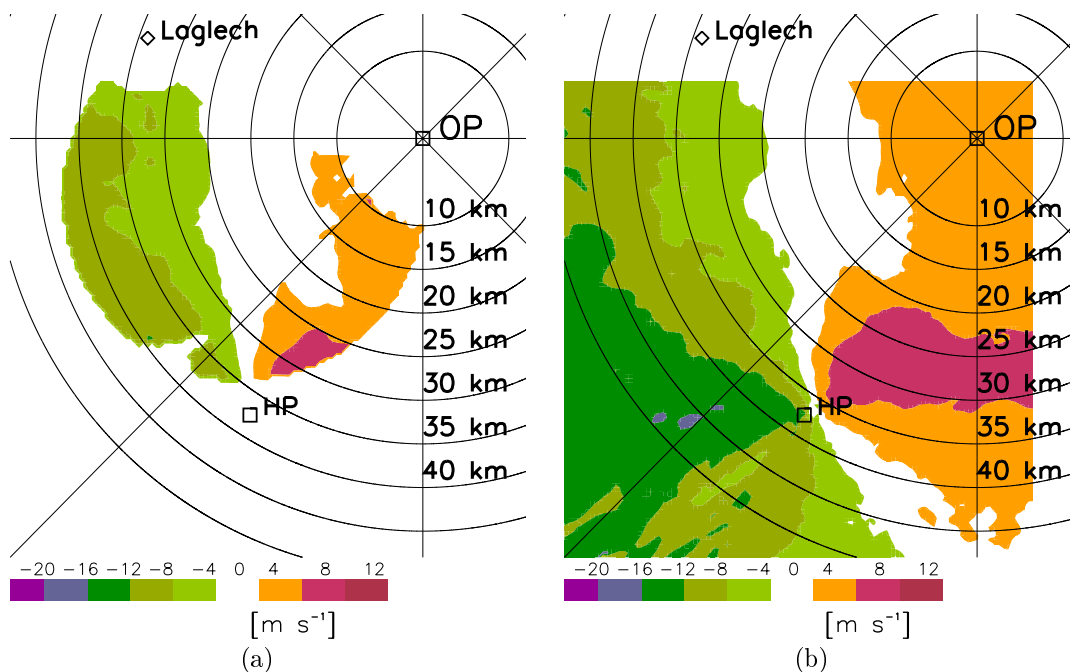


Figure 7.1: Horizontal cross-section of (a) the reconstructed radial velocity in m s^{-1} and (b) the radial velocity measured by the monostatic radar Hohenpeißenberg (denoted as HP) during stratiform precipitation on 10 April 2001 at 1300 UTC. The reconstructed radial velocity was achieved by calculating the radial component from the horizontal wind-vector at 1.6 km above MSL. The horizontal wind-vector was estimated from measurements taken by receivers POLDIRAD and Lagerlechfeld (Laglech).

To illustrate the superior reliability of bistatic Doppler radar measurements, this intercomparison was performed for a weather situation with low wind-shear. On 10 April 2001, between 1200 UTC and 1530 UTC, stratiform precipitation was present within the observation area²⁴. The wind came mainly from the southwest, with

²⁴Note that this case was discussed in detail in Sec. 6.2.1.

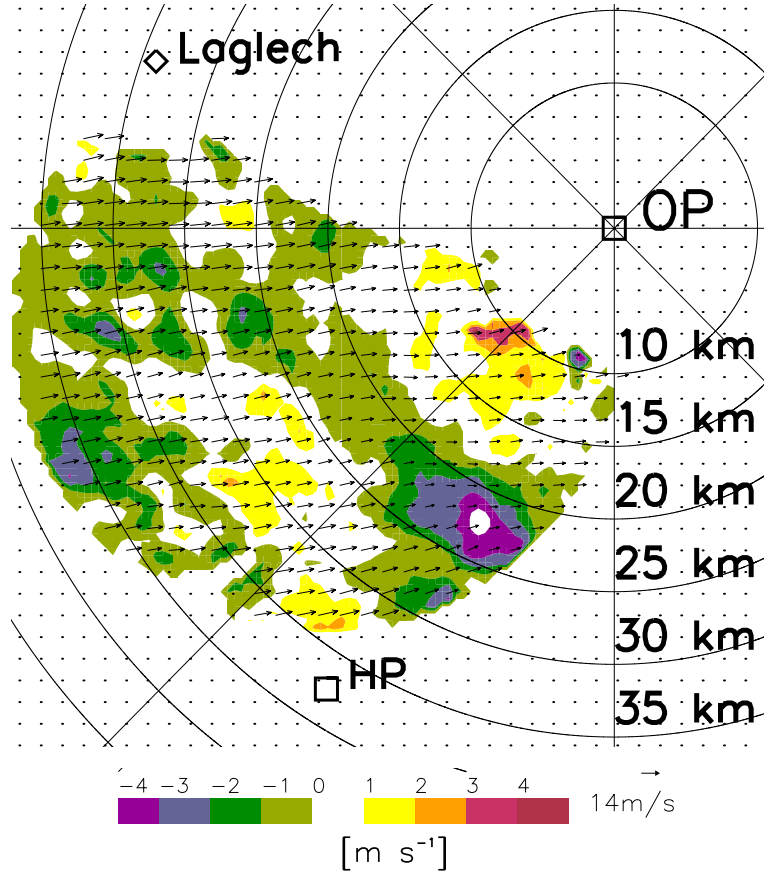


Figure 7.2: Horizontal cross-section of the difference between measured and reconstructed radial velocity (m s^{-1}) related to the monostatic Doppler radar HP. Doppler velocities were observed during a case of stratiform precipitation on 10 April 2001 at 1300 UTC. Horizontal wind vectors measured by the bistatic Doppler radar are overlaid for the respective time and height. For clarity of display, only every third wind-vector is plotted. Within the white marked core at $\phi_t = 210^\circ$ and 215° , $r'_t = 20 \text{ km} - 25 \text{ km}$, the differences exceed the value of -4 m s^{-1} .

velocities ranging between 10 m s^{-1} to 14 m s^{-1} . A wind-velocity gradient in an east-west direction over a length of 30 km occurred having values of 14 m s^{-1} in the west and 6 m s^{-1} east of the observation area. The mean wind direction was about 260° , varying from $240^\circ - 265^\circ$.

First, the horizontal wind-field was determined from the Doppler velocities measured by the receivers Lagerlechfeld and POLDIRAD. From this wind-vector, the radial wind component as measured by the independent monostatic Doppler radar HP, \tilde{v}_{tHP} , was reconstructed according to Eq. (2.3). Figure 7.1(a) illustrates a horizontal cross-section of \tilde{v}_{tHP} at a height of 1.6 km above MSL. The reconstructed radial velocities were then compared to those velocities measured by the monostatic Doppler radar at HP [Fig. 7.1(b)]. The differences between the reconstructed and the observed radial velocities, illustrated in Figure 7.2 (color-coded), were mainly in

the same order of magnitude as the accuracy of the wind-field measurements ranging between about $\pm 1.5 \text{ m s}^{-1}$. Larger differences were observed at $\phi_t = 200^\circ - 220^\circ$ at a distance between 20 km and 25 km (Fig. 7.2). In the reconstructed radial velocities displayed in Fig. 7.1(a), the zero-velocity isoline formed a bulge between $\phi_t = 210^\circ - 225^\circ$ and at a range of 15 km to 25 km. On the other hand, this bulge was less pronounced by the radial velocity measurements taken by radar HP [Fig. 7.1(b)]. In this area, higher radial velocities with values of 4 m s^{-1} to 8 m s^{-1} were measured by the radar HP. One reason for the great differences can be the time delay of four minutes between the radial velocity measurements taken by HP and the measurements obtained by the bistatic multiple-Doppler radar network. Similar differences were observed at various other heights.

Summarizing, beside the area SSW of OP, the differences in radial velocity were about 1 m s^{-1} to 2 m s^{-1} at all levels. The bistatic multiple-Doppler radar network achieved mainly realistic results in this stratiform precipitation case.

Beside the influence of instrumentation specifications (e.g. data-processing) and meteorological parameters (e.g. high degree of turbulence within the resolution volume) on the quality of the wind-field, interpolating data onto a Cartesian grid and to a reference time can also modify the wind-field. While this impact is relatively low in the case of stratiform precipitation, it can be critical in weather situations when there is a high wind-speed or a fast developing precipitation system.

The comparison of Doppler velocity measurements to external observational data can also be used to indicate regions where the Doppler velocities (measured by bistatic receivers) are contaminated by sidelobes of the transmitting power pattern. A comparison will show the contaminated areas directly, because the Doppler velocity measured by a monostatic radar is less susceptible to sidelobe effects (cf. Sec 2.5). It would be premature at this time to make a statement about the reliability of the bistatic wind-field measurement, until further comparisons have been accomplished, especially during weather situations having a high wind shear.

7.2 Intercomparison to in-situ flight measurements

Evaluating spatially high-resolution horizontal wind-fields with point measurements is less meaningful when compared to those achieved with a monostatic Doppler radar system. But the in-situ flight measurements taken on 11 April 2001 can be used as an additional independent measurement to evaluate horizontal wind-fields determined by the bistatic Doppler radar network.

The in-situ measurements were performed with the DLR research aircraft, Falcon. The wind-speed at the position of the aircraft, measured by a five-hole gust probe on the tip of the nose boom, is derived from the differential and the static pressure at the five holes of the half-spherical probe tip. The wind components, u, v, w , in an earth-fixed coordinate system, can be derived from the differences between the airflow at the probe, velocity of the aircraft, and orientation of the sensor relative to the ground, which is given by an internal reference system (IRS). The absolute accuracy of the mean horizontal components is $\pm 1 \text{ m s}^{-1}$ (for more detail, see Boegel

& Baumann (1991); Quante et al. (1996)).

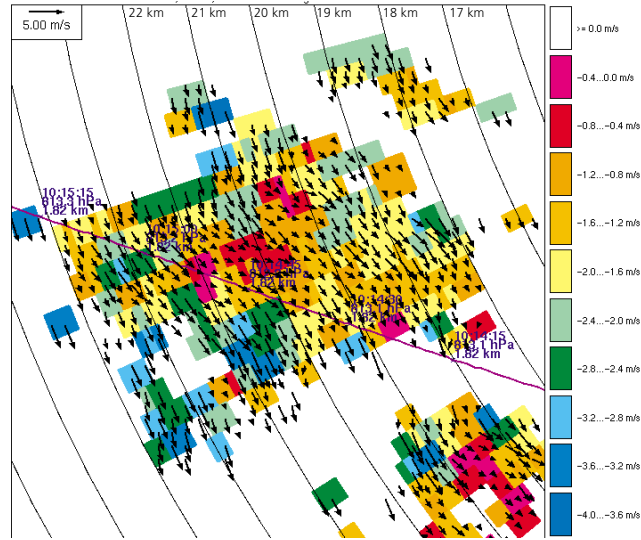
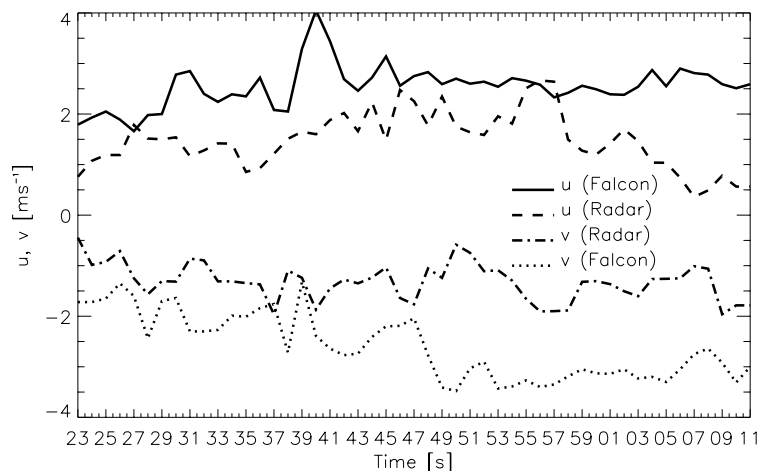


Figure 7.3: PPI of the south-wind component in m s^{-1} (color-coded) at 4° elevation taken on 11 April 2001 between 10:13:09 UTC and 10:13:11 UTC, overlaid by the flight path of the aircraft (red line) and the horizontal wind-vector field (arrows). The labels on the flight path indicate the UTC time (HH:MM:SS), pressure in hPa, and altitude above MSL in km. The horizontal wind-vectors, \mathbf{V}_h , were determined from the Doppler velocities measured by the receivers POLDIRAD, Lichtenau, and Lagerlechfeld.

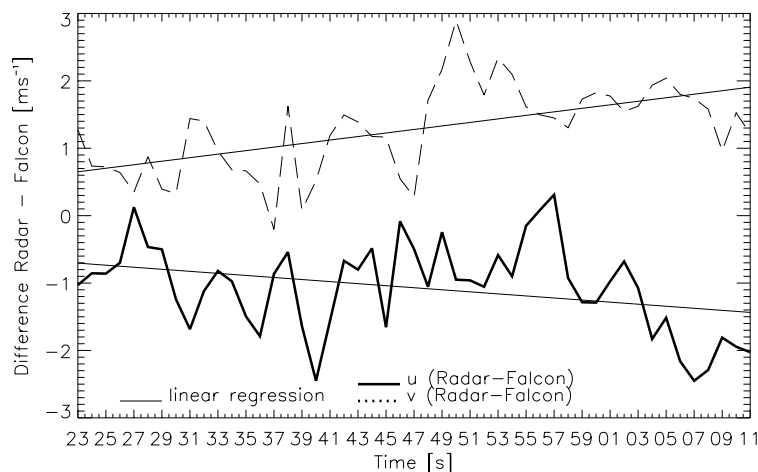
The aircraft passed the investigation area flying between 10:14:15 – 10:15:15 UTC from the southeast to the northwest at an altitude of 1.8 km above MSL. Fig. 7.3 exhibits the flight path through the investigation area. The respective elements of UTC time, pressure, and altitude are labeled. The sensor signals were recorded with 100 Hz corresponding to a sampling interval of typically 1.5 m. The measured data was averaged to an interval of 1 s, which represents a length of about 150 m, assuming the aircraft speed to be about 300 kt.

In-situ flight measurements of u, v were compared to the velocity components determined by the bistatic multiple-Doppler radar network at 2° elevation (sampled between 10:12:29 UTC and 10:12:32 UTC) and at 4° elevation (10:13:09 UTC and 10:13:11 UTC). The horizontal wind-vector, \mathbf{V}_h , was estimated in spherical coordinates at 2° and 4° elevation from the Doppler velocities measured by receivers POLDIRAD, Lichtenau, and Lagerlechfeld. The horizontal wind-vector field at 4° elevation underlaid by its south-wind component of each sample volume is illustrated in Fig. 7.3.

At 2° elevation, the observation height varied between 1.30 km above MSL (at $r_t = 19$ km) and 1.44 km above MSL (at $r_t = 24$ km). While at 4° elevation it ranged between 2.0 km (at $r_t = 19$ km) and 2.3 km above MSL (at $r_t = 24$ km). The flight path was located at a height of 1.8 km above MSL. The west- and south-wind components, measured by the radar at each aircraft sample point, were averaged vertically. At a distance of 20 km from the radar, the sample volume of the monostatic



(a)



(b)

Figure 7.4: (a) The values of u, v and (b) its differences in ms^{-1} achieved during in-situ flight measurements (denoted as Falcon) and measured by the bistatic Doppler radar (denoted as Radar) along the flight path for a stratiform precipitation case on 11 April 2001. The aircraft passed the observation area between 10:14:23 UTC and 10:15:11 UTC. For the west-wind component, the linear regression line is given by $y = -0.015x + 0.68$, while for the south-wind-component it is $y = 0.026x + 0.65$.

radar had a diameter of about 300 m and a length of 150 m (with a 1° antenna beam-width and a $1\text{-}\mu\text{s}$ pulse length). Therefore, the spatial resolution of the aircraft measurements was higher than this achieved by the radar. An interpolation in time of both data sets was not performed due to a lack of synchronization between time measurements in the aircraft and at the radar. Furthermore, coupled GPS and IRS

measurements achieved the positioning of the aircraft with an error ranging from 100 m to 200 m per two to three minutes. The error results mainly from the IRS measurements.

Figure 7.4(a) illustrates time series of the west- and south-wind components when measured by the bistatic Doppler radar network and by the in-situ flight measurements. The differences of u, v between the radar and in-situ measurements are presented in Fig. 7.4(b). The difference of u, v ranged mainly between $\pm 2 \text{ m s}^{-1}$. The horizontal wind-components measured by the aircraft were mostly 1 m s^{-1} to 2 m s^{-1} higher than the radar measurements, even though the Doppler velocities were sampled at a higher elevation, e.g. only considering data measured at an elevation of 4° (not explicitly shown). The observed differences between radar and the in-situ measurements were slightly wider than the degree of the accuracy in the wind-field measurements. These differences in the horizontal wind-field components can be related mainly to the low values of u, v when compared to the absolute error of the velocity measurement. Due to a low temporal evolution of this system, having weak precipitation and low wind-velocity, the impact of the temporal displacement between the aircraft and radar measurements can be neglected.

For a broader evaluation, flight measurements have to be obtained over a longer time period, a larger spatial coverage, and in weather situations, for example with higher wind-shear or with higher wind velocities.

8 Future applications

8.1 Wind–vector fields throughout Germany

A knowledge of the wind–vector field is essential to the understanding of weather phenomena. With a bistatic Doppler radar, wind–vector fields can be sampled in time and space within precipitating clouds, but also within certain clear–air situations. This information can be used operationally in real–time to give warnings of severe weather or for nowcasting of weather events. Together with reflectivity and radial velocity data measured by the monostatic radar, horizontal wind–vectors can be assimilated operationally into numerical weather prediction (NWP) models in order to adjust the model initial state more realistically to the meteorological situation (for more details, see Sec. 8.3).

The German Weather Service (DWD) has built up a radar network consisting of 16 C–band weather radar systems covering an area with an average radius of 240 km. Reflectivity and, in some cases, Doppler velocity and spectral width are sampled operationally every 15 minutes. For a wider spatial coverage, the network can be extended by the Doppler radar system located at the observatory Hohenpeißenberg and by the radar operated by the Forschungszentrum Karlsruhe.

If each monostatic radar system were equipped with three bistatic receivers, horizontal wind–vector fields could be estimated for large parts of Germany, as illustrated in Fig. 8.1. Gray circles having a radius of about 50 km indicate the areas where horizontal wind–vector fields could be estimated using a bistatic radar network. Those weather radars within the network which cannot measure the phase of the transmitted and received wave need not be replaced to have bistatic receivers installed. They need only to be altered for purposes of measuring the phase of the transmitted wave. Weather radar systems without polarization diversity transmit a horizontally–polarized wave. For wind–vector field determination using bistatic receivers, the monostatic transmitting radar system has to be reconstructed to be able to transmit a vertically–polarized wave (cf. Sec. 2.3).

Three bistatic receivers grouped around one monostatic radar give optimal usage when considering a minimum number of receivers to achieve a maximum spatial coverage in horizontal wind–field estimation.

Within this configuration, the horizontal wind–vector fields can be determined within a radius of about 50 km around the transmitting radar, as illustrated in Fig. 8.2(a). The area is restricted by a scattering–angle limit of 50° to 140° (gray–marked area). The horizontal wind–vector fields are processed with a dual–Doppler analysis with an absolute accuracy of the horizontal wind within the range of 2 to 3 m s^{-1} .

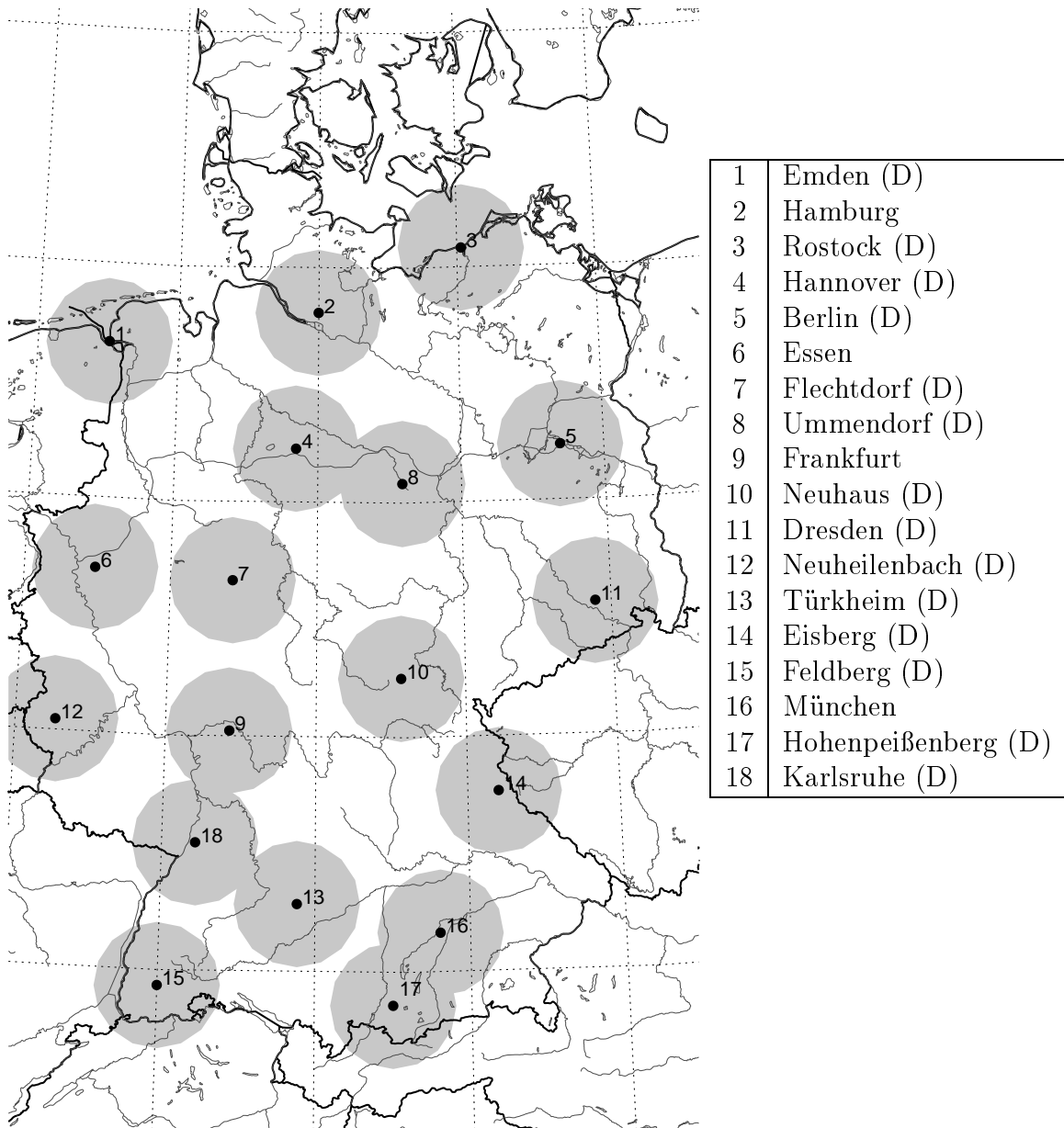


Figure 8.1: Map of the coverage of horizontal wind-vector fields throughout Germany. Each operationally working radar system is equipped with three bistatic receivers. An area with a radius of about 50 km can be covered by measurements of the horizontal wind-vector field. Radar systems with Doppler capability are signified by (D).

The accuracy of the horizontal wind retrieval can be increased to values ranging between $1.5 - 2 \text{ ms}^{-1}$ if an additional antenna is installed at each bistatic receiver site, as demonstrated in Fig. 8.2 (b). Both antennas sharing one bistatic receiver can be automatically selected according to the azimuth angle of the transmitting radar beam. Each antenna has to be positioned to cover the scattering-angle limit of 25° to 70° on both sides of the transmitter-receiver-baseline. A scattering-angle

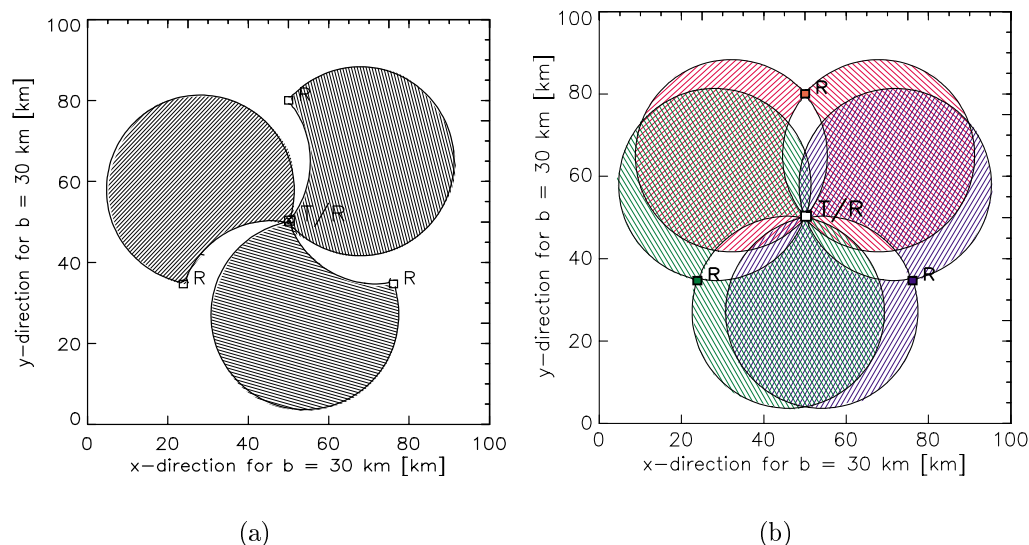


Figure 8.2: The horizontal coverage of a dual-Doppler or (b) dual-/triple-Doppler (hatched/cross-hatched area) processed horizontal wind-field. This estimation is limited for both applications by a scattering-angle limit of 50° to 140° . Each receiver is equipped with two antennas (color-coded according to the bistatic receiver).

limit of 50° to 140° is indicated. With this configuration, wind measurements along the transmitter-receiver baseline can be guaranteed through measurements taken by the two neighboring receivers. Moreover, the equation system to determine the horizontal wind-field components is overdetermined in the cross-hatched areas and exactly determined in the hatched areas. Within the overlapping areas, the entire quality-control scheme can be applied, including the algorithm dealing with irregularities during measurement, e.g. sidelobe contamination and synchronization problems between transmitter and receiver.

8.2 Wind-vector fields in the vicinity of airports

To avoid aviation accidents, severe weather-warning systems and nowcasting of weather events are especially important in the vicinity of airports and especially during holding patterns. Identification and analysis of severe weather can be supported with the knowledge of temporally and spatially high-resolution wind-vector fields. With a real-time display of the horizontal wind-field, warnings of severe weather, e.g., wind shear, can be given immediately after the signal is received. Furthermore, the processed wind-vector field in the vicinity of airports can be assimilated into high-resolution regional NWP models to improve weather forecasting around airports.

Figure 8.3 shows a possible configuration of four bistatic receivers installed around the weather radar located at Frankfurt Main Airport. In this study, each bistatic

receiver is equipped with two antennas, each covering a side of the baseline. One advantage of installing four receivers is to increase the accuracy of the horizontal wind–field determination arising from the overdetermination of the equation system used for the wind–field calculation. A second advantage is that, the area between the transmitter and receiver baseline plus the area beyond the bistatic receiver is always covered by one of the other receivers. For a configuration with four bistatic receivers, the spatial distribution of standard deviation in the horizontal wind–field, $\sigma'_{|\mathbf{V}_h|}$, is illustrated Fig. 8.3(a). Assuming a standard deviation of 1 m s^{-1} for the radial velocity measurement, the horizontal wind can be derived in the vicinity of the airport with an accuracy of $1.4 - 2 \text{ m s}^{-1}$ over an area of about $60 \text{ km} \times 60 \text{ km}$ [Fig. 8.3(a)]. The spatial distribution of the minimum detectable reflectivity factor, $Z_{b_{\min}}$, (cf. Sec. 2.4.1) is shown in Fig. 8.3(b). The spatial distribution of $Z_{b_{\min}}$ for configuration of four receivers, in Fig. 8.3(b) indicates that wind–fields can indeed be observed when the reflectivity values are larger than -5 dBZ close to the receiver and larger than 5 dBZ in an area within a radius of about 30 km around the transmitting radar. As a result measurements can be obtained, for instance, in the presence of light rain, stratiform and convective precipitation, and in some clear–air situations.

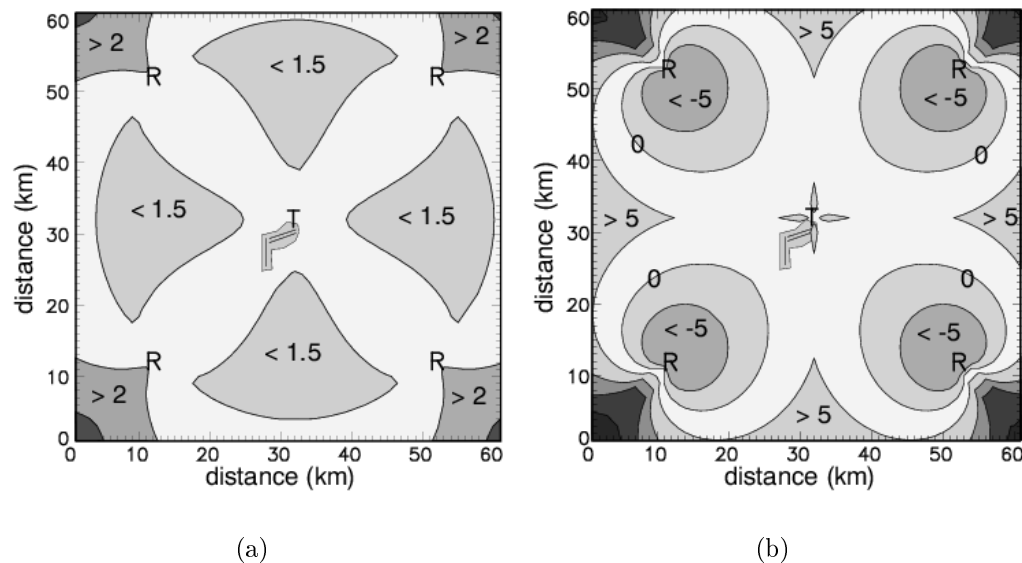


Figure 8.3: Spatial distribution of (a) $\sigma'_{|\mathbf{V}_h|}$ in m s^{-1} and (b) $Z_{b_{\min}}$ in dBZ at ground level for an installation of four bistatic receivers grouped around the transmitting weather radar at Frankfurt Main Airport. The lines close to the monostatic radar mark the two parallel runways $20^\circ / 200^\circ$, and the runway $180^\circ / 360^\circ$ at the airport.

8.3 Assimilation of wind–vector fields

Observations assimilated into numerical models are used to adjust the model initial state more realistically to the meteorological situation at the time of the observation.

A great variety of observations can be assimilated (e.g. temperature and humidity profiles, cloud height, cloud classification, wind, precipitation data) which are measured by different instruments (e.g. radar, lidar, satellite, mesonet station, radiosonde). The use of radar observations in hydrological and NWP models is a topic for the European COST²⁵ action 717 (Rossa, 2000).

Radial-velocity data has been assimilated into the HIRLAM (High-resolution limited-area model) forecasting system using different assimilation schemes. Vertical profiles of the horizontal wind are presently being assimilated into an operational mesoscale assimilation and forecasting system at the UK Met. Office (see Lindskog et al. (2002), personal communication with Bruce McPherson).

Before starting data assimilation, the requirements of the spatial and temporal resolution and the accuracy on radar observations have to be defined. The capabilities and the limitations of weather radar systems and bistatic radar systems have to be analyzed. Meischner et al. (1997), Serafin & Wilson (2000), Fulton et al. (1998), and Alberoni et al. (2002) give an overview of the capabilities and limitations of operational weather radar systems and processing techniques. Section 2 investigates the spatial resolution and accuracy of Doppler velocities when measured by a bistatic radar system. Section 4 presents a scheme to process Doppler velocities which also includes a quality-control scheme.

Furthermore, it is important to identify which meteorological phenomena are of interest for a particular application and which can be resolved by a numerical model. For instance, the bistatic radar resolves the wind-field with a length of resolution volume of 200 m to 500 m, thereby taking into account structures which might not be represented by a numerical model. Therefore, the question arises: how does radar data have to be processed in order to give optimal information on a weather situation which can be then handled by the numerical model?

In this section, an attempt is made to answer certain aspects of this question by comparing simulation data with radar observations achieved by the bistatic Doppler radar network at Oberpfaffenhofen. The simulations were performed by the mesoscale numerical model MM5 (Grell et al., 1994).

The monostatic Doppler radar POLDIRAD measures radial velocity and reflectivity within precipitating clouds. In addition, wind-vector fields are also available from measurements by the bistatic multiple-Doppler radar network. Vertical profiles of the horizontal wind can be obtained in both a clear- and precipitation-filled atmosphere using the VAD analysis (Lhermitte & Atlas, 1961; Browning & Wexler, 1968).

During the aircraft wake-vortex forecasting and measuring campaign WakeOP (Gerz, 2001) carried out between 29 March and 4 May 2001 in Oberpfaffenhofen, the MM5 model ran in a quasi-operational mode providing an hourly output for 24 hours in advance. At the same time, radar measurements were obtained by POLDIRAD and three bistatic receivers located at Lagerlechfeld, Lichtenau, and at the airfield at Fürstenfeldbruck.

²⁵Co-operation in the field of scientific and technical research

The observed and forecasted horizontal wind–vector fields at 0700 UTC were compared for a stratiform precipitation event on 26 April 2001. Figure 8.4 exhibits a horizontal cross–section of the horizontal wind–vector field at a height of 850 m above MSL, simulated with the MM5 model and measured by the bistatic Doppler radar network. The simulation results are underlaid by orography (shading). The retrieved vertical velocities (color–coded) are superimposed on the observed horizontal wind–vector field. Additionally, VAD scans performed over the whole day by POLDIRAD provided vertical profiles of the horizontal wind [Fig. 8.4(c)].

Both observation and forecast showed variable winds coming mainly from a westerly and southwesterly directions and having velocities ranging between about 5 m s^{-1} to 15 m s^{-1} . As a first approximation, model results [Fig. 8.4(a)] and observations [Fig. 8.4(b)] showed similar wind velocities and wind–directions.

The simulation was performed for a horizontal domain of $100 \text{ km} \times 100 \text{ km}$ having a uniform grid–interval of 2.1 km horizontally. The vertical resolution of the model varied between 20 m close to the ground and 500 m at about 5 km. The top of the domain was located at 200 mb. About 38 levels were below 4 km and 14 levels were above.

The measured Doppler velocities were processed as described in Sec. 4: Doppler velocities were dealiased according to Sec. 4.1.1. Furthermore, the observed data was interpolated onto a Cartesian grid with a uniform grid–interval of 500 m horizontally and 250 m vertically (Sec. 4.1.2). The confidence of each wind–vector was quantified using the quality–control scheme described in Sec. 4.3. The vertical velocity was retrieved using the constraining model (Sec. 5.2). The continuity equation was integrated vertically using the minimization of up– and downward integration (FUDO).

Observations and forecasts were performed on grids having different horizontal and vertical resolution. Figure 8.5 exhibits a vertical cross–section through the observation–grid of the radar data and simulation–grid of the MM5 model. The observations were interpolated onto a Cartesian grid (thick straight lines). The model results were available on terrain–following coordinates (thin lines).

The simulated horizontal wind–vectors were compared point by point to the nearest wind–vector of the measured field. No distance–weight nor averaging was applied. The distance between model and observation grid–point can reach maximal 125 m vertically and 250 m horizontally. Horizontal cross–sections of the differences in horizontal wind–speed and direction at about 850 m above MSL are given in Fig. 8.6.

Large areas were well represented by the simulation, with differences of only up to $\pm 2 \text{ m s}^{-1}$ in wind–speed and up to 10° in wind–direction. In some areas, however, the differences in wind–speed ranged between 2.5 m s^{-1} up to values of 10 m s^{-1} ; in wind–direction, differences of about 20° appeared. For instance, the area dominated by westerly winds located at $225^\circ \leq \phi_t \leq 245^\circ$ and at a range of $r'_t \approx 40 \text{ km}$ was not captured by the model and, therefore, large differences in direction and speed appear. The simulation results showed higher wind–velocities than the observations. Those

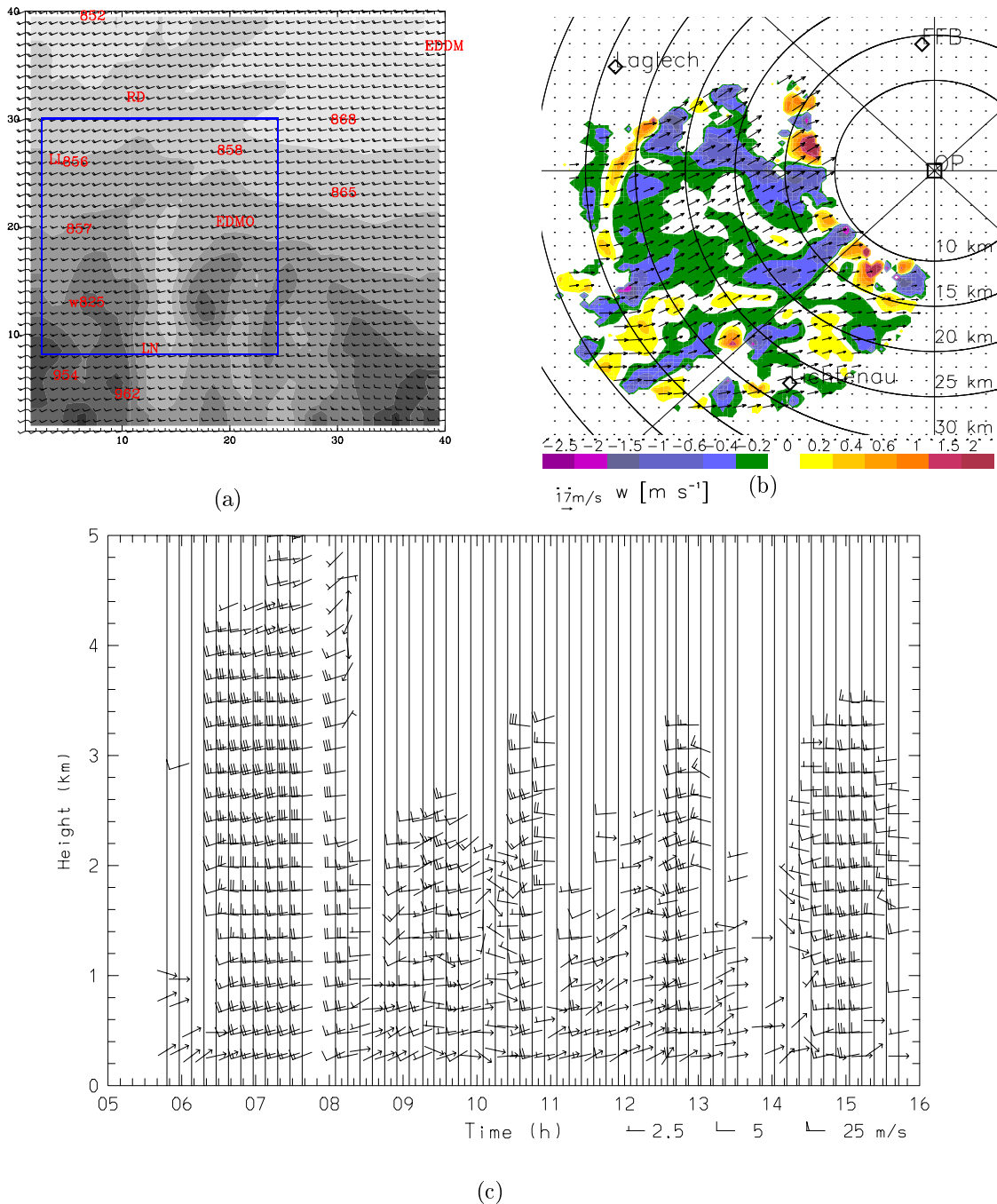


Figure 8.4: Horizontal cross-section at about 850 m above MSL of (a) the forecasted horizontal wind-vector field in kt performed with the MM5 underlaid by orography (the figure was kindly provided by Arnold Tafferer) and (b) the observed horizontal wind-vector in m s^{-1} measured by the bistatic Doppler radar network underlaid by the retrieved vertical velocity in m s^{-1} . Both simulation and observation were obtained during stratiform precipitation on 26 April 2001 at 0700 UTC. The blue box marks the observation area. The position of the receivers is denoted as LN for Lichtenau, LL for Lagerlechfeld, 858 for Fürstfeldbruck, and EDMO for Oberpfaffenhofen. Updraft is indicated by positive values, while negative values signify downdraft. For clarity of display, only every third wind-vector is plotted. (c) Vertical profile of the horizontal wind-vector taken above POLDIRAD measured between 0500 UTC – 1600 UTC by POLDIRAD (the figure was kindly provided by Martin Hagen).

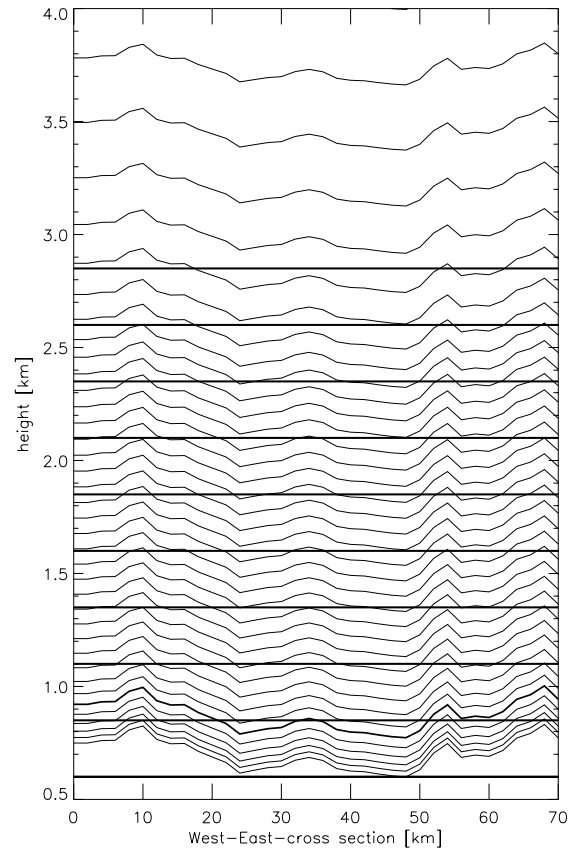


Figure 8.5: Vertical cross-section through the model and the observation domain. While the numerical model uses terrain-following coordinates (thin lines), the observational data is interpolated onto a grid with a fixed vertical spacing of 250 m, starting at a height of 600 m above MSL (straight thick lines).

differences were similar at all levels (not shown). Note that the higher-resolution observational data showed much more detail and a higher variability.

The high variability of the measured data when compared to the simulation is illustrated in the scatter diagram in Fig. 8.7. In the observations, the horizontal wind-speed varied mainly from 7 to 14 m s^{-1} and in wind-direction from 230° to 270° . The simulated wind-vector fields showed a smaller variability in wind-speed, having a range of 6 to 9 m s^{-1} and an average wind-speed of 8 m s^{-1} . The horizontal wind-direction ranged between 240° and 260° . The observed variances cannot be represented by the mesoscale model. Indeed, the scatter diagram shows little (b) to almost (a) no correlation.

In order to assimilate only those structures that can be resolved with the grid-resolution of the model (in this case $\Delta x = 2$ km), the observational data has to be interpolated onto the model grid. The original characteristics and structures of the raw wind observations have to be presented as well as possible after smoothing is applied. For instance, Albers (1995) described the box averaging methodology

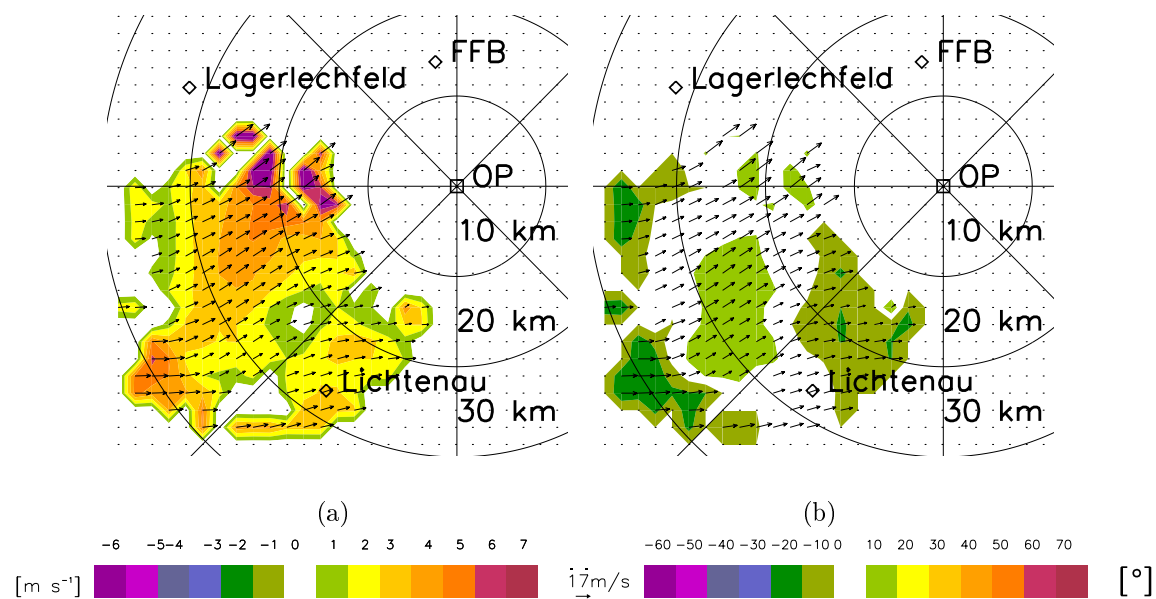


Figure 8.6: Horizontal cross-section at a height of 850 m above MSL of the difference in (a) speed [m s^{-1}] and (b) direction [$^{\circ}$] of the horizontal wind-vector field between the observation time and the 7-h forecast, during stratiform precipitation on 26 April 2001 at 0700 UTC. The horizontal wind-vector field measured by the bistatic Doppler radar network is superimposed.

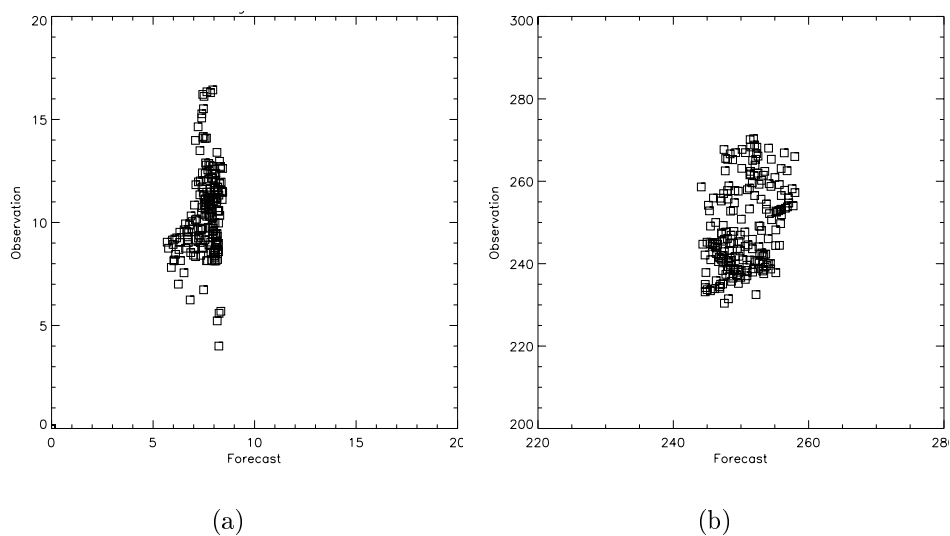


Figure 8.7: Scatter plot of observed and forecasted (a) speed in m s^{-1} and (b) direction [$^{\circ}$] of the horizontal wind-vector field at about 850 m above MSL for the stratiform precipitation case on 26 April 2001, 0700 UTC.

used for the Local Analysis and Prediction System (LAPS). Here, the radial velocity was averaged for each LAPS grid–box. For the assimilating of radial winds into the HIRLAM model, the raw volume data was averaged horizontally in polar space (Lindskog et al., 2002).

9 Summary and Conclusion

Wind–vector fields have been estimated during different weather situations using a bistatic Doppler radar network. This system is the first worldwide to operate with a magnetron transmitter, where the phase of each transmitted pulse is random and must be measured and then transferred to each bistatic receiver for data processing (cf. Sec. B). This thesis has examined procedures for determining the wind–vector field and its quality. The optimal configuration of the bistatic receivers is analyzed in order to have low spatial resolution, high accuracy, and high spatial coverage of the horizontal wind–vector field. Technological advancements of the bistatic system are discussed also.

The spatial resolution, accuracy of wind–field measurements, and the ability to detect weak signals depend largely on how the bistatic receivers are arranged. The investigation showed that, within a bistatic Doppler radar network, wind–vector fields can be most reliably determined within a scattering–angle limit of between 50° and 140° (cf. Fig. 2.14). Within this area, the spatial resolution ranges from 150 m to 700 m and the standard deviation margin varies between 2 m s^{-1} and 3 m s^{-1} . In addition, the minimum detectable reflectivity factor ranges between -5 dBZ to 10 dBZ within the area of the limited scattering–angle (all numerical values based on the DLR system). Investigations on how the transmitted wave and the receiver have to be polarized indicated that vertically transmitted and received polarization is optimal at lower altitudes. At higher altitudes (above a height of 9 km), a transmitted wave with slanted $45^\circ/135^\circ$ polarization and a receiver polarized vertically give a higher sensitivity.

In order to set up a bistatic system having the same degree of accuracy as a monostatic network, a set of bistatic receivers double in number compared to the radars in the monostatic network has to be installed [cf. Figs. 2.13(a) and 2.13(c)]. Reducing the number of receivers within this bistatic network (starting from twice the number of receivers) results in a standard deviation increase of $0.5 \text{ m s}^{-1} - 1 \text{ m s}^{-1}$ per missing receiver [cf. Figs. 2.13(a), 2.13(b)]. If the number of receivers are equal in a monostatic network compared to a bistatic one, the standard deviation of the monostatic Doppler velocity measurement is indeed lower than the one achieved by the bistatic system by $1 - 2 \text{ m s}^{-1}$ [cf. Figs. 2.13(a) and 2.13(b)]. Nevertheless, the main advantage of the bistatic system lies in the low costs involved and the simultaneous measurement of each velocity component.

In accordance with the optimal configuration of bistatic receivers, the bistatic multiple–Doppler radar network consisting of three bistatic receivers was installed around OP. Conventional bistatic antennas were constructed for measurements within the boundary layer having a vertical aperture of 8° . For measurements during thunderstorms, two prototype antennas with vertical apertures of 22° were developed in the context of this thesis. These two antennas were installed in addition to the conventional antennas at Lagerlechfeld and Lichtenau, respectively, sharing one bistatic

receiver. An antenna-switch was constructed so that each antenna can be selected according to the azimuth angle of the transmitted radar beam. Since the power, measured by a bistatic receiver has to be corrected by the antenna power pattern in order to determine the reflectivity factor, the antenna power pattern of several bistatic antennas were measured at an antenna range at the DLR in OP.

High-quality and rapidly updated wind-vector fields are required for most applications, especially for regional weather surveillance, for the nowcasting of weather events, or warnings of severe weather at airports or around populated areas, and for assimilating wind-vector fields into numerical prediction models. A quality-control scheme was developed to quantify the confidence of the Doppler velocity measurements. For the first time, not only was the geometrically induced accuracy of the wind-field determination using a bistatic Doppler radar system considered, but also signal quality and the effects of external (e.g. birds) or internal (e.g. side-lobe, receiver synchronization) contamination were taken into account in analyzing the quality of the measurements. Furthermore, the wind-field structures at each level were tracked both in time and space.

In this quality-control scheme, the algorithms either reject noisy data (i.e. SQI algorithm and persistence check) or the quality of the measurements is analyzed by means of quality-index fields with values ranging from zero to one. These fields can be merged into an average quality-control field which is available together with the wind-vector field to the user.

To choose between a strict quality-control scheme which probably rejects too much data, and a scheme where some errors can slip through, is a difficult decision. It would be almost impossible if the requirements of the scheme were the same under different weather conditions. Therefore, the quality-control scheme needed to be developed in such a way, so that each algorithm could be flexibly and separately applied according to the weather situation or to the scientific/operational requirements.

The three components of the wind-vector field were derived using Doppler velocities together with a constraining model. The performance of the constraining model was examined. The impact of the integration technique and the influence of the irregular data density on the quality of the vertical-velocity retrieval was investigated also. As a result, different one-way and two-way-integration techniques were applied in order to validate the derived vertical velocities with simulated radar data. In general, minimization of up- and downward integration was favored because it used both ground-level and upper-level boundary conditions.

Furthermore, the impact of the data density on the quality of the wind-field retrieval was investigated. Using a bistatic antenna with a vertical aperture ranging from between 1° to 9° , the choice of the integration technique depends on whether the echo top of the weather phenomena was reached or not. It is suggested that the echo top be determined with an RHI measurement or a complete volume scan. If the sampling using a bistatic receiver terminates far below the echo top, an upward

integration should be favored. Otherwise, minimizing the results from the up- and downward integration should be used.

One of the aims of this thesis was to show that all three wind-components could be determined for different weather situations. This was achieved by performing wind synthesis and wind retrieval during a frontal passage with stratiform precipitation, during convective precipitation, and within a clear-air situation. Although the specific case studies could be validated only by ground-based observations, the estimated wind-field represented significant characteristics of the respective weather situations.

Horizontal wind-fields determined by the bistatic Doppler radar network at Oberpfaffenhofen were verified using measurements from an independent Doppler radar and in-situ flight measurements during stratiform precipitation. The differences for both applications were less than $\pm 2 \text{ ms}^{-1}$ and in many cases less than $\pm 1 \text{ ms}^{-1}$. These values are on the same order of magnitude as the accuracy of the wind-field measurements.

In conclusion, the bistatic Doppler radar system is an inexpensive alternative to an additional monostatic radar for the purpose of providing areas with horizontal wind-field measurements. It can be implemented also in existing monostatic radar systems. However at present, the usage of the bistatic Doppler radar system for the horizontal wind-field determination is not as well established as, e.g. the use of monostatic Doppler radar. Therefore, more investigations using the bistatic Doppler radar network in different weather situations must be conducted and more validations performed.

The impact of side-lobe contaminations is denoted to be critical by de Elia & Zawadzki (2000) for the bistatic network operated at McGill University, in Montreal, Canada. In this thesis, the investigation of side-lobe contamination during the case studies under discussion showed no impact on the measured data. Therefore, the possibility of side-lobe contamination induced by POLDIRAD should be investigated in future as precisely as by de Elia & Zawadzki (2000). According to the first results, the reduction in the secondary lobes of the transmitting power pattern plays the main impact on the possibility and degree of contamination. Within this context, power measured by the bistatic receivers would have to be adjusted to the reflectivity measured by POLDIRAD.

There are plans to install a vertically-pointing bistatic antenna to validate the estimation of w within the constraining model.

A quasi-operational test run assimilating horizontal wind-fields into the mesoscale model MM5 is expected to show if the quality-control algorithms are sufficient for operational applications. Further, it should also clarify how data should be presented for the operational assimilation into numerical weather prediction models.

As a next step, a bistatic Doppler radar network could be installed within the vicinity of airports, e.g. Frankfurt Main Airport, or as an additional component to the existing radar network operated by the DWD.

A Technical specifications

A.1 Transmitting radar, POLDIRAD

Frequency [GHz]	5.5027
Wavelength [cm]	5.45
Horiz./vert. beam-width [°]	1
Transmitted power [kW]	250
PRF [Hz]	Variable from 160 to 1200
Pulse width [μ s]	0.5, 1, 2
Range resolution [m]	any multiple of 75 75: unambiguous range 60 km 150: unambiguous range 120 km 300: unambiguous range 300 km
Minimum detectable signal [dBm]	-108, for 0.5 μ s pulse width
Dynamic range [dB]	linear 52 dB, logarithmic 80 dB
Number of samples	32, 64, or 128
Antenna diameter [m]	ca. 5
Antenna gain [dB]	44.5
sidelobe level [dB]	< -32 (for linear polarization)
Polarizations	Variable (linear, circular, elliptic) 128 amplitude and phase settings

A.1.1 Receiver at the radar

Longitude	11°16'45"
Latitude	48°05'12"
Height above MSL [m]	600
Number of range-bins	295
Gate separation [μ s]	Any multiple of 0.25
Maximum coverage [km]	Any multiple of 22.1
Processed parameters (available in real-time)	Reflectivity [dBZ] Doppler velocity [m s^{-1}]

A.2 Bistatic receivers at remote sites

Antenna gain [dB]	15.6, for $\Delta\Phi_b = 8^\circ$ 11, for $\Delta\Phi_b = 22^\circ$
Minimum detectable signal strength [W]	10^{-14}
Noise figure[dB]	2.8
Dynamic range [dBm]	58.6 (−118 to −59)
Number of range bins	126
Gate separation [m]	Any multiple of 37.5
Processed parameters (available in real-time)	Power [dBm] Doppler velocity [m s^{-1}] NCP

	Lichtenau	Lagerlechfeld	Ried
Longitude	11°04'52"	10°50'59"	11°2'27"
Latitude	47°52'50"	48°11'04"	48°17'21"
Baseline distance [km]	27.1	33.97	28.74
Height above MSL [m]	607	550	535
Orientation from POLDIRAD [°]	212	290	318
Delay time [μs]	87.5	109.1	90.8
Number of antennas	2	2	1
Horizontal antenna aperture[°]	60	60	60
Vertical antenna aperture [°]	8, 22	8, 22	8
Orientation of antenna [°] (based on the receive beam axis)	0, 90	142, 142	170

B Signal Processing

This section describes the acquisition of Doppler time series data, and the processing of such data to obtain a velocity power-spectrum and related Doppler parameters (moments), such as mean velocity and normalized coherent power (inversely proportional to the spectral width).

The frequency measurement of each single pulse is technically very expensive (Steinhagen & Lehmann, 1998) because typical wind velocities create small values in the Doppler shift. Furthermore, in case of weather echos, single sample estimates have a too large statistical uncertainty to yield meaningful data interpretation. Thus, large number of echos samples must be processed to provide the required accuracy which depends on both system characteristics and meteorological conditions (Zrnic, 1979).

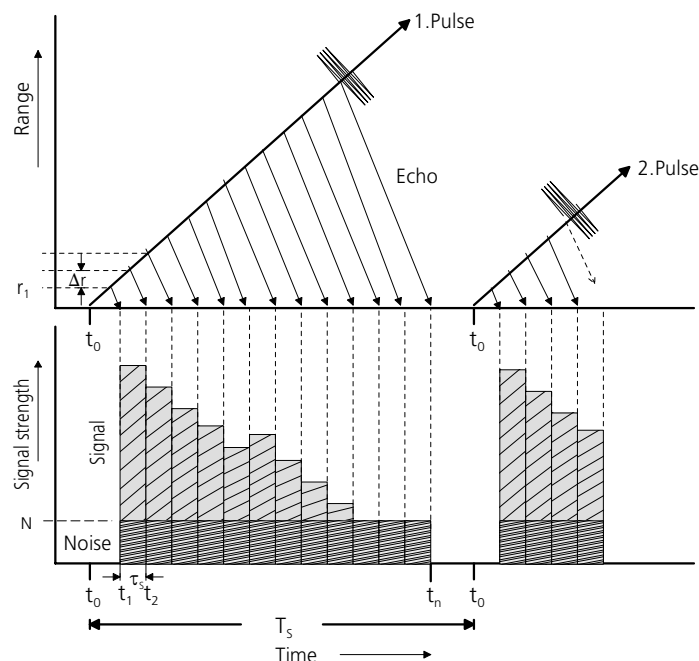


Figure B.1: Schematical view of the transmission and reception cycle of a radar system [modified from Czechowsky (1994)].

A transmission and reception cycle of a radar system for one ray (antenna does not tranverse) is schematically illustrated in Fig. B.1. At the time t_0 , the first pulse is transmitted and propagates in space. The receiver starts sampling at t_1 and proceeds sampling after each time interval τ_s (sample spacing).

Each receiver can only sample a certain number of echos which is limited by the number of range gates. The limit is set, because the power received from a meteorological target decreases with distance and the distatnce between radar beam and ground level increases with increasing distance.

The next pulse is send out after a time T_s (pulse repetition time). A radar

transmits many pulses each second. The maximum range a radar signal can travel and return before the next pulse is send out is given by

$$r_{\max} = \frac{cT_s}{2} \quad , \quad (\text{B.1})$$

where c is the speed of light. A time series is created from each received pulse corresponding to a certain range gate.

At the receiver the in-phase and quadrature position of the Doppler video signal is sampled (more details by Gekat (1998)). The simultaneous samples of 'I' and 'Q' of the k -th pulse are combined in a single complex number as $A_k = I_k + jQ_k$, where j is the square root of -1 . From this time series, a velocity power spectrum is computed by an autocorrelation technique, which is usually either a Fast Fourier Transformation (FFT²⁶) or pulse pair estimation algorithms.

At the remote bistatic receiver, 126 gates of the in-phase and quadrature position of the Doppler video signal (I and Q) are sampled for the usual dwell²⁷ time of 64 transmitted pulses. Here, the velocity-power spectrum is obtained using a pulse pair estimation algorithm. Detailed explanations to pulse pair estimation algorithms and signal processing at the bistatic receiver can be found by Keeler & Passarelli (1990); Wurman et al. (1994). The same processing is applied to the data measured by the receiver at POLDIRAD, except that 295 gates are processed.

The time series consists of 64 successive pulse signals measured by the remote receiver for each range gate. After combining the samples to A_k , the data collection pauses and a pulse pair estimation algorithm calculates the real and imaginary components of the lag one and lag two autocorrelations of I and Q.

The received signal can be characterized by the first three Doppler spectral moments (Keeler & Passarelli, 1990). The inverse transform of the Doppler power spectrum is taken to obtain the circular autocorrelation function $R_n = R(nT_s)$, where $T_s = 1/PRF$ and n is the number of Doppler spectral moments.

The total receiver power (zeroth moment), corrected by the noise power, P_0 is

$$P_r = R_0 - P_0 \quad . \quad (\text{B.2})$$

The next two lags are $R_1 = |R_1|e^{j\phi_1}$ and $R_2 = |R_2|e^{j\phi_2}$. For a Doppler power spectrum that is symmetric about the mean velocity, the velocity is obtained directly from the argument of the autocorrelation at the first lag, i.e.

$$\hat{V} = \frac{\lambda}{4\pi T_s} \theta_1, \quad (\text{B.3})$$

with $\theta_1 = \arg R_1$ being the angle between the positive real axis and the above vector.

²⁶FFT algorithms are explained in detail by Passarelli & Siggia (1983); Keeler & Passarelli (1990); Meischner et al. (2001).

²⁷Time over which a signal estimate is made. Usually, the time required for the antenna to traverse one degree [cited from the glossary by Rinehart (1999)].

Assuming that the Doppler spectrum is Gaussian and the signal-to-noise ratio is large, the spectral variance is given by

$$\sigma^2 = 2 \ln \frac{R_0}{|R_1|} \quad (\text{B.4})$$

For scientific purposes, the spectrum width is more physically meaningful than the variance, since it scales linearly with the severity of wind shear and turbulence. The spectral width is normalized to the Nyquist interval by π to ± 1 . The spectrum width is then given by $W = v_{nt}\sigma/\pi$.

As a measure of the signal quality, the normalized coherent power, NCP, is calculated at the bistatic receivers as

$$NCP = \frac{|R_1|}{R_0} \quad (\text{B.5})$$

NCP is inverse to σ^2 and varies between zero for an uncorrelated signal to one for a noise-free zero-width signal. It is introduced by BINET Inc. and a measure of the uncertainty in the velocity estimates.

References

- Alberoni, P. P., V. Ducrocq, G. Gregoric, G. Haase, I. Holleman, M. Lindskog, B. Macpherson, M. Nuret, A. Rossa, 2002: Quality and assimilation of radar data for NWP - a review. *COST-717 working document, available at <http://www.smhi.se/cost717/>*.
- Alberoni, P. P., P. Mezzasalma, S. Costa, T. Paccagnella, P. Patruno, D. Cesari, 2000: Doppler radar wind data assimilation in mesoscale analysis. *Phys. Chem. Earth (B)*, **25**, 1263–1266.
- Albers, S. C., 1995: The LAPS wind analysis. *Wea. Forecasting*, **10**, 342–252.
- Atlas, D., R. C. Srivastava, R. S. Sekhon, 1973: Doppler radar characteristics of precipitation at vertical incidence. *Rev. Geophys. and Space Phys.*, **11**, 1–35.
- Awaka, J., T. Oguchi, 1982: Bistatic radar reflectivities of Pruppacher–and–Pitter form raindrops at 14.3 and 5.33 GHz. *J. Radio Res. Lab.*, **29**, 125–150.
- Battani, L. J., 1973: *Radar observation of the atmosphere*. The University of Chicago Press, 324 pp.
- Boegel, W., R. Baumann, 1991: Test and calibration of the DLR Falcon wind measuring system by maneuvers. *J. Atmos. Oceanic Technol.*, **8**, 5–18.
- Bohne, R. A., R. C. Srivastava, 1976: Random errors in wind and precipitation fall speed measurement by a triple Doppler radar system. In *Proc. 17th Radar Meteorology Conf., Seattle*. Amer. Meteor. Soc., 7–14.
- Browning, K. A., R. Wexler, 1968: The determination of kinematic properties of a wind field using Doppler radar. *J. Appl. Meteor.*, **7**, 105–113.
- Carbone, R. E., F. I. Harris, P. H. Hildebrand, R. A. Kropfli, L. J. Miller, W. Moninger, R. G. Strauch, R. J. Doviak, K. W. Johnson, S. P. Nelson, P. S. Ray, M. Gilet, 1980: The multiple Doppler radar workshop, November 1979. *Bull. Amer. Meteor. Soc.*, **61**, 1169–1203.
- Chong, M., J. Testud, 1983: Three-dimensional wind field analysis from dual-Doppler radar data. Part III: The boundary condition: An optimum determination based on a variational concept. *J. Climat. Appl. Meteor.*, **22**, 1227–1241.
- Chong, M., J. Testud, F. Roux, 1983: Three-dimensional wind field analysis from dual-Doppler radar data. Part II: Minimizing the error due to temporal variation. *J. Climat. Appl. Meteor.*, **22**, 1216–1226.
- Crane, R. K., 1974: Bistatic scatter from rain. *IEEE Trans. Antennas Propag.*, **AP-22**, 312–320.

- Czechowsky, P. Principles of wind profilers. In Lafaysse, C., editor, *COST 74 final report*, 21–43. European Commission, Luxembourg, 1994.
- de Elia, R. *Performance study of a bistatic radar network*. PhD thesis, Dep. of Atmospheric and Oceanic Sciences, McGill University, Montreal, 2000.
- de Elia, R., I. Zawadzki, 2000: Sidelobe contamination in bistatic radars. *J. Atmos. Oceanic Technol.*, **17**, 1313–1329.
- de Elia, R., I. Zawadzki, 2001: Optimal layout of a bistatic radar network. *J. Atmos. Oceanic Technol.*, **18**, 1184–1194.
- Dibbern, J., 1987: Dependence of radar parameters on polarization properties of rain for bistatic CW radar. *Radio Sci.*, **22**, 769–779.
- Doviak, J. R., D. S. Zrnic, 1984: *Doppler radar and weather observations*. Academic Press, Inc., 458 pp.
- Doviak, R. J., 1972: Comparison of bistatic and monostatic radar detection of clear air atmospheric targets. In *Proc. AIAA, 10th Aerospace Sciences Meeting*, San Diego, Calif., 1–8.
- Doviak, R. J., P. S. Ray, R. G. Strauch, L. J. Miller, 1976: Error estimation in wind fields derived from dual-Doppler radar measurement. *J. Appl. Meteor.*, **15**, 868–878.
- Doviak, R. J., C. M. Weil, 1972: Bistatic radar detection of the melting layer. *J. Appl. Meteor.*, **11**, 1012–1016.
- Easterbrook, C. C., 1975: Estimating horizontal wind fields by two-dimensional curve fitting of single Doppler radar measurements. In *16th Radar Meteorology Conf., Houston, TX*. AMS, 214–219.
- Friedrich, K., M. Hagen, P. Meischner, 2000: Vector wind field determination by bistatic multiple-Doppler radar. *Phys. Chem. Earth (B)*, **25**, 1205–1208.
- Fulton, R. A., J. P. Breidenbach, D.-J. Sea, D. A. Miller, T. O’Bannon, 1998: The WSR–88D rainfall algorithm. *Wea. Forecasting*, **13**, 377–395.
- Gal-Chen, T., 1982: Errors in fixed and moving frame of references: Applications for conventional and Doppler radar analysis. *J. Atmos. Sci.*, **39**, 2279–2300.
- Gao, J., M. Xue, A. Shapiro, K. K. Droegemeier, 1999: A variational method for the analysis of three-dimensional wind fields from two Doppler radars. *Mon. Wea. Rev.*, **127**, 2128–2142.
- Gauthreaux, S. A., C. G. Belser, 1998: Displays of bird movements on the WSR–88D: Patterns and quantification. *Wea. Forecasting*, **13**, 453–464.

- Gekat, F. Grundlagen und Funktionsweise von modernen Wetterradargeräten. In *Annalen der Meteorologie Nr. 38, Herbstschule Radarmeteorologie*, 25–45. Deutscher Wetterdienst, 1998.
- Georgis, J.-F., F. Roux, P. H. Hildebrand, 2001: Observation of precipitating systems over complex orography with meteorological Doppler radars : A feasibility study. *Meteor. Atmos. Phys.*, **72**, 185–202.
- Gerz, T., 2001: Wake vortex prediction and observation: Towards an operational system. In *3rd ONERA–DLR Aerospace symposium ODAS 2001, Paris*, S1–3:1–10.
- Glaser, J. I., 1986: Fifty years of bistatic and multistatic radar. In *IEEE Proceedings F, Special issue on bistatic and multistatic radar*, volume 133, 596–603.
- Grell, G. A., J. Dudhia, D. R. Stauffer. A description of the fifth-generation PennState/NCAR mesoscale model (MM5). Technical Report 398, 117 pp, NCAR/Technical Note, 1994.
- Hagen, M. *Ableitung von Windfeldern aus Dopplermessungen eines Radars und Anwendung auf eine Kaltfront mit schmalem Regenband*. PhD thesis, Fakultät für Physik der Ludwig–Maximilians–Universität München, 1989.
- Hagen, M., 1997: Identification of ground clutter by polarimetric radar. In *Preprints, 28th Conf. on Radar Meteorology, Austin, TX*. Amer. Meteor. Soc., 67–68.
- Hagen, M., S. Stockinger. Verfahren zum automatischen Entfalten von Dopp- lergeschwindigkeiten mit einem Wetterradar. Technical Report DLR–FB 91–08, Deutsches Zentrum für Luft– und Raumfahrt, 1991.
- Hanle, E., 1986: Survey of bistatic and multistatic radar. In *IEEE Proceedings F, Special issue on bistatic and multistatic radar*, volume 133, 587–595.
- Heymsfield, A. J., 1977: Precipitation development in stratiform ice clouds: A micro- physical and dynamic study. *J. Atmos. Sci.*, **34**, 367–381.
- Houze, R. A., 1993: *Cloud dynamics*. Academic Press Inc., 573 pp.
- James, C. N., S. R. Brodzik, H. Edmon, R. A. Houze, S. E. Yutter, 2000: Radar data processing and visualization over complex terrain. *Wea. Forecasting*, **15**, 327–338.
- James, C. N., R. A. Houze, 2001: A real–time four–dimensional Doppler dealiasing scheme. *J. Atmos. Oceanic Technol.*, **18**, 1674–1683.
- Joss, J., A. Waldvogel, 1970: Raindrop size distributions and Doppler velocities. In *Proc. 14th Radar Meteorology Conf., Tucson, Arizona*. AMS, 153–156.
- Keeler, R. J., R. E. Passarelli. Signal processing for atmospheric radars. In Atlas, D., editor, *Radar in meteorology*, 199–229. Amer. Meteor. Soc., 1990.

- Kerker, M., 1969: *The scattering of light and other electromagnetic radiation*. Academic Press Inc., 666 pp.
- Klemp, J. B., R. B. Wilhelmson, 1978: The simulation of three-dimensional convective storm dynamics. *J. Atmos. Sci.*, **35**, 1070–1096.
- Lafore, J.-P., J. Stein, N. Asencio, P. Bougeault, V. Ducrocq, J. Duron, C. Fischer, P. Hereil, P. Mascart, J.-P. Pinty, J.-L. Redelsperger, E. Richard, J. V.-G. de Arellano, 1998: The Meso-NH Atmospheric Simulation System. Part I: Adiabatic formulation and control simulations. *Ann. Geophys.*, **16**, 90–109.
- Laroche, S., I. Zawadzki, 1994: A variational analysis method for retrieval of three-dimensional wind field from single-Doppler radar data. *J. Atmos. Sci.*, **51**, 2664–2682.
- Laroche, S., I. Zawadzki, 1995: Retrievals of horizontal winds from single-Doppler clear-air data by methods of cross correlation and variational analysis. *J. Atmos. Oceanic Technol.*, **12**, 721–738.
- Lazarus, S., A. Shapiro, K. Droegemeier, 1999: Analysis of the Gal-Chen-Zhang single-Doppler velocity retrieval. *J. Atmos. Oceanic Technol.*, **16**, 5–18.
- Lee, R., G. D. Bruna, J. Joss, 1995: Intensity of ground clutter and of echoes of anomalous propagation and its elimination. In *Preprints, 27th Conf. on Radar Meteorology, Vail, Colorado*. Amer. Meteor. Soc., 651–652.
- Lhermitte, R. M., 1971: Probing of atmospheric motion by airborne pulse-Doppler radar techniques. *J. Appl. Meteor.*, **10**, 234–246.
- Lhermitte, R. M., D. Atlas, 1961: Precipitation motion by pulse Doppler. In *Proc. 9th Weather Radar Conf., Boston*. Amer. Meteor. Soc., 498–503.
- Lindskog, M., H. Järvinen, D. B. Michelson. Development of Doppler radar wind data assimilation for the HIRLAM 3D-Var. Technical report, HIRLAM, 52, 2002.
- Meischner, P., R. Baumann, H. Höller, T. Jank, 2001: Eddy dissipation rates in thunderstorms estimated by Doppler radar in relation to aircraft in situ measurements. *J. Atmos. Oceanic Technol.*, **18**, 1609–1627.
- Meischner, P., C. Collier, A. Illingworth, J. Joss, W. Randeu, 1997: Advanced weather radar systems in Europe: The COST 75 action. **78**, 1411–1430.
- Miller, L. J., R. G. Strauch, 1974: A dual Doppler radar method for the determination of wind velocities within precipitating weather systems. *Remote Sens. Environ.*, **3**, 219–235.
- Montmerle, T., A. Caya, I. Zawadzki, 2001: Simulation of a midlatitude convective storm initialized with bistatic Doppler radar data. *Mon. Wea. Rev.*, **129**, 1949–1967.

- Nissen, R., D. Hudak, S. Laroche, R. de Elia, I. Zawadzki, Y. Asuma, 2001: 3D wind field retrieval applied to snow events using Doppler radar. *J. Atmos. Oceanic Technol.*, **18**, 348–362.
- O'Brien, J. J., 1970: Alternative solutions to the classical vertical velocity problem. *J. Appl. Meteor.*, **9**, 197–203.
- Orr, B. W., R. A. Kropfli, 1999: A method for estimating particle fall velocities from vertically pointing Doppler radar. *J. Atmos. Oceanic Technol.*, **16**, 29–37.
- Passarelli, R. E., A. D. Siggia, 1983: The autocorrelation function and Doppler spectral moments: Geometric and asymptotic interpretations. *J. Appl. Meteor.*, **22**, 1776–1787.
- Persson, G. O. P., T. Andersson, 1987: A real-time system for automatic single-Doppler wind field analysis. In *Proc. Symp. Mesoscale Analysis & Forecasting, Vancouver, Canada*, volume SP-282, 61–66.
- Powell, D. J. M., 1977: Restart procedures for the conjugate-gradient method. *Math. Prog.*, **11**, 42–49.
- Probert-Jones, J. R., 1962: The radar equation in meteorology. *Q. J. R. Meteorol. Soc.*, **88**, 485–495.
- Protat, A., I. Zawadzki, 1999: A variational method for real-time retrieval of three-dimensional wind field from multiple-Doppler bistatic radar network data. *J. Atmos. Oceanic Technol.*, **16**, 432–449.
- Protat, A., I. Zawadzki, 2000: Optimization of dynamic retrievals from a multiple-Doppler radar network. *J. Atmos. Oceanic Technol.*, **17**, 753–760.
- Qiu, J.-C., Q. Xu, 1992: A simple adjoint method of wind analysis for single-Doppler data. *J. Atmos. Oceanic Technol.*, **9**, 588–598.
- Quante, M., P. R. A. Brown, R. Baumann, B. Guillemet, P. Hignett, 1996: Three aircraft intercomparison of dynamical and thermodynamical measurements during the 'Pre-EUCREX' campaign. *Beitr. Phys. Atmos.*, **69**, 129–146.
- Ray, P. S., K. L. Sangren, 1983: Multiple-Doppler radar network design. *J. Climat. Appl. Meteor.*, **22**, 1444–1454.
- Ray, S. P., K. K. Wagner, K. W. Johnson, J. J. Stephens, W. C. Bumgarner, E. A. Mueller, 1978: Triple-Doppler observations of a convective storm. *J. Appl. Meteor.*, **17**, 1201–1212.
- Ray, S. P., C. L. Ziegler, W. Bumgarner, R. J. Serafin, 1980: Single- and multiple-Doppler radar observations of tornadic storms. *Mon. Wea. Rev.*, **108**, 1607–1625.

- Rinehart, R. E., 1999: *Radar for meteorologists*. Rinehart Publications, 428 pp.
- Rinehart, R. E., J. D. Tuttle, 1981: A technique for determining antenna beam patterns using a ground target. In *Preprints, 20th Conf. on Radar Meteorology, Boston*. Amer. Meteor. Soc., 672–675.
- Rogers, R. R., 1964: An extension of the Z–R relation for Doppler radar. In *Preprints, 11th Conf. on Radar Meteorology, Boulder, Colo.* Amer. Meteor. Soc., 14–18.
- Rossa, A., 2000: Use of radar observation in hydrological and NWP models. *Phys. Chem. Earth (B)*, **25**(10–12), 1221–1224.
- Satoh, S., J. Wurman, 1999: Accuracy of composite wind fields derived from a bistatic multiple–Doppler radar network. In *Proc. 29th Radar Meteorology Conf., Montreal*. Amer. Meteor. Soc., 221–224.
- Schroth, A. C., M. S. Chandra, P. Meischner, 1988: A C–band coherent polarimetric radar for precipitation and cloud physics research. *J. Atmos. Oceanic Technol.*, **5**, 803–822.
- Sekhon, R. S., R. C. Srivastava, 1971: Doppler radar observations of drop-size distributions in a thunderstorm. *J. Atmos. Sci.*, **28**, 983–994.
- Seltmann, E. E. J., 2000: Clutter versus radar winds. *Phys. Chem. Earth (B)*, **25**, 1173–1178.
- Serafin, R. J., J. W. Wilson, 2000: Operational weather radar in the United States: Progress and opportunity. **81**, 501–518.
- Shapiro, A., J. J. Mewes, 1999: New formulations of dual–Doppler wind analysis. *J. Atmos. Oceanic Technol.*, **16**, 782–792.
- Shupyatsky, A. B., 1974: Echo depolarization as measured with bistatic radar. *J. Rech. Atmos.*, **8**, 201–204.
- Skolnik, M., 1990: *Radar Handbook*. McGraw–Hill, Inc., 1200 pp.
- Smythe, R. G., D. S. Zrnić, 1983: Correlation analysis of Doppler radar data and retrieval of the horizontal wind. *J. Climat. Appl. Meteor.*, **22**, 297–311.
- Stein, J., E. Richard, J.-P. Lafore, J.-P. Pinty, N. Asencio, S. Cosma, 2000: High-resolution non-hydrostatic simulations of flash-flood episodes with grid-nesting and ice-phase parameterization. *Meteor. Atmos. Phys.*, **72**, 203–222.
- Steinhagen, H., V. Lehmann. Windprofiler Radar–Messprinzip und Signalverarbeitung. In *Annalen der Meteorologie: Herbstschule Radarmeteorologie 1998*, 211–222. Deutscher Wetter dienst, 1998.

- Sun, J., D. W. Flicker, D. K. Lilly, 1991: Recovery of three-dimensional wind and temperature fields from simulated single-Doppler radar data. *J. Atmos. Sci.*, **48**, 876–890.
- Takaya, Y., M. Nakazato, 2002: Error estimation of the synthesized two-dimensional horizontal velocity in a bistatic Doppler radar system. *J. Atmos. Oceanic Technol.*, **19**, 74–79.
- Testud, J., M. Chong, 1983: Three-dimensional wind field analysis from dual-Doppler radar data. Part I: Filtering, interpolation and differentiating the raw data. *J. Climat. Appl. Meteor.*, **22**, 1204–1215.
- Tuttle, D. J., G. B. Foote, 1990: Determination of the boundary layer airflow from a single Doppler radar. *J. Atmos. Oceanic Technol.*, **7**, 218–232.
- van Zyl, J. J., F. T. Ulaby. Scattering matrix representation for simple targets. In Ulaby, F. T., C. Elachi, editors, *Radar polarimetry for geoscience applications*, 364. Norwood, MA, Artech House, 1990.
- Wahba, G., J. Wendelberger, 1980: Some new mathematical methods for variational objective analysis using splines and cross validation. *Mon. Wea. Rev.*, **108**, 36–57.
- Waldteufel, P., H. Corbin, 1979: On the analysis of single-Doppler radar data. *J. Appl. Meteor.*, **18**, 532–542.
- Wüest, M., I. Zawadzki, W. Schmid, 2001: Noise filtering in a variational wind field retrieval from Doppler radar. *Meteor. Z.*, **10**, 131–140.
- Wurman, J., 1994a: Directly measured vector winds from an inexpensive bistatic multiple-Doppler radar network. In *COST75-Weather radar Systems*. Commission of European Communities, 562–573.
- Wurman, J., 1994b: Vector winds from a single-transmitter bistatic dual-Doppler radar network. *Bull. Amer. Meteor. Soc.*, **75**(6), 983–994.
- Wurman, J., S. Heckman, D. Boccippio, 1993: A bistatic multiple-Doppler radar network. *J. Appl. Meteor.*, **32**, 1802–1814.
- Wurman, J., M. Randall, C. L. Frush, E. Loew, C. L. Holloway, 1994: Design of a bistatic dual-Doppler radar for retrieving vector winds using one transmitter and a remote low-gain passive receiver. In *Proc. of the IEE—Special issue on remote sensing instruments for environmental research*, volume 82, 1861–1872.
- Xu, Q., C. J. Qiu, J. X. Yu, 1994: Adjoint-method retrievals of low-altitude wind fields from single-Doppler wind data. *J. Atmos. Oceanic Technol.*, **11**, 579–585.
- Yamada, Y., M. Chong, 1999: VAD-based determination of the Nyquist interval number of Doppler velocity aliasing without wind information. *J. Meteor. Soc. Japan*, **77**, 447–457.

- Zawadzki, I., 1973: Statistical properties of precipitation patterns. *J. Appl. Meteor.*, **12**, 459–472.
- Ziegler, C. L. A dual Doppler variational objective analysis as applied to studies of convective storms. Master's thesis, University of Oklahoma, 1978.
- Zrnic, D. S., 1979: Estimation of spectral moments for weather echos. In *IEEE Transactions on geoscience electronics*, volume GE-17, 113–128.

Dank

Ich möchte mich ganz herzlich bei all den Personen bedanken, die mir bei der Anfertigung meiner Arbeit mit Rat und Tat zur Seite standen.

Mein besonders herzlicher Dank gilt Martin Hagen, ohne dessen Idee ein bistatisches Radar am DLR zu installieren ich nie die Gelegenheit bekommen hätte, darüber zu promovieren. Ich danke für seine fachliche Hilfe und sein Engagement bei der Installation, Wartung und Reparatur der bistatischen Empfänger.

Den Herren Hermann Scheffold, Hans Krafcyk, Fred Ritenberg und Thomas Jank danke ich für die technische Unterstützung beim Betrieb der beiden Radarsysteme, mit denen ich arbeitete.

Ich bedanke mich bei Edgar Clemens für das Vermessen der bistatischen Antennen.

Für die konstruktiven Vorschläge und Kommentare bedanke ich mich bei Prof. Ulrich Schumann und bei Prof. Roger K. Smith.

Dank schulde ich der Belegschaft des DLR Standortes in Weilheim sowie Klaus Hager und seinen Wetterbeobachtern von der Geophysikalischen Beratungsstelle Lechfeld für die freundliche und unkomplizierte Unterstützung bei der Installation sowie dem alltäglichen Betrieb der bistatischen Empfänger. Sie ersparten mir so manche Fahrt dorthin.

Außerdem möchte ich all meinen Kollegen danken besonders Christian Keil, Thomas Birner, Arnold Tafferner, Thorsten Fehr und Hartmut Höller für die wissenschaftliche Unterstützung und die sportliche Ablenkung.

Ein Dankeschön geht an Madhukar Chandra (Inst. für Hochfrequenztechnik und Radarsysteme) für die anregenden Diskussionen zur Polarimetrie. Für das aufmerksame Korrekturlesen meiner Arbeit, die Vorschläge und besonders für die Kommentare danke ich Peter Meischner.

Allen Kollegen des Instituts für Physik der Atmosphäre gilt mein Dank für die angenehme Arbeitsatmosphäre und die stete Hilfsbereitschaft.

Ich danke Jörg Seltmann (DWD, Hohenpeißenberg) für die Bereitstellung der DWD Radardaten, die ich freundlicherweise für die Evaluation der bistatischen Windfelder nutzen konnte.

Great thanks goes to the radar team at McGill University Montreal specially to Isztar Zawadzki and Alain Caya for introducing me to the retrieval program as well as to Ramon de Elia for fruitful discussions and incitations for my work. Furthermore, I would like to say thank you to BINET Coop. (Josh Wurman, Mitch Randall, Chris Burghard) for all the support during installation and operation.

I would like to thank my roommate Evelyne Richard for the fruitful incitations, discussions, and the great working atmosphere during her stay at the DLR. I thank her and Jean-Piere Pinty for providing me kindly the meso-NH simulation for the tests on the vertical integration.

Besonders bedanken möchte ich mich auch bei meinem Freund Martin Käser für seine Geduld, Unterstützung und Aufmunterungen. Auch meinen Eltern und meinem Bruder gilt mein großer Dank, deren Unterstützung und Vertrauen jederzeit eine große Hilfe waren. Last but not least great, thanks are due to Nerissa Röhrs, who helped me with the English language.

Curriculum vitae

Persönliche Daten

Name Katja Friedrich
geboren am 1. April 1974
in Leipzig
Anschrift Kapuzinerstr. 39a, 80469 München

Schulausbildung

in Leipzig
Mai 1992 Abitur am Gymnasium Thomasschule zu Leipzig

Studium

September 1993 bis September 1998
Studium der Meteorologie an der Universität Leipzig
Dezember 1998 Diplom in Meteorologie
Thema der Diplomarbeit:
*Numerische Untersuchungen zur Sensitivität des Bowen-
Verhältnisses.*

Promotion

März 1999 bis Mai 2002 an der
Ludwig-Maximilians-Universität München
August 2001, Spiros G. Geotis-Preis der American
Meteorological Society für die beste Nachwuchspräsentation
präsentiert auf der 30. Internationalen Konferenz für
Radarmeteorologie
Thema des Posters:
*Wind Vector Field Determination with a Bistatic Multiple-
Doppler Radar Network.*

